Atomic Bose-Hubbard Systems With Single-Particle Control

Citation

Preiss, Philipp Moritz. 2016. Atomic Bose-Hubbard Systems With Single-Particle Control. Doctoral dissertation, Harvard University, Graduate School of Arts & Sciences.

Permanent link

http://nrs.harvard.edu/urn-3:HUL.InstRepos:26718727

Terms of Use

Share Your Story

Atomic Bose-Hubbard Systems with Single-Particle Control

A dissertation presented

by

Philipp Moritz Preiss

to

The Department of Physics

in partial fulfillment of the requirements

for the degree of

Doctor of Philosophy

in the subject of

Physics

Harvard University

Cambridge, Massachusetts

November 2015

Dissertation advisor   Author

Professor Markus Greiner   **Philipp Moritz Preiss**

Atomic Bose-Hubbard Systems with Single-Particle Control

Abstract

Experiments with ultracold atoms in optical lattices provide outstanding opportunities to realize exotic quantum states due to a high degree of tunability and control. In this thesis, I present experiments that extend this control from global parameters to the level of individual particles.

Using a quantum gas microscope for ^{87}Rb, we have developed a single-site addressing scheme based on digital amplitude holograms. The system self-corrects for aberrations in the imaging setup and creates arbitrary beam profiles. We are thus able to shape optical potentials on the scale of single lattice sites and control the dynamics of individual atoms.

We study the role of quantum statistics and interactions in the Bose-Hubbard model on the fundamental level of two particles. Bosonic quantum statistics are apparent in the Hong-Ou-Mandel interference of massive particles, which we observe in tailored double-well potentials. These underlying statistics, in combination with tunable repulsive interactions, dominate the dynamics in single- and two-particle quantum walks. We observe highly coherent position-space Bloch oscillations, bosonic bunching in Hanbury Brown-Twiss interference and the fermionization of strongly interacting bosons.

Many-body states of indistinguishable quantum particles are characterized by large-scale spatial entanglement, which is difficult to detect in itinerant systems. Here, we ex-

tend the concept of Hong-Ou-Mandel interference from individual particles to many-body states to directly quantify entanglement entropy. We perform collective measurements on two copies of a quantum state and detect entanglement entropy through many-body interference. We measure the second order Rényi entropy in small Bose-Hubbard systems and detect the buildup of spatial entanglement across the superfluid-insulator transition.

Our experiments open new opportunities for the single-particle-resolved preparation and characterization of many-body quantum states.

Contents

Acknowledgments

I would like to thank my advisor, Markus Greiner, for five wonderful years in his group. Markus is extremely supportive of every group member and very open to new ideas. He is an incredibly gifted experimentalist with an amazing ability to explain most of our experiments in terms of beamsplitters and speckle patterns.

It has been a pleasure to work with a number of great colleagues on the Rubidium experiment throughout the years. After I arrived in 2010, I learned a lot from Waseem Bakr before he left for MIT. Our postdoc Jon Simon was amazing at getting me up to speed on all aspects of the experiment. My fellow grad students at the time were Alex Ma and Eric Tai, whom I worked with throughout the next five years. I thank Alex for all the long sessions together in lab, especially during the bilayer days, and Eric, without whom the machine would certainly not run anymore. Philip Zupancic, a Master's student from Munich, deserves special credit for his work on the DMD and the control software. Rajibul Islam, our second postdoc, taught us to be persistent with the double-well system. By now, the Rubidium team has been rejuvenated by Alex Lukin, Matthew Rispoli and Robert Schittko, who will undoubtedly take good care of the experiment. Our new postdoc Adam Kaufman has already had a huge impact on the team.

Since the lab renovations in 2013 we no longer sit in the old tiny corner office, where monitors, chairs and elbows often touched. Fortunately, the group is still small enough to keep up-to-date with everyone and enjoy the company of the Lithium and Erbium teams in the new group office.

I would like to thank the people who make the physics department such a comfortable place to work at: Lisa Cacciabaudo, Sheila Ferguson, Carol Davis, Stuart McNeil, Jay McNeil, Stanley Cotreau, Jim MacArthur, and our group administrators.

Outside work, I thank everyone who has made the last years fun: Old friends who stayed in touch and came to visit, the new friends I made in Boston, and my family.

Lastly, I want to thank Julijana, who has been a continued source of warmth and support.

Dedicated to my parents Anette and Wolfgang,
and my sister Eva.

Chapter 1

Introduction

Across many physical platforms, there has been tremendous progress towards creating and controlling quantum mechanical systems in the laboratory. Trapped atomic ions [1] and superconducting qubits [2] enable high-fidelity control of few-particle systems, new techniques in waveguide manufacturing permit the study of correlated states in photonic systems [3], and advances in nano-fabrication enable experiments in highly engineered mesoscopic solid state systems [4].

A powerful experimental platform to realize strongly correlated states of delocalized particles are ultracold atoms in optical lattices [5]. Different atomic species, both fermionic and bosonic, are now routinely cooled close to their motional ground state and loaded into optical lattices with precisely controlled and almost arbitrary energy landscapes [6]. Feshbach resonances [7] are often accessible to tune the interaction between particles and a wide range of states with different underlying interactions, geometries, and quantum statistics can be realized. Using microscopy techniques, several groups have imaged bosonic [8, 9, 10] and fermionic [11, 12, 13] systems with single-particle resolution, gaining access

to local observables and correlation functions [14].

In this thesis, I present experiments that extend these local detection methods to the *local manipulation* of individual atoms. Using a quantum gas microscope [8, 9] for bosonic ^{87}Rb, we have developed a holographic beam shaping system to project arbitrary optical potentials on top of a square optical lattice. With these tailored potentials, we control dynamics and deterministically address individual particles in the optical lattice [15, 16].

The development of single-particle control for neutral atoms enables new types of experiments. We deterministically prepare one or two particles in localized Fock states and let the atoms propagate in an optical lattice, realizing continuous, one-dimensional quantum walks [17]. In contrast to previous implementations of quantum walks, we can tune the interactions between particles and access dynamics that are dominated by strong interactions. Such idealized scenarios can reveal phenomena that are difficult to isolate in bulk systems. In the two-particle densities and correlations, we directly observe the interplay between quantum statistics and interactions. A direct signature of bosonic quantum statistics in the Hong-Ou-Mandel interference of massive bosons [18], which we observe on an atomic beamsplitter realized by double-well potentials.

While such experiments on few-body systems reveal the microscopic phenomena underlying the Bose-Hubbard model, the full complexity of many-body quantum mechanics emerges when many indistinguishable particles become entangled [19]. The robust generation and control of entangled states is one of the central goals of applied quantum science. For quantum information processing and quantum cryptography, entanglement is the main resource that enables operations which are not possible classically [20]. Similarly, many quantum metrology schemes exploit non-classical states for enhanced sensitivity [21]. In

condensed matter physics, the most interesting new materials and systems are characterized by large-scale entanglement between constituent particles [22]. Unconventional superconductors, spin liquids, and fractional quantum Hall states are prominent examples.

What has been unclear is how the large-scale entanglement inherent to many-body states can be quantified in experiments [23]. In few-particle systems, the verification of entanglement can be achieved by witness operators [24] or state tomography [25]. For many-particle systems of interacting, delocalized particles, such as atoms in an optical lattice, a path for the experimental measurement and quantification of entanglement is less clear. The issue is not simply an experimental puzzle for atomic physicists: Even though entanglement plays a crucial role in quantum phase transitions [26], conformal field theories [27], and high energy theory [28], there is currently no general scheme for quantifying entanglement in physical systems.

We leverage the precise control over dynamics in our system to realize quantitative measurements of entanglement in itinerant systems. Our method uses collective observables in several realizations of the same quantum state. Interfering two copies of a many-body state in a double-well potential, we directly detect its quantum state purity and quantify entanglement entropy in one dimensional Bose-Hubbard systems [29, 30].

Collective measurements based on many-body interference characterize itinerant many-body phases by the entanglement entropy, which currently cannot be accessed in any other system. Our method is general and applies to multi-component gases, topological states [31, 32] and fermionic systems [33]. It provides a verification of quantum state purity, and can help to distinguish quantum fluctuations from classical noise.

Our microscopic observation of the dynamics of strongly interacting particles and the
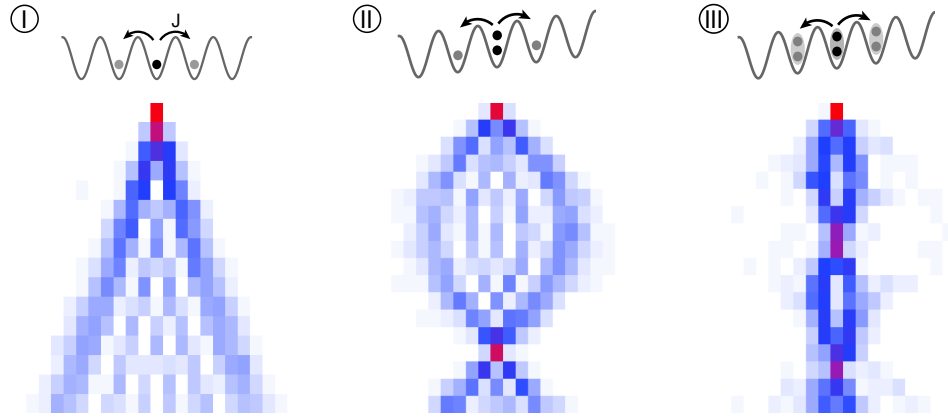
Figure 1.1: Density evolution in single- and two-particle quantum walks. From left to right: single particle quantum walk (I), two-particle Bloch oscillation in position space without (II) and with repulsive interactions (III).

detection of entanglement entropy highlight the capabilities of ultracold atom experiments. Beyond the *quantum simulation* paradigm of solving outstanding condensed matter problems [34, 5], cold atoms now realize *synthetic quantum matter* with interesting properties and possibilities in its own right. Recent examples of cold atoms pushing the envelope of condensed matter research are the implementation of strong synthetic gauge fields [35, 36], the creation of systems with tunable topology [37], and advances in the physics of disordered interacting systems [38]. The methods presented in this thesis add new possibilities of engineering quantum states and directly characterizing their nature through measurements of entanglement.

Quantum walks

In these conceptually simple experiments, particles are prepared in a highly localized initial state, and then allowed to propagate freely or under the influence of a uniform external force [39, 40]. Coherent quantum walks display behavior that is markedly differ-

$$|1,1\rangle \qquad |0,2\rangle + |2,0\rangle \qquad |1,1\rangle$$
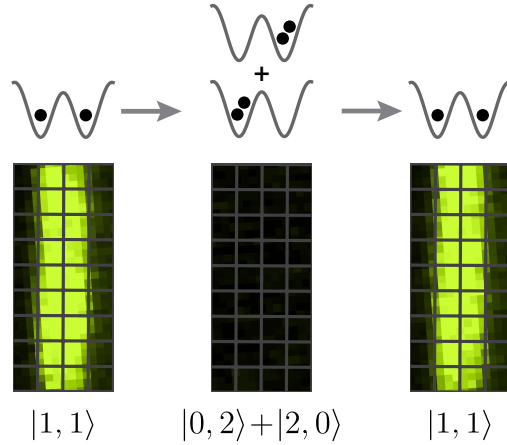
Figure 1.2: Hong-Ou-Mandel interference of massive bosonic particles. A beamsplitter operation realized in a double-well potential transforms a state with one particle per site (left) to a superposition state (middle) and back (right). Due to bosonic quantum statistics, the particles are always detected on the same site in the intermediate state. This state appears completely dark in fluorescence imaging because of the inherent parity projection.

ent from their classical random walk counterparts, with fast, ballistic instead of diffusive behavior. They have therefore been considered as the basic units of computation in time-independent quantum computing schemes [41]. We use the tunable interactions between ultracold atoms and our near-deterministic preparation scheme to realize two-particle quantum walks. We find that the densities and correlations emerging from two-particle quantum walks are an ideal probe of strong interactions. Two bosons performing a quantum walk in the presence of strong repulsive interactions develop fermion-like behavior and avoid each other over long distances. We observe this process known as fermionization from many-body theory, as well as interaction-dominated, correlated Bloch oscillations directly in the fundamental until cell of two particles.
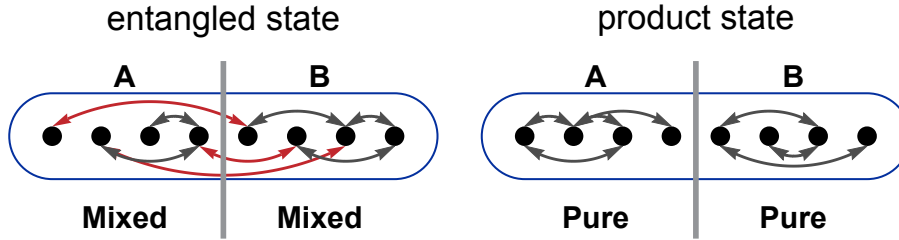
Figure 1.3: Entanglement entropy in many-body systems. If an entangled system is divided into subsystems A and B, quantum correlations across the boundary are interrupted (red arrows). In contrast to a product state, for which each subsystem is in a pure state itself, entanglement results in a subsystem mixed state with classical randomness. Detecting this reduction in local purity provides a path to measuring entanglement entropy.

Hong-Ou-Mandel interference

A second hallmark of many-body quantum systems are the quantum statistics of the constituent particles. Unlike for classical particles, many-particle paths of indistinguishable quantum particles can interfere and lead to correlations. These many-particle interference processes uniquely depend on quantum statistics and are different from single-particle interference, which can be described by classical waves. Photonic Hong-Ou-Mandel interference is the most famous signature of many-particle path interference. In direct analogy to the original Hong-Ou-Mandel experiment [18], we perform interference experiments of massive bosonic particles in the optical lattice. We observe full interference contrast, confirming the quantum mechanical indistinguishability of the two atoms [42, 43].

Entanglement entropy

Entanglement entropy can be detected by a direct extension of our Hong-Ou-Mandel interference experiments from single particles to many-body states. We prepare two copies of the same one-dimensional Bose-Hubbard state, and interfere them on a beamsplitter

realized by a double-well potential. The Hong-Ou-Mandel interference contrast is a direct measurement of indistinguishability and probes the quantum state purity [44, 29, 30]. We discover that for superfluid ground states, the HOM interference contrast for parts of the system is reduced, while it remains close to full amplitude for the entire system. The subsystems are hence less pure than the global system, and we encounter the classically impossible situation that part of a system carries more entropy than the full system itself [45]. The emergence of this non-extensive entropy can be measured directly in our experiments as a quantum system crosses from the Mott insulator to the superfluid regime.

This thesis is structured as follows:

Part I: A quantum gas microscope with single-particle control

I give a compact overview of the experimental apparatus. Chapter 2 gives a brief introduction to the Bose-Hubbard model, which describes the physics of neutral atoms in optical lattices. Chapter 3 introduces the ^{87}Rb quantum gas microscope on which the experiments in this thesis are performed, and chapter 4 describes our novel single-site addressing scheme.

Part II: Interactions and quantum statistics in few-particle dynamics

Here we investigate the building blocks of the Bose-Hubbard model, and study the role of interactions and quantum statistics in idealized scenarios of two-particle dynamics. Chapter 5 describes correlated quantum walks and position-space Bloch oscillations for strongly interacting bosons. Chapter 6 introduces the experimental tools for many-particle

interference in optical lattice and reports on our observation of Hong-Ou-Mandel interference of massive particles.

Part III: Measuring entanglement entropy

Chapter 7 gives an overview of the role of entanglement in different systems and its quantification via entanglement entropy. In chapter 8 we extend the concept of Hong-Ou-Mandel interference from individual particles to many-body states and describe our measurements of Rényi entanglement entropy and mutual information in Bose-Hubbard systems.

Part I

A quantum gas microscope with single-particle control

Chapter 2

Optical lattices and the Bose-Hubbard model

2.1 Optical lattices

Optical lattices have become a ubiquitous tool in ultracold atom experiments [5]. By defining the geometry of the system and controlling the atoms' motional degrees of freedom such lattices provide tremendous tuning capabilities in many-body systems. Many configurations, such as square [46], hexagonal [47], kagome [48], and tunable dimerized geometries [49] can be implemented.

In their simplest form, optical lattices in one dimension are generated by interfering counter-propagating laser beams with collinear polarization and frequency ω, resulting in a standing-wave intensity pattern with period $\lambda/2$. For appropriately chosen optical frequencies ω, an atom experiences the time-averaged intensity pattern $I(\mathbf{r})$ as a conservative
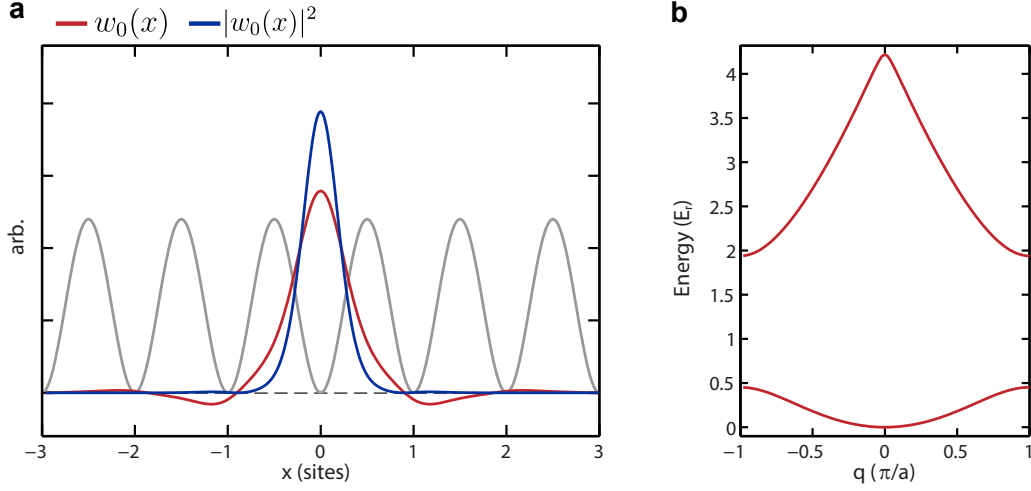
Figure 2.1: Single-particle wavefunctions in a periodic potential. a) Sketch of the lattice potential in gray and the ground band Wannier function $w_0(x)$ as well as the corresponding density $|w_0(x)|^2$, calculated for a lattice depth of $3\,E_r$. In this shallow lattice, the Wannier function still has significant side lobes on the neighboring sites. b) Band structure $E^{(m)}(q)$ at $V_{2D} = 3\,E_r$ for the lowest two bands. The ground band is approximately sinusoidal, i.e. close to the tight binding regime, whereas the second band still displays free-particle like dispersion.

potential

$$V(\mathbf{r}) = -\frac{1}{2\epsilon_0 c}\alpha(\omega)I(\mathbf{r}) \tag{2.1}$$

via the AC Stark shift. For red-detuned light, that is with a frequency smaller than the dominant atomic resonance, the frequency-dependent dynamic polarizability $\alpha(\omega)$ is positive, and regions of high intensity correspond to attractive potentials. Blue-detuned light creates repulsive potentials.

To determine the total potential experienced by a real atom in a light field, the polarizability $\alpha(\omega)$ needs to be summed over all relevant atomic transitions. For ^{87}Rb, the principal transitions are the $D1$ and $D2$ line at $\lambda_{D1} = 795\,\text{nm}$ and $\lambda_{D2} = 780\,\text{nm}$, respectively. Convenient choices for lattice lasers are red-detuned (attractive) lattices at $\sim 840\,\text{nm}$ or $1064\,\text{nm}$, or blue-detuned (repulsive) lattices at $755\,\text{nm}$, as used in our experiment.

11

We perform experiments in a two-dimensional square optical lattice, for which the lattice potential is separable and takes on the form

$$V(x) = V_{2D} \cos^2(k_l x) \tag{2.2}$$

along the x and y directions. The lattice momentum $k_l = \frac{\pi}{a}$ is set by the lattice spacing a. It is convenient to express energy in units of the recoil energy $E_r = \frac{\hbar^2 k_l^2}{2m}$. Throughout this thesis, we will use units in which $\hbar = 1$ and hence all energies are expressed as *angular* frequencies. In our case of ^{87}Rb in a lattice of spacing $a = 680$ nm the recoil energy is $E_r \approx 2\pi \times 1240$ Hz.

The single-particle eigenstates in a periodic lattice are Bloch waves, which are labeled by a band index m and are eigenstates of the quasimomentum q, with $-k_l \leq q \leq k_l$. The Bloch wavefunctions and their energy eigenvalues, the bandstructure $E^{(m)}(q)$, can be calculated numerically for each axis using plane wave basis states. The bandstructure as shown in Figure 2.1 b completely determines the physics of non-interacting particles in the optical lattice.

A second useful set of basis functions are Wannier functions (Figure 2.1 a). This set of basis states consists of maximally localized and mutually orthogonal wavefunctions on each lattice site. Localized Wannier functions can be constructed from coherent superpositions of all Bloch eigenstates within a particular band, and smoothly connect to the approximate on-site eigenstates of deep lattices. For detailed descriptions of the calculation of Bloch bands, Wannier functions, and bandstructures we refer to references [50] and [51].

$$H = -J \sum_{\langle i,j \rangle} a_i^\dagger a_j + \frac{U}{2} \sum_i n_i(n_i - 1)$$

kinetic energy
interaction energy
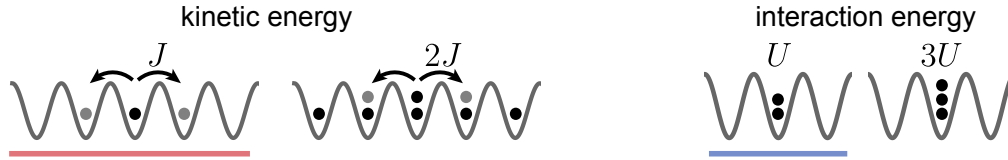
Figure 2.2: Processes in the Bose-Hubbard model. a) Atoms tunnel between neighboring sites at a rate J, set by the depth of the optical lattice. Due to Bose enhancement, tunneling in the presence of other atoms is enhanced, for example to $2J$ for an atom tunneling on a constant background of one atom per site. b) The energy cost of two particles occupying the same site is the repulsive interaction U. Multiple particles on the same site interact pair-wise. The interaction strength is assumed to be independent of the number of particles per site.

2.2   The Bose-Hubbard model

The physics of ultracold bosonic atoms in optical lattices is very well described in terms of the Bose-Hubbard model. In contrast to mean-field equations with interaction corrections, such as the Gross-Pitaevski equation, the bosonic Hubbard model captures correlated states that arise in the case of strong interactions between bosonic atoms.

The canonical Bose-Hubbard model is given by the Hamiltonian

$$H_{\mathrm{BH}} = -J \sum_{\langle i,j \rangle} a_i^\dagger a_j + \frac{U}{2} \sum_i n_i(n_i - 1). \tag{2.3}$$

Here, $a_i^\dagger$ and a_i are bosonic creation and annihilation operators on site i, $n_i = a_i^\dagger a_i$ measures the particle number, and the sum in the first term runs over adjacent lattice sites i, j. The basis functions of the Hubbard Hamiltonian are the localized Wannier states in the lowest

band.

The Hamiltonian 2.3 describes the two most basic low-energy processes occurring in an optical lattice, as illustrated in Figure 2.2. The first part of the Hamiltonian captures coherent hopping on neighboring lattice sites at a rate J. Due to bosonic statistics, the presence of other atoms in the lattice can enhance effective tunneling rates, as shown in Figure 2.2. The second term of the Hamiltonian describes the interaction of multiple atoms residing on the same lattice site, parameterized by the pairwise interaction U.

It is straightforward to obtain the Bose-Hubbard parameters J and U for a given lattice potential. The Bose-Hubbard Hamiltonian assumes the tight-binding regime, i.e. that tunneling occurs only between neighboring lattice sites. This assumption is valid for lattices deeper than $\sim 5\, E_r$ and the tunneling $J^{(m)}$ in band m is equal to 1/4 of the width of the mth band.

The magnitude of the interaction U can be calculated by considering the scattering between two atoms on the same lattice site in the ground band Wannier function. At the low temperatures realized by ultracold atoms, an efficient description of two-particle interactions is given by s-wave scattering. The interaction can be modeled as an effective δ-function potential, whose strength is given by a momentum-independent scattering length a_s. For ^{87}Rb, the scattering length at low magnetic fields is approximately independent of the hyperfine spin, and $a_s \approx 100 a_0$ results in repulsive interactions. The Bose-Hubbard interaction parameter U can then be estimated by integrating the single-particle Wannier functions with a δ-function interaction over all space. Detailed treatments of scattering theory and the derivation of the Bose-Hubbard parameters J and U can be found in many references, for example [50, 51].
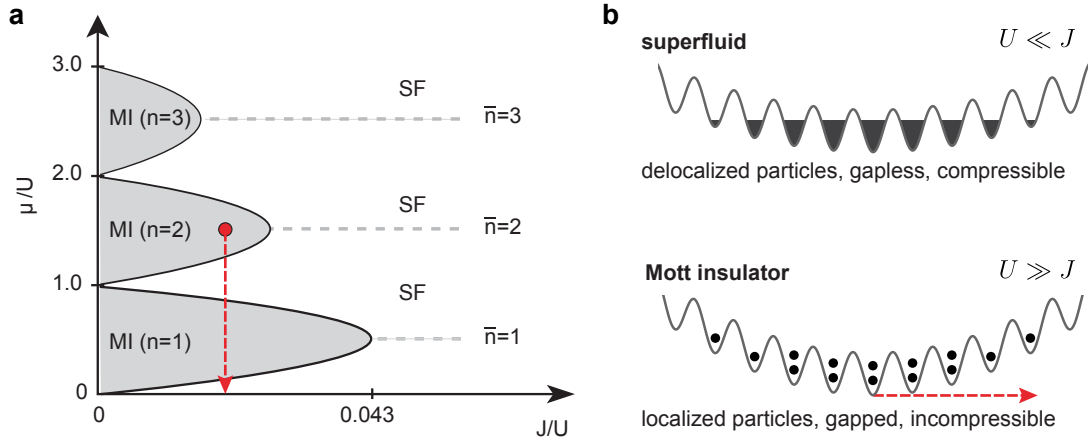
Figure 2.3: Superfluid-insulator phase transition. a) Schematic zero-temperature mean-field phase diagram for the Bose-Hubbard model in two dimensions. At large J/U, the ground state is a superfluid (SF) for all μ. For small J/U, Mott insulating (MI) lobes of fixed particle number separated by superfluid regions develop. b) Schematic drawings of the phases in harmonic traps, as realized in the experiment. The superfluid is compressible and the density varies smoothly with the chemical potential. The Mott insulator of localized particles exhibits domains of constant density, where the system is incompressible $\frac{\partial \langle n \rangle}{\partial \mu} = 0$. The local chemical potential varies throughout the trap, and the system samples a line through the phase diagram (red arrow).

The single-band Bose-Hubbard model applies as long as the relevant energy scales J, U, the chemical potential μ, and the temperature T are much smaller than the energy gap to higher bands. For experiments with multiple species or spin states, the Bose-Hubbard model is easily extended to a multi-component model, where differences between intra- and inter-species interactions can give rise to interesting physics [52, 53].

2.3 Quantum phase transition

It is clear that the nature of the many-body eigenstates of Hamiltonian 2.3 depends on the relative size of the kinetic energy J and the interaction energy U. One approach

to tuning their relative strength is through Feshbach resonances [7]: Applying a magnetic bias field can bring two atoms into resonance with a molecular bound state, and lead to a resonant enhancement in scattering. The scattering length a_s for some atomic species can thus be controlled by an external magnetic field, and be tuned to zero or negative values, corresponding to vanishing and attractive interactions, respectively.

In our experiment, we instead control the depth of the optical lattices to tune the Bose-Hubbard parameters: The tunneling J decreases approximately exponentially with increasing lattice depth, i.e. particles tunnel at reduced rates and acquire an enhanced effective mass. Even in moderately deep lattices, the relative strength of interaction terms is therefore increased dramatically compared to free space, and bosonic systems enter the strongly interacting regime at extremely low absolute densities of order one particle per site, or $10^{12} - 10^{13}$ per cm^3.

The competition between minimizing kinetic and interaction energy manifests itself as the well-known superfluid-Mott insulator phase transition in the ground state of the Bose-Hubbard model. In contrast to classical phase transitions, which are driven by thermal fluctuations, this phase transition is driven by quantum fluctuations, here the tunneling terms, and occurs even at zero temperature.

Superfluid phase In the regime $U \ll J$, atoms tend to accumulate in a single macroscopic wavefunction. In the ground state for vanishing interactions, all particles occupy the same $q = 0$ quasimomentum eigenstate and coherently delocalize over the entire system. The many-particle wavefunction of the superfluid can be written as

$$|\Psi_{\text{SF}}\rangle = \frac{1}{\sqrt{N}}(a_{q=0}^\dagger)^N |0\rangle \propto \left(\frac{1}{\sqrt{N}} \sum_i a_i^\dagger \right)^N |0\rangle . \tag{2.4}$$

For conceptual purposes, the superfluid wavefunction can be approximated as

$$|\Psi_{SF}\rangle \approx \prod_i |\alpha\rangle_i = \prod_i e^{-\frac{|\alpha|^2}{2}} e^{\alpha a_i^\dagger} |0\rangle \,, \tag{2.5}$$

i.e. the wavefunction on each site i can be described as a coherent state $|\alpha\rangle_i$ with well-defined phase $\phi = \arg(\alpha)$ and density $\langle n \rangle = |\alpha|^2$.

In three dimensions, the ground state possesses long-range phase coherence, i.e the condensate has the same well-defined phase everywhere and the first-order correlator $\langle a_j^\dagger a_k \rangle$ remains finite as $|j - k| \to \infty$.

Excitations in a weakly interacting condensate can be described by Bogoliubov excitations. Such excitations are gapless and have a linear dispersion relation $E \approx v_c q$ for small momenta q, where v_c is the critical velocity of the superfluid.

Mott insulator phase The Mott insulating regime is entered when interactions dominate the Hamiltonian ($U \gg J$). For $J = 0$, all particles localize and the ground state corresponds to the energetically most favorable way of stacking classical repulsive particles. For densities commensurate with the lattice, Mott insulators with a fixed number of atoms per site form, i.e. the ground state for $n = 1$ particles per site is

$$|\Psi_{\mathrm{MI}}\rangle = \prod_i a_i^\dagger |0\rangle \,, \tag{2.6}$$

where i runs over all sites. The Mott insulator does not exhibit any spatial phase coherence. The lowest-lying excitations at an energy U are particle-hole pairs, and the excitation spectrum is gapped with discrete resonances corresponding to local excitations.

The Mott insulator and superfluid phase in the Bose-Hubbard model are connected via a quantum phase transition [46, 54]. Qualitatively, the transition can be understood as the

proliferation of coherent particle-hole pairs: Starting from the $J = 0$ ground state $|\Psi_{\mathrm{MI}}\rangle$, perturbatively increasing J results in the coherent admixture of particle-hole pairs to the many-body wavefunction. As J is increased further, the formation of particle-hole pairs becomes more favorable, until all particles delocalize.

The observation of the Mott-superfluid phase transition with bosons in optical lattices [46] was a ground-breaking demonstration of many-body quantum mechanics with cold atoms. By now, the equilibrium and dynamic phase transition have been studied thoroughly through phase coherence [46], local number statistics [55, 9], and excitation spectra [56].

The behavior of Bose-Hubbard systems strongly depends on dimensionality: As expected, the behavior in higher dimensions is more closely described by mean field theory than in lower dimensions, where quantum fluctuations are enhanced [14]. Experimentally, optical lattice systems can be realized with three-, two,- or one-dimensional geometries by freezing out motion in unwanted directions in deep lattices.

2.4   Related models

Depending on the particular parameter regime, physics inherent to the Bose-Hubbard model can be more easily explained by mapping to different, well-understood descriptions.

Continuum models   For sparsely filled one-dimensional systems, the Bose-Hubbard model can be mapped to the Lieb-Lininger model, which describes bosonic continuum systems with contact interactions [57]. Just like the Lieb-Lininger model, the Bose-Hubbard model exhibits "fermionization" in the regime of infinite repulsive interactions [58], where the bosonic system displays fermion-like behavior in certain observables. The close relation to

continuum models has enabled the observation of a lattice analog of the Tonks-Girardeau gas [59]. However, in contrast to the Lieb-Lininger model, which exhibits a large number of conserved quantities at any interaction strength [60], the Bose-Hubbard model is integrable only in the limits of $U = 0$ or $U \to \infty$.

Spin models   Several models of quantum magnetism can be accessed from the Bose-Hubbard model. The Heisenberg model has been implemented in a two-component Bose gas in the Mott insulating regime, where density fluctuations are suppressed and spin remains as the only degree of freedom [61]. Atoms between neighboring sites are coupled through virtual tunneling processes at the superexchange energy scale $J_{\text{ex}} = \frac{4J^2}{U}$, resulting in an effective XXZ model. In our group, the antiferromagnetic Ising model in a transverse field has been simulated using Mott insulators in tilted optical lattices [62]. Here, spin is encoded in motional states rather than in hyperfine internal states.

Luttinger liquids   The low-energy properties of one-dimensional Bose-Hubbard systems can often be described by Luttinger liquid theory [63]. Here, conjugate variables $\nabla\phi(x)$ and $\theta(x)$ describe density and phase fluctuations of a bosonic field, respectively. The appeal of Luttinger liquid theory is its broad applicability to fermionic and bosonic systems, and the complete specification of the system in terms of only two parameters, the sound velocity u and the interaction parameter K. Luttinger liquid theory can be used, for example, to calculate the scaling of number fluctuations as a proxy for entanglement entropy in weakly interacting Bose-Hubbard systems as discussed in chapter 8.
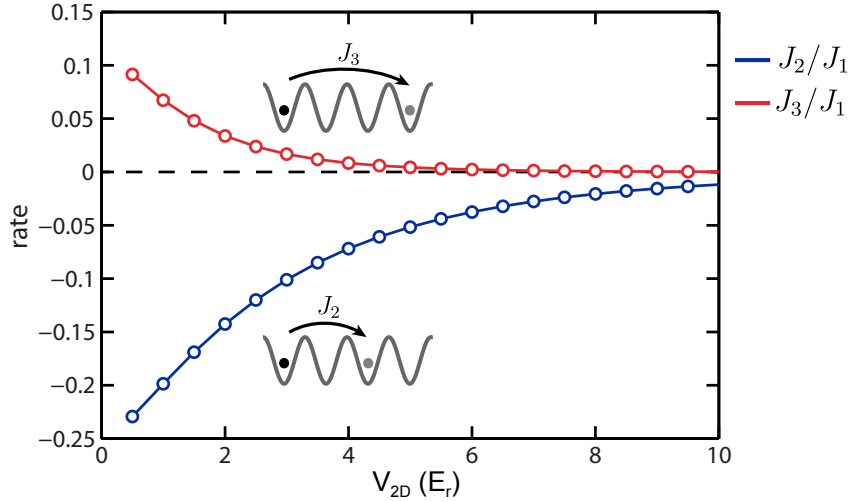
Figure 2.4: Breakdown of the tight-binding assumption at low lattice depths. For lattice depths $V_{2D} < 5\,E_r$, tunneling terms not typically included in the Bose-Hubbard model become significant. The figure shows the rate of direct tunneling across two and three sites (J_2 and J_3), relative to nearest-neighbor tunneling J_1. The rates were calculated numerically as the coefficients of a Fourier expansion of the lowest band dispersion relation for the data points shown. The line connects the data points.

2.5   Beyond Bose-Hubbard models

The Bose-Hubbard Hamiltonian 2.3 provides an efficient description of the physics of bosons in periodic potentials, but does not include all processes which naturally occur for cold atoms in optical lattices. In shallow lattices $V_{2D} < 5\,E_r$, the tight-binding approximation begins to break down and direct long-range tunneling occurs. Figure 2.4 shows the relative strength of tunneling across two sites (next-nearest-neighbor) and across three sites. Next-nearest neighbor tunneling can be significant, and affects the quantum walk dynamics described in chapter 5. Nearest-neighbor interactions or interaction-induced tunneling [64] can occur due to the finite extent of Wannier functions beyond a single lattice site. Such terms, as well as multiorbital shifts to the on-site interaction U [65], can be estimated

by summations over higher bands [66, 67], and are often incorporated by renormalizing Bose-Hubbard terms [68].

It is also possible to access novel physics by deliberately engineering the terms of the Bose-Hubbard model. For example, using Raman transitions or periodically modulated or shaken optical lattices, it is possible to locally imprint a complex phase on the tunneling matrix elements [69]. If this phase varies spatially such that closed loops encircle a non-zero phase, the Hamiltonian effectively corresponds to that of a charged particle in a magnetic field. Extremely high flux densities of the order of π per lattice plaquette can be engineered, enabling the realization of topologically non-trivial models, such as the Hofstadter-Harper Hamiltonian [36, 70]. In combination with strong interactions, the availability of high flux densities puts ultracold atoms in a unique position to realize highly correlated phases, such as fractional quantum Hall states.

Chapter 3

Overview of the experimental apparatus

3.1 Quantum gas microscope

The experiments presented in this thesis are performed using a quantum gas micro-scope for bosonic atoms. We study a two-dimensional atomic cloud of ^{87}Rb confined to a single plane of a three-dimensional optical lattice. The ultracold gas resides at the focus of an imaging system with numerical aperture (NA) 0.8, which allows single-site resolved readout and optical manipulation. In situ fluorescence imaging is used to detect individual atoms in the optical lattice. Detailed descriptions of the apparatus have been given in a number of publications [71, 8, 72, 73, 74]. Here, we briefly summarize the main aspects of the experimental setup.

Figure 3.1 shows a schematic overview of the experiment. At the core of the appa-ratus is the high-NA imaging setup consisting of a custom-made objective with NA 0.55 outside and a fused silica hemispherical lens inside the vacuum chamber. The hemisphere enhances the NA of the imaging system by its refractive index $n = 1.45$ to an NA of 0.8. A
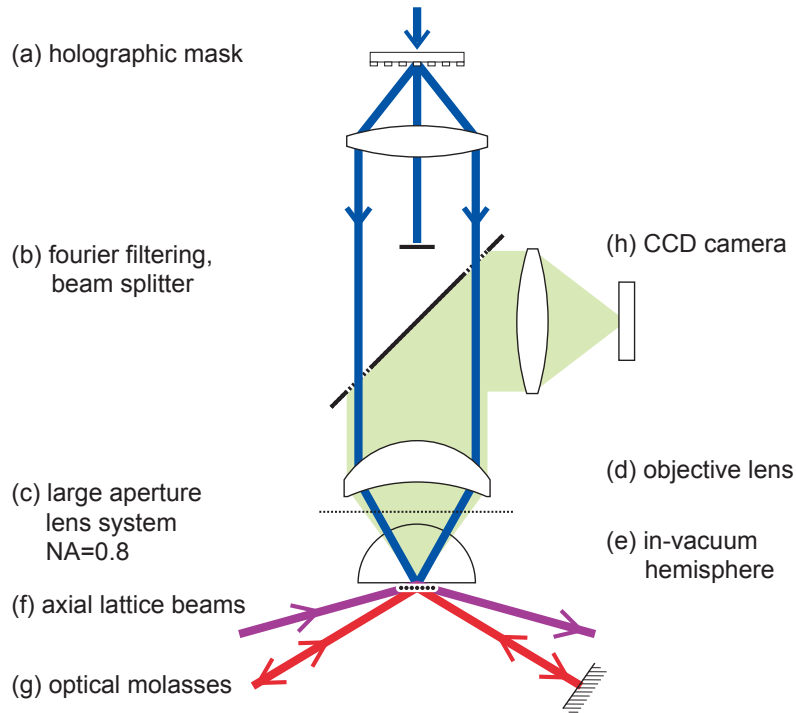
Figure 3.1: Schematic of the experimental setup. The two-dimensional atomic cloud of ^{87}Rb is trapped $10\,\mu$m below the surface of the in-vacuum hemisphere. The vertical confinement is provided by axial lattice beams (purple) reflected at the hemisphere under a shallow angle, as are the molasses beams for fluorescence imaging (red). The square lattice (blue) is generated by holographic masks and projected through the microscope objective, which is also used to image atoms (light green path). Figure adapted from [8].

Bose-Einstein condensate of ^{87}Rb created by conventional evaporation in a magnetic trap resides at the focus of the imaging system, $10\,\mu$m below the flat surface of the hemispherical lens. Optical lattice potentials to confine atoms in the vertical direction are created by beams entering from the side, while lattices within the x–y plane are projected through the objective. Atoms are imaged onto an EMCCD camera using fluorescence imaging with polarization gradient cooling provided by optical molasses beams. Various other beams, e.g. for harmonic confinement or single-atom addressing, are coupled into the imaging path using dichroic filters and propagate downwards through the objective.

3.2 Optical lattice potentials

The potential landscape experienced by the atoms is defined by optical means in all three dimensions. In the vertical direction (z), the atoms are confined to a single node of an optical lattice. This "axial lattice" is generated by reflecting a single beam off the uncoated flat surface of the hemispherical in-vacuum lens as shown in Figure 3.1. The beam is incident at $14°$ from horizontal, and interferes with its own reflection from the substrate to produce a standing wave of period $1.5\,\mu$m. The atoms are confined to the 6th minimum from the substrate, which provides a reference surface for all optical traps in the vertical direction. The z-position of the atoms is very stable, and the focus of the imaging system is consistent for months at a time.

In the x–y plane, atoms are confined to a square optical lattice with spacing $a = 680\,$nm, which is generated by imaging a holographic mask onto the atomic cloud through the objective [72].

The quantum mechanical evolution of the ultracold gas proceeds in blue-detuned lattices centered at a wavelength $\lambda = 755\,$nm. These lattices are far detuned from the atomic resonances at $\lambda_{D1} = 795\,$nm and $\lambda_{D2} = 780\,$nm and create a conservative potential. Using blue-detuned optical lattices reduces the sensitivity to potential corrugations in the lattice, since the atoms are localized to the nodes of the light field and their energy depends on the local lattice depth V only as $\propto V^{1/2}$ via their zero-point energy $\hbar\omega/2$. In this "physics" lattice, only moderate lattice depths of up to $V_{2\mathrm{D}} = 45\,E_r$ are required to control ground-band tunneling on time scales of the experiment (typically $1-2\,$s). We observe single-atom $1/e$ lifetimes of $12(2)$ s, limited by residual spontaneous scattering.

During the imaging process, atoms have to remain pinned while scattering thousands of

photons. In this "thermal" regime, atoms are distributed over several bands, and very deep lattices are required to localize the atoms. In order to avoid working with high-powered ($\gg 1$ Watt) lasers, we employ a set of near-detuned "pinning" lattices, whose geometry is identical to the physics lattice. The pinning lattices are 60 GHz blue-detuned from the $D1$ transition at $\lambda_{D1} = 795$ nm. Because the pinning lattices are only used in combination with the optical molasses, which counterbalance excitations caused by spontaneous scattering, heating from the near-detuned beams is not relevant. Potential depths of up to $5000\,E_r$ can be realized in the pinning lattice using about 350 mW per lattice axis derived from a Ti:Sapph (Coherent MBR 110) laser.

The geometry of individual lattice sites has to be preserved during the handover from the physics to the pinning lattice. Within the x–y plane, this requirement is guaranteed by the generation of the lattice via the holographic mask: The spacing and phasing of the lattices is fixed by the imaging condition and independent of the wavelength, so the handover from 755 nm to 795 nm light does not change the lattice structure. In the vertical z-direction, the angle of incidence of the pinning lattice onto the substrate is chosen to match the spacing of the axial physics lattice. We verify the correct phasing of the lattices using simultaneous Kapitza-Dirac scattering with the beams at 755 nm and 795 nm.

3.3   Single-atom imaging

Single-atom resolved imaging requires spatial resolution on the order of one lattice site and the collection of many photons from each individual atom. For our imaging system with NA 0.8, we measure an almost diffraction-limited point spread function (PSF) with a FWHM of $\sim$600 nm, slightly smaller than the lattice spacing $a = 680$ nm [8]. Identifying
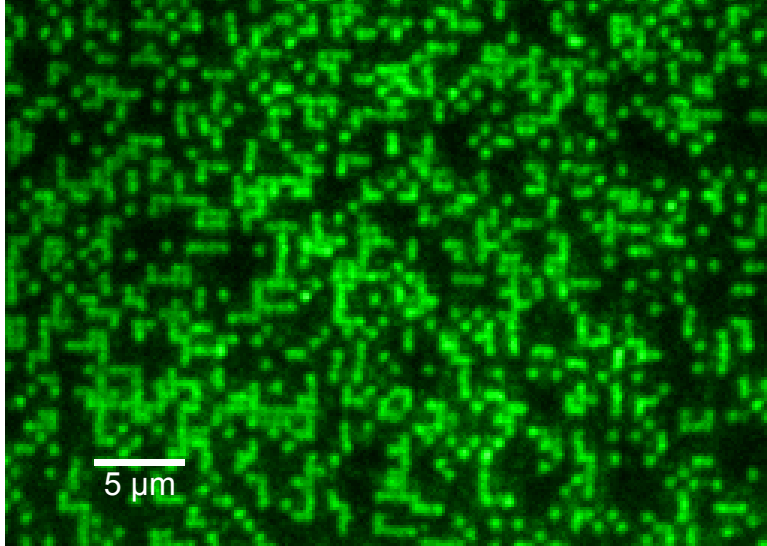
Figure 3.2: Partial raw image of a thermal cloud of ^{87}Rb. Individual atoms can be identified, and the underlying square lattice structure is visible. Due to parity projection in the imaging process, each site is either bright (odd atom number) or dark (even atom number). The full field of view is about $100\,\mu$m$\times100\,\mu$m, i.e. several ten thousand lattice sites can be imaged at the same time. Figure adapted from [8].

individual atoms at this spatial resolution requires the collection of several hundred photons from each atom, necessitating the use of in-lattice cooling mechanisms.

We achieve the required signal-to-noise ratio using polarization gradient cooling [75]: While freezing out motion in the deep ($\sim5000\,E_r$) lattice near $\lambda_{D1} = 795\,$nm, we cool the atoms using two retro-reflected optical molasses beams $80\,$MHz red-detuned from the $D2$ transition ($\lambda = 780\,$nm). Photons scattered from the molasses beams can be separated from the background due to the lattice using interference filters, and are collected on an EMCCD camera for imaging. We observe atom lifetimes in the imaging lattice of $\sim30\,$s, consistent with background gas collisions. Throughout this time, each atom scatters up to $20,000$ photons per second, of which $\sim10\,\%$ are detected on the camera. We expose the sensor for $500\,$ms, a compromise between atom lifetime and number of collected photons.

Inherent to our fluorescence imaging scheme are light-assisted collisions [8, 9]: When pairs of atoms residing on the same lattice site are illuminated with red-detuned molasses light, optical excitation causes the atoms to interact via strong dipole-dipole interactions. The kinetic energy released in one absorption/emission cycle causes atoms to leave the trap in pairs. At the high atomic densities in the deep pinning lattice, light-assisted collisions occur on fast timescale of $100\,\mu$s, and we image the *parity-projected* atom distribution: Sites with an initially odd number of atoms will retain one atom per site and appear bright in imaging, whereas sites with initially even occupation are entirely cleared of atoms and appear dark in imaging. There are hence only two outcomes (even or odd) of the imaging process on each site, and fitting the image with the amplitude of the measured PSF on each site yields a binary histogram [8]. Figure 3.2 shows a typical image obtained from a large thermal cloud of ^{87}Rb covering the entire field of view. Occupied and empty sites can be identified with a fidelity of $> 99\,\%$.

3.4 Generation of precise optical potentials

One of the challenges in working with lattices is the generation of precise and homogeneous optical potentials. A typical energy scale for our experiment is $J \approx 2\pi \times 100\,$Hz, and relevant energy gaps in many-body systems can be a small fraction of J, corresponding to only a few Hz. Lattice potentials, on the other hand, are up to $\sim 2\pi \times 50\,$kHz deep. Corrugations in the optical potential have to be suppressed to 1 part in 10^3 or better in order not to perturb the quantum states.

Coherent laser light, which is typically used in cold atom experiments, is particularly susceptible to potential corrugations. Any scatter off optics or dust particles in the beam

path interferes coherently with the desired light field and can cause large fractional errors in the potentials. A prime example are the concentric interference fringes often seen due to individual dust particles on optics.

Potential corrugations due to unwanted interference can be suppressed by using temporally or spatially incoherent light sources. Both techniques are used in our experiment.

Temporally incoherent light   The use of broadband, or temporally incoherent light greatly reduces unwanted interference effects. If the coherence length of the light is smaller than the typical physical separation between surfaces of optics in the experiment, partial reflections off those surfaces do not interfere with the desired light in the plane of the atoms. The unwanted light then adds in intensity, not in amplitude, to the target potential, causing much smaller corrugations than in the coherent case.

In our experiment, all conservative lattices are generated using temporally incoherent light at a central wavelength of $755\,$nm. The bandwidth of the light is $3\,$nm, corresponding to a coherence length $l_c = 190\,\mu$m. This is long enough such that all lattices interfere with full contrast. However, reflections from other surfaces, such as optics in the beam path or the glass chamber, are typically separated by several millimeters in optical path length, and reflections add incoherently to the desired field.

We use incoherent light derived from a superluminescent diode (Exalos EXS7510). The bandwidth of the light is set to $3\,$nm FWHM using interference filters, and then amplified using tapered amplifiers (Eagleyard EYP-TPA-0765-02000). We typically use one TA per lattice axis to produce $\sim 1.5\,$W of light on the optical table, of which $\sim 300\,$mW can be delivered to the atoms.

Spatially incoherent light   The use of temporally incoherent light cannot suppress errors due to scatterers directly in the beam path, such as dust particles on an optic. To work around this, spatially incoherent light sources can be used.

We have developed a spatially incoherent light source based on temporally incoherent light and custom-made etalons: A single temporally incoherent beam is split into ∼20 mutually incoherent beams within the etalon. The beams are combined on the atoms, but travel through different paths in the imaging setup, sampling independent disorder environments. Incoherently averaging over all paths greatly reduces the detrimental effect of dust, as we observed in test setups. So far, spatially incoherent light has only been implemented for the secondary z-lattice in the experiment, but might be implemented for other beams in the future. Full details and results are presented in [74].

3.5   Energy scales

The important parameters for Bose-Hubbard physics are the ground band tunneling J, the on-site interaction U, and the temperature T. The tunneling is exponentially sensitive to the depth of the 2D lattice V_{2D} and can be tuned over orders of magnitude from $J = 2\pi \times 0.07\,\text{Hz}$ ($V_{2D} = 45\,E_r$) to $J = 2\pi \times 220\,\text{Hz}$ at $V_{2D} = 1\,E_r$. The interaction U only depends weakly on the lattice depth along each direction as $\propto V^{1/4}$. In the deepest lattice $V_x = V_y = 45\,E_r$ and $\omega_z = 2\pi \times 5.9\,\text{kHz}$, the measured interaction is $U = 2\pi \times 480(30)\,\text{Hz}$. During state preparation, the ultracold cloud is subject to an additional harmonic confining potential, which sets the overall size of the system. In the superfluid regime, we use $\omega_{\text{harm}}/(2\pi) = 10 - 20$ Hz.

From the residual entropy of the sample we estimate the temperature at the superfluid-

insulator phase transition to be $T \approx 2\,\mathrm{nK}$, or $k_B T/\hbar \approx 2\pi \times 40\,\mathrm{Hz}$ [55]. The energy gaps to higher bands, both within the x–y plane as well as the z-direction, are typically larger than $2\pi \times 5\,\mathrm{kHz}$ and hence much bigger than all other energy scales, such that the ground-band Bose-Hubbard model gives an excellent description of the system.

3.6   Experimental sequence

Bose-Einstein condensation   The starting point for our experiment is a Bose-Einstein condensate of ^{87}Rb created using conventional methods. After loading a magneto-optical trap (MOT) with $\sim 10^9$ atoms at a temperature of $100\,\mu\mathrm{K}$, we perform free-space optical molasses cooling and magnetically transport the cloud to a UHV fused silica "science" cell using a series of quadrupole coils. We perform RF evaporative cooling in a QUIC trap for $23\,\mathrm{s}$ and obtain a nearly pure BEC of $\sim 10^5$ atoms in the low-field seeking state $|F, m_F\rangle = |1, -1\rangle$.

Lattice loading   After evaporation, the magnetic trap is reconfigured to obtain an almost spherical cloud with Thomas-Fermi radius $3\,\mu\mathrm{m}$, which is translated to its final position $10\,\mu\mathrm{m}$ below the substrate. We then compress the entire BEC into a single pancake-shaped two-dimensional cloud in a two-step process: First, we ramp on a secondary z-lattice with a spacing of $9.2\,\mu\mathrm{m}$. The large period helps capture all of the BEC in the first node of the lattice, where we achieve a vertical trapping frequency $\omega_z \approx 2\pi \times 2\,\mathrm{kHz}$. We then ramp on the axial lattice with a spacing of $1.5\,\mu\mathrm{m}$. All atoms are loaded from the long lattice into a single node of the short lattice, where a maximal trap frequency of $\omega_{\mathrm{axial}} \approx 2\pi \times 7.9\,\mathrm{kHz}$ can be achieved. At this point, the pancake-shaped cloud is confined vertically by the axial

lattice and in the x–y plane by the magnetic trap.

Dimple loading   We set the final atom number using an optical dimple: A tightly focused beam (waist $8\,\mu$m) of red-detuned temporally incoherent light at $840\,$nm forms a small attractive potential well at the center of the two-dimensional cloud. The magnetic trap is turned off, and all atoms not confined in the dimple are spilled from the trap. The remaining atoms, typically $100 - 500$, are released into a large harmonic trap with typical trap frequencies of $\omega_{\text{harm}} = 2\pi \times 20\,$Hz. The harmonic trap is formed by a blue-detuned Laguerre-Gauss ("doughnut") beam with waist $40\,\mu$m, which we create using a polymer vortex phase plate (RPC Photonics VPP-1a). The loading via the dimple potential reduces the entropy density of the remaining atoms and prepares a low-entropy superfluid with excellent number stability with RMS fluctuations as small as $2\,\%$.

Mott insulator formation   We drive a quantum phase transition between the superfluid and a Mott insulator in two dimensions by adiabatically ramping on the x–y square lattice. The ramp is exponential in depth with a time constant of $54\,$ms (base e) and typically ends at a lattice depth of $45\,E_r$.

3.7   Mott insulators

Our sequence prepares two-dimensional Mott insulators deep in the atomic regime with $U/J \approx 7 \times 10^3$. In this regime, atoms are localized to individual lattice sites with a well-defined number of atoms per site, and any remaining excitations within the Mott shells are thermal holes due to residual entropy of the cloud.
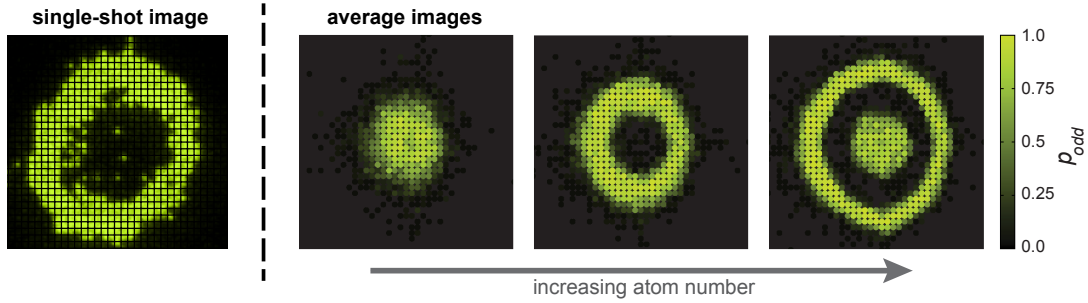
Figure 3.3: Site-resolved images of Mott insulators. Left: Single-shot raw image of a Mott insulator. Sites with $n = 1$ atoms per site form a bright ring around the dark center, where pairs of atoms are lost due to light-assisted collisions. Right: Averaged images of Mott insulators with increasing atom number showing the formation of the wedding cake structure.

Figure 3.3 shows a single-shot image of a Mott insulator in a harmonic trap with up to two particles per site. The picture reveals the well-known "wedding cake" structure: A ring of sites with one atom per site (bright) surrounds a dark core, which corresponds to sites with two particles per site, both of which are lost due to light-assisted collisions in the imaging process. The shell structure develops as the total number of atoms is increased (Figure 3.3). The cloud changes from one atom per site (all bright) via the two-shell Mott insulator to a wedding cake with up to three atoms per site, where parity projection causes an odd-even-odd structure of concentric rings.

An important metric is the fidelity of preparing a Mott insulator with the correct number per site. The fidelity is highest at the center of the shells, and typically best in the $n = 1$ regions. For optimized parameters, we can obtain single-site preparation fidelities of $99\,\%$. Typical fidelities for most experiments are $95\,\% - 98\,\%$ for extended regions. Mott insulating regions are the starting point for all experiments described in this thesis. Selecting a small area of the Mott insulator as a seed for few-particle experiments ensures very small number fluctuations and low configurational entropy.

Chapter 4

Single-atom addressing with holographically generated potentials

4.1 Introduction

A key advantage of atomic many-body systems over conventional condensed matter is the realization of strongly correlated phases at experimentally convenient time and length scales. In cold atomic systems, time-resolved, local detection methods enable the study of highly idealized scenarios, such as the dynamics of single particles or individual excitations. In particular quantum gas microscopes [8, 9] provide observations of individual quanta directly in their many-body environment.

Several approaches have been developed to also achieve *local control* in ultracold gases: in mixed-species experiments, high-resolution optical addressing has enabled studies of few-impurity systems [76]. Very commonly, radio frequency addressing in external or light-induced magnetic fields [77, 78] is used to address individual planes or sub-lattices.

33

In combination with high-resolution optical addressing, this technique has led to deterministic manipulation of individual atoms in three-dimensional large-spacing arrays [16] and in two-dimensional quantum gases in the Bose-Hubbard regime [15]. Even higher spatial resolution can be achieved with focused electron beams, which can clear atoms from individual sites in optical lattices [79].

While most of these addressing techniques rely on locally changing the internal state of individual quanta, we have developed a single-site addressing scheme with a complementary goal: Using the high resolution afforded by our quantum gas microscope, we are able to manipulate the *optical potential* experienced by the atoms on the length scale of a single lattice site. We superimpose arbitrary repulsive optical potentials onto an optical lattice, thereby controlling the chemical potential on each site. Our scheme enables the implementation of many interesting potential configurations, for example uniform box potentials or uncorrelated disorder, as well as highly controlled dynamics. The approach builds on a digital micromirror device (DMD) used as an amplitude hologram in a Fourier plane to generate re-programmable potentials.

4.2 Arbitrary potentials

One approach to creating arbitrary potentials is to project an image of the desired profile, either from a physical mask [80] or from spatial light modulators used to display gray scale images [81], onto the optical lattice. This method can be limited by aberrations in high-NA optical setups, preventing the creation of sharp, diffraction-limited features. The coherent laser light typically used is prone to the formation of speckle patterns due to unwanted coherent scattering in the imaging setup. It is therefore desirable to use temporally

and spatially incoherent light whenever possible [74], and this approach is best suited to create smooth, slowly-varying potentials on the atoms.

A complementary approach is to use coherent laser light and to precisely engineer the wavefronts defining the potential. Advanced wavefront engineering is afforded by holograms, which can fully control the amplitude and phase of complex wavefronts. Re-programmable holograms can be realized with modern optical elements: Spatial light modulators (SLMs) are high-resolution optical devices that control either the amplitude or phase of light on individual pixels and can be used to imprint complex patterns onto optical beams.

4.3 Digital holography

SLMs have been used to holographically create variable optical potentials for ultracold atoms by several groups [82, 83]. The typical approach is to place an LCD-based phase modulator in a Fourier plane of an imaging setup. The pixels of such devices imprint arbitrary phases on wavefronts in transmission and can be programmed to imprint the phase pattern of the Fourier transform of the desired potential. With optimization and feedback algorithms [83, 84], it is possible to create complex, re-programmable potentials. Several complications can arise with this method. Firstly, the LCD-based SLM only changes the phase of the transmitted wavefront, but not its amplitude. The precision in obtaining the correct potential after the Fourier transform performed by the imaging system is hence limited. Secondly, the aberrations in the imaging system are typically not known, and it is impossible to directly determine the exact potential in the location of the atoms. Thirdly, LCD-based devices switch the orientation of the phase-defining electric field in each pixel

35
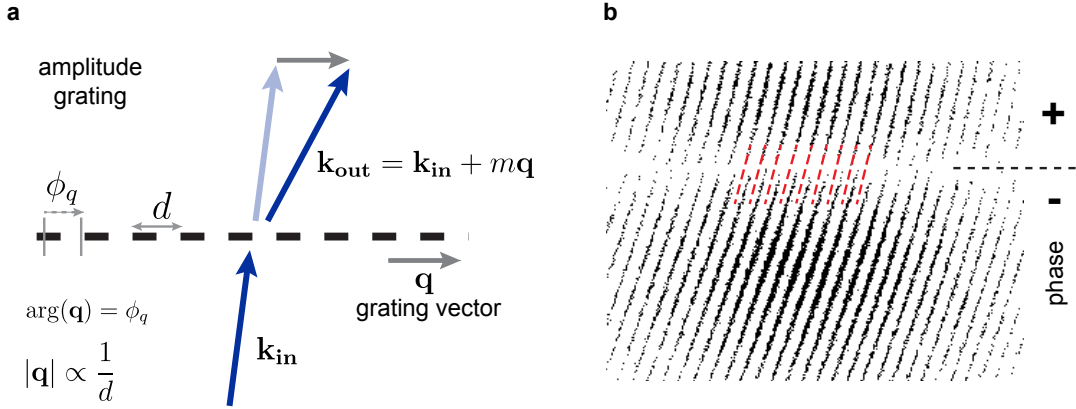
Figure 4.1: Holography with binary amplitude gratings. a) Locally, an amplitude grating changes the phase and angle of the diffracted light by adding m times the grating vector $\mathbf{q}$ to the mth diffraction order. The magnitude of the grating vector $\mathbf{q}$ is inversely proportional to the grating period, while the phase of vector is given by the spatial phase of the grating. The `on` fraction of the grating sets the amplitude of the outgoing wave. b) Detail of a hologram for Hermite-Gauss beams. Both the local phase and amplitude of the grating change across the beam profile (the grating lines are curved and vary in thickness), imprinting the desired phase and amplitude profile onto the beam. The π phase jump between the two regions of the hologram is emphasized by the red dashed lines.

at a frequency of several hundred Hz. This leads to significant heating due to intensity "blinking" and to small switching-induced errors in the potential.

In contrast, we use a digital micromirror device for wavefront engineering. DMDs are arrays of micron-sized mirrors that can rotate between an `on` and and `off` orientation. The displayed binary patterns are completely static, eliminating all problems with intensity noise due to the SLM. When used as an amplitude hologram, the DMD can define both phase and amplitude, and fully define the outgoing wavefront. Moreover, using a simple photodiode or a BEC as detectors, we can completely map out and compensate all aberrations in the imaging system and achieve near diffraction-limited potentials even in optical setups with aberrations of several λ. Similar approaches have been used in aberration com-

pensation for optical micromanipulation [85].

The concept of DMD-generated amplitude holograms is illustrated in Figure 4.1 a: We use the device in a Fourier plane to display a programmable binary diffraction grating. A plane wave scattered off the mirror array carries information about the displayed grating: The local k-vector of the grating determines the momentum transfer to the light, setting the angle of the outgoing light, while the phase of the scattered wave is set by the local spatial phase of the grating. The duty cycle or `on` fraction of the grating determines the amplitude of the outgoing wave.

Wavefronts of light can then be engineered by illuminating a large diffraction grating with a coherent beam. Varying both the phase and the amplitude of the grating locally imprints the underlying phase and amplitude information on the outgoing beam. Figure 4.1 b shows a detail of a grating used to generate high-order Hermite-Gauss beams [86]. The varying width and curvature of the grating lines (black) corresponds to local amplitude and phase modulation of the scattered field, respectively.

4.4 DMD physical setup

4.4.1 DMD device

DMDs consist of CMOS arrays of micromirrors on torsion hinges which can be switched between two angles corresponding to the `on` and `off` directions. DMD devices are typically used as image plane displays in high-end optical devices such as theater projectors, and are available with resolutions up to HD (1920×1080) and switching rates of $23\,\text{kHz}$. The device used in our experiment is the Keynote Photonics FlexLight X3, which uses the
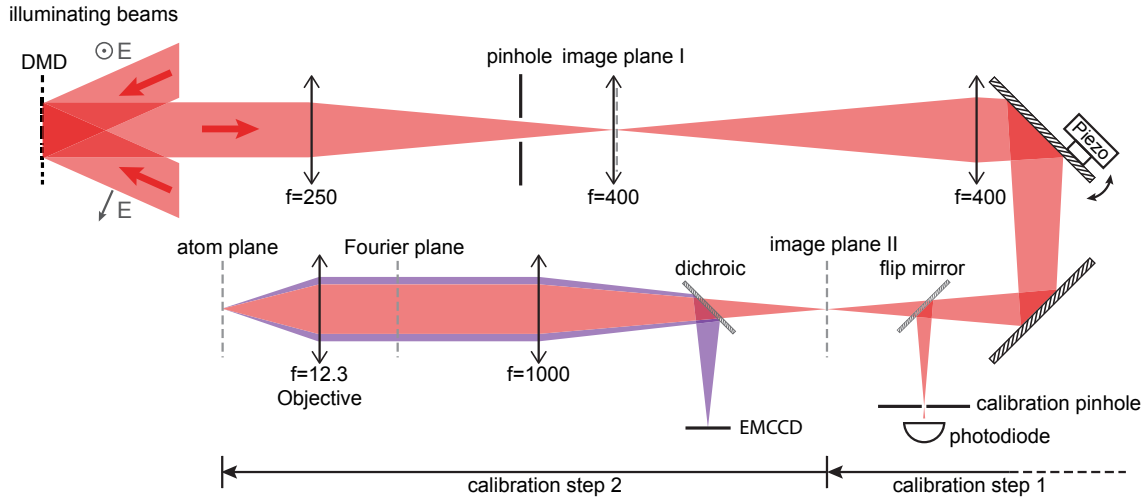
Figure 4.2: Schematic of the DMD optical path in the experiment. The DMD is illuminated with either a round or elliptical beam with orthogonal polarizations. The correct diffraction order is singled out with a pinhole, and the image of the desired potential formed in image plane I (IP I) is relayed to the atom plane with demagnification $\sim 1/80$. The field lens in IP I ensures that the DMD chip is imaged onto the objective back focal (Fourier) plane with magnification factor 4. The DMD is coupled into the microscope beam path (shown in purple) using a dichroic near the camera plane of the microscope (IP II). Aberrations to IP II are measured with a photodiode in IP II, while aberrations in the second part of the imaging path are calibrated using the atoms. A piezo-actuated mirror is used for position stabilization (see section 4.8).

Texas Instruments DLP 5500 chipset. The 1024×768 micromirror array has a pitch of $10.8\,\mu$m, micromirror angles $\pm 12°$ from normal, and an update rate of $5\,$kHz. The time required to switch between individual patterns is even shorter, on the order of a few μs, and dynamically deformable beams might be possible.

4.4.2 Optical setup

The optical path for the DMD in shown in Figure 4.2: The DMD is coupled into the microscope imaging path with a dichroic beamsplitter such that the DMD chip is imaged

onto the back focal plane of the microscope objective. The diameter of the effective aperture on the DMD chip is 500 pixels. The chip is illuminated from two directions at $\pm 24°$ from normal, respectively (see section 4.7). The light at $\lambda = 760$ nm is derived from a DFB (Eagleyard EYP-DFB-0760-00040), which generates 34 mW of light with a specified line width of 2 MHz. The light is then amplified with two stages of tapered amplifiers (Eagleyard EYP-TPA-0765-02000) in home-built mounts. After polarization cleanup on the optical table, up to 250 mW of intensity-stabilized light can be delivered to the DMD chip from either one of the illumination channels.

4.5   Calibration procedure

In order to achieve diffraction-limited potentials by pre-compensating wavefronts for aberrations in the optical setup, we need to calibrate the DMD with a full map of the aberrations of the optical path to the plane of the atoms.

An aberration-free lens system converts a plane wave in the Fourier plane to a converging spherical wave, subject to the limits of diffraction. Equivalently, paths from every point in the Fourier plane should interfere with the same phase at a point in the image plane to form a diffraction-limited spot. Aberrations constitute deviations from this condition, and can thus be mapped out by measuring phase differences between pairs of points in the Fourier plane, as shown in Figure 4.3 a for a simplified single-lens system. Turning on two small patches on the DMD creates two beams, which interfere to form a standing wave in the image plane. The spatial phase of the interference fringe is equal to the optical path length difference between the two patches on the DMD. Measuring the spatial phase of this interference pattern for pairs of patches covering the entire Fourier plane then gives a com-

39
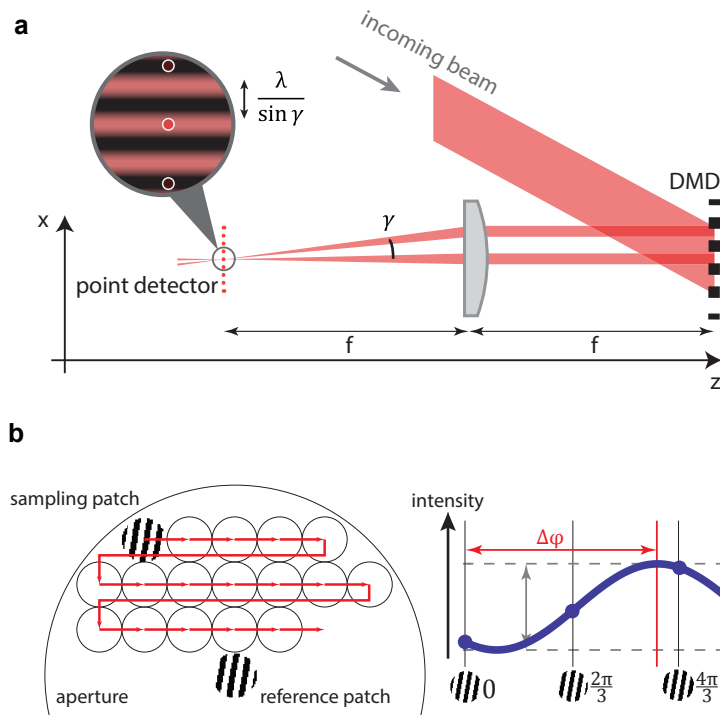
Figure 4.3: Self-calibration procedure of the DMD. a) Turning on two small patches on the DMD results in a fringe pattern in the image plane, whose spatial phase is equal to the optical path length difference between the two patches. The phase of the fringe can be recorded with a camera, or measured with a point detector, such as a photodiode or fluorescing ions or atoms. The beam path could be much more complex and contain many imperfect elements. b) Measuring aberrations with a point detector. Left: A patch at the DMD center remains as a static reference while a sampling patch is scanned across the aperture. Right: Shifting the phase of the sampling patch grating in steps of $2\pi/3$ physically moves the interference pattern across the point detector. Recording the point intensity for three phases for each sampling patch is sufficient to determine the amplitude and phase of the interference fringe, and hence to map out phase and amplitude across the Fourier plane. Figure reproduced with permission from reference [86].
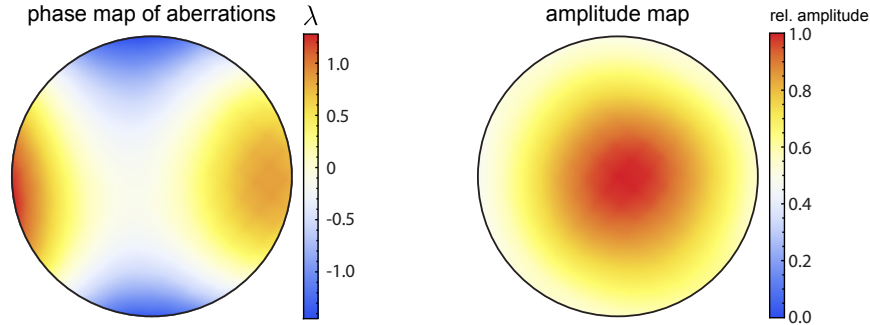
Figure 4.4: Intermediate image plane calibration. Phase and amplitude maps from a calibration with a photodiode in the intermediate image plane IP II. The phase map includes all aberrations in the illumination beams, the DMD itself, and optics in the beam path. Tilt and focus have been removed from the phase map, showing 3λ of astigmatism due to bending of the DMD chip itself. The amplitude map shows the Gaussian amplitude envelope of the round illuminating beam. To the edge of the aperture, the amplitude falls to 50% of its maximal value.

plete map of all aberrations. In our setup, this calibration of the aberrations is performed in two steps.

4.5.1   Intermediate plane calibration

We first calibrate all aberrations in the first part of the system with a photodiode in an intermediate image plane. A detailed description of this procedure can be found in the Master's thesis by Philip Zupancic [86]. Using a $10\,\mu$m pinhole, the photodiode samples a point on the interference pattern generated by two Fourier plane patches. By deliberately scanning the phase offset between the patches in steps of $2\pi/3$, full information about the amplitude and phase of the standing wave interference pattern can be obtained from three measurements of the photodiode voltage (Figure 4.3 b). Using the center of the Fourier

plane as a reference patch, we map out the phase for ~ 250 patches covering the entire aperture. The patch size of 35 pixels ($1/15$ of the aperture diameter) is a compromise between sampling aberrations on a sufficiently smooth scale and obtaining enough power from each patch. This part of the calibration is fast and can be performed with a good signal-to-noise ratio, yielding typical wavefront flatness of $\lambda/40$ RMS. The measured phase maps include aberrations present on the beams illuminating the DMD chip, unevenness in the chip itself, and aberrations induced by all optics in the beam path up to the photodiode plane. The phase map shown in Figure 4.4 displays mainly astigmatism caused by deformation of the DMD chip in the manufacturing process. From the interference contrast on the photodiode we also obtain an amplitude map of the beams illuminating the DMD in order to account for the non-uniform illumination. This first part of the calibration ensures diffraction-limited performance in the intermediate image plane IP II, corresponding to the EMCCD camera, as shown in Figure 4.2.

4.5.2 Calibration to the atoms

In a second calibration step we measure aberrations in the beam path between the intermediate image plane IP II and the plane of the atoms, which includes the high-NA objective. Because it is not possible to directly image the interference pattern or to place a photodiode in the plane of the atoms, we need to use the atoms themselves to map out aberrations.

To this end, we prepare a weakly interacting superfluid of ~ 400 atoms in a shallow two-dimensional lattice of depth $1\,E_r$. We then adiabatically turn on the DMD beam while displaying a hologram of two patches spaced by $1/5$ of the aperture. The atoms experience a repulsive standing-wave pattern of period 3.7 sites and arrange themselves in the
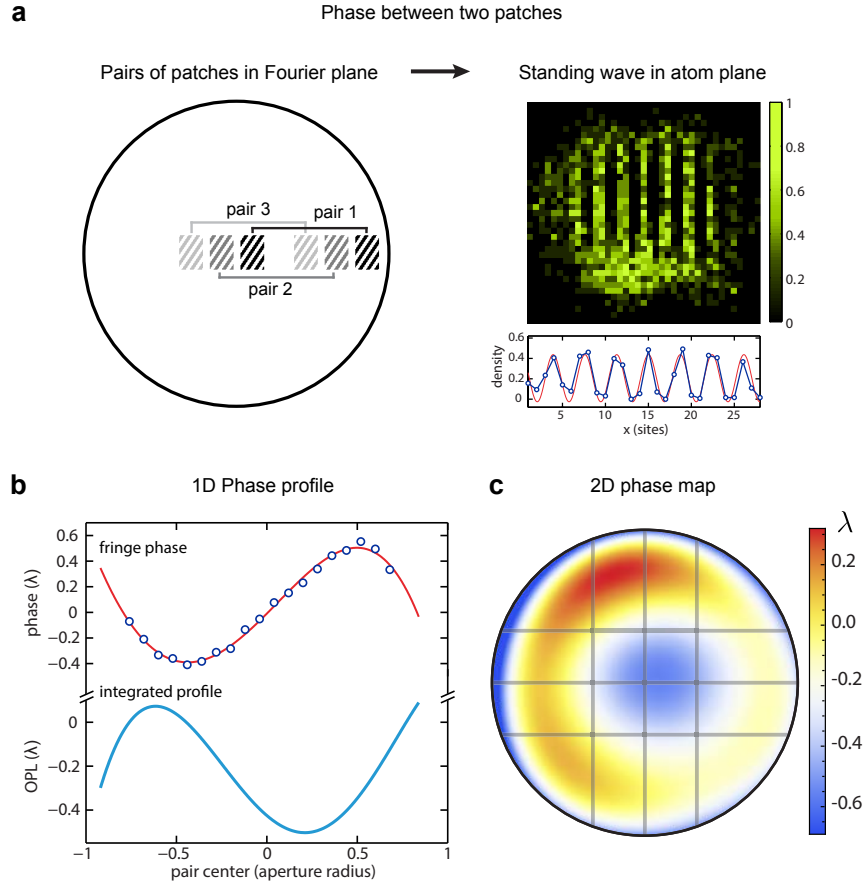
Figure 4.5: Aberrations in the microscope setup. In the second step of measuring aberrations, a BEC is used to map out interference patterns directly in the plane of the atoms. a) Pairs of patches (left, shown in different gray scales) produce a standing wave, forcing the atoms to its minima and revealing the optical path length (OPL) difference between the patches as the phase of the averaged density wave (right). b) Translating the pair of patches across the Fourier plane, the changing standing wave phase reveals the aberrations sampled by each pair. Data points are measured fringe phases at the center location of the patch pairs, red is a fit with a 5th order polynomial. Light blue is the reconstructed phase profile. The width of the plotted profile indicates the range of the aperture over which the reconstruction in valid. c) A smooth phase map is interpolated from six measured phase profiles (gray lines). The dominant aberrations are spherical terms from the flat surface of the hemispherical lens. Tilt and focus have been removed from the phase map.

minima of the DMD-generated potential. Because the potential results in an overall deconfinement, we simultaneously increase the trap frequency of the harmonic trap from initially $\omega_{\mathrm{harm}} \approx 2\pi \times 20\,\mathrm{Hz}$ to $\omega_{\mathrm{harm}} \approx 2\pi \times 50\,\mathrm{Hz}$ in order to keep the cloud size constant. Images of the cloud directly reveal the phase difference between the two hologram patches on the DMD, as shown in Figure 4.5 a. By averaging ~ 10 images and fitting the integrated density profile, we can determine the relative phase with a typical uncertainty of $\pm 0.2\,\mathrm{rad}$.

We map out the aberrations across the entire aperture by repeating the experiment with different pairs of patches. The spacing between the patches and hence the spacing of the interference pattern on the atoms remains fixed while the two patches are translated across the Fourier plane in steps of $1/25$ of the aperture diameter. We repeat this procedure along different paths and obtain six phase profile "cuts" through the Fourier plane, as shown in Figure 4.5. The phase profile across the entire DMD aperture is then constructed by fitting a two-dimensional surface parameterized by Zernike polynomials to the six phase profiles. We allow Zernike polynomials up to radial order 4 and azimuthal order 3. An example of a fitted phase map is shown in Figure 4.5 c. We verify the accuracy of the phase calibration map by correcting the wavefront for aberrations and measuring the six phase cuts again. Typical deviations from an expected flat wavefront are $\lambda/6$ peak-to-peak, caused by differences between the six measured phase profiles and the fitted two-dimensional surface. Improving the fitting algorithm or using a more uniform sampling of the Fourier plane might improve the accuracy of the second calibration step.

The full set of calibration data consists of amplitude maps of the illuminating beams as well as summed phase maps for the intermediate and atom plane calibrations. The overall phase error of typically $\lambda/6$ is dominated by uncertainties in the calibration to the atom
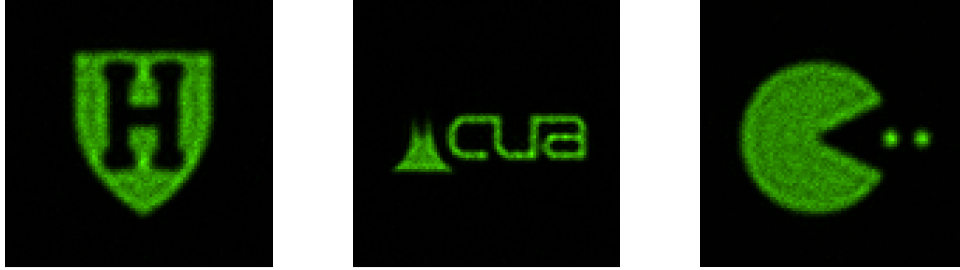
Figure 4.6: Arbitrary beam shaping. Complex beam profiles are generated by numerically Fourier transforming the desired wavefront in the image plane and displaying the amplitude and aberration-corrected phase profile on the DMD. Figure reproduced with permission from reference [86].

plane. For applications in other experiments, for example addressing of individual trapped ions, aberrations could be measured in situ by using the fluorescence from individual ions as point detectors equivalent to the photodiode in our first calibration step.

4.6 Arbitrary waveforms

With the calibrated DMD, almost arbitrary beam shapes can be generated. The holograms required to generate a desired beam profile in the atom plane are calculated numerically [86]. First the appropriate phase and amplitude profiles in the Fourier plane are obtained as the Fourier transform of the desired wavefront in the image plane. Corrections due to the vector nature of light and the breakdown of the paraxial approximation, which are in principle required at an NA of 0.8, have not been limiting so far and are neglected in this calculation. In a second step the binary hologram itself is created, accounting for the measured phase and amplitude calibration maps.

For each pixel, we assign a local phase and amplitude with a suitable carrier vector k_0 to place the image in the correct location in the atom plane [86]. To minimize artifacts

associated with binarization errors at discrete k-vectors, a probabilistic approach is chosen to assign `on` or `off` values to each pixel when a binary hologram pattern is created [86]. Figure 4.6 shows some interesting beam shapes generated in a test setup.

4.7   Power efficiency

A drawback of using the DMD as an amplitude hologram in the Fourier plane is its poor power efficiency. The periodic array of micromirrors splits the incident light into many diffraction orders, both due to the underlying pixel array with pitch $p = 10.8\,\mu$m and the displayed amplitude grating with typical carrier spatial periods of five pixels or $d = 55\,\mu$m. Only the beam corresponding to the $+1$ order carries the proper phase and amplitude information and remains as useful power, which is separated from the other orders using an iris. The power in this desired diffraction order can be maximized by fulfilling the "blazing condition": The angle of illumination is chosen such that a diffraction order of the underlying pixel grating is overlapped with the `on` direction of each individual mirror.

The overall power efficiency of the DMD, including illumination light lost outside the effective aperture, is thus $1 - 2\,\%$. Of the $250\,$mW of incident power on the DMD, $4\,$mW remain in the correct diffraction order. Taking into account additional optics in the beam path, the maximal deliverable power to the atoms is $900\,\mu$W, corresponding to an area-integrated Stark shift of $2\pi \times 45\,$MHz $\times\,(\text{site})^2$ for ^{87}Rb at a wavelength of $\lambda = 760\,$nm.

The considerations above assume that all of the aperture on the DMD is being used, which is not always the case. Consider the case of a Gaussian spot in the plane of the atoms: For a waist of $w \approx 1$ site, the DMD hologram covers almost all of the Fourier plane

and the maximum possible power is used. If the waist of the Gaussian is increased, the active area in the Fourier plane and hence the power in the beam scales as $1/w^2$, which is distributed across the beam cross-section $\propto w^2$. The intensity in the Gaussian hence scales dramatically as $I \propto w^{-4}$, and for current parameters it is unrealistic to make useful patterns larger than 10×10 lattice sites.

Some of the power loss caused by the poor match between the shape of typically used holograms and the illumination beam can be avoided by appropriately shaping the illumination beam. In the experiment, we often use line-shaped potentials with aspect ratios $>$10:1. The corresponding holograms on the DMD chip have the inverse aspect ratio 1:10, and cover only a narrow strip of the effective aperture on the chip. In addition to a round illumination beam (waist $3.2\,\text{mm}$), which is used for patterns that cover the entire Fourier plane, we also use an elliptical illumination beam. This cylindrical beam has waists $0.8\,\text{mm}$ and $3.2\,\text{mm}$ and is used for patterns that require large momentum components only along one direction. The polarization of each beam is chosen to achieve maximal interference contrast along the respective large-momentum direction (section 4.9). The two beams illuminate the DMD symmetrically from $\pm24°$ from normal, respectively, such that they each satisfy the blazing condition. The definition of `on` and `off` is reversed between the two beams. Separate phase and amplitude calibration maps are obtained for the two beams using the same pinhole, ensuring that aberrations in each beam are properly compensated and the beams are perfectly overlapped in the image plane.

4.8 Pointing stability

A critical characteristic of the single-site addressing scheme is its position stability with respect to the optical lattice. For typical applications we need the relative alignment to be accurate and stable to ~ 0.2 sites or better. We identified two main sources of pointing noise: On timescales of $0.2 - 2\,\mathrm{Hz}$, the stability of the addressing beam is limited by air currents on the optical table. We therefore enclosed the optical path with additional curtains and shields wherever possible. On longer timescales, we observe thermal drifts of up to 1 site/hour. To compensate for this drift during data sets, we feed back on the position of the addressing beam with respect to the lattice: At the end of each experimental run, we image reflections from the substrate close to the atoms on a camera, capturing the optical lattice and a small dot generated by the DMD. We fit the position of the beams and compensate any drifts for the next run of the experiment with a piezo-controlled mirror in the beam path (Figure 4.2). With the feedback enabled, we achieve relative position errors of ~ 0.04 sites RMS, which is sufficient for our current experiments.

4.9 Limitations

High-NA effects Our current method of generating holograms as the Fourier transform of the desired potential assumes the paraxial approximation holds. For holograms that use the full NA of the imaging system, this simplification causes errors, as shown in Figure 4.7: The actual potential deviates significantly from the desired outcome, in particular if the polarization of the light is chosen incorrectly, as components of the electric field out of the atom plane lead to reduced interference contrast. We always chose the correct polarization
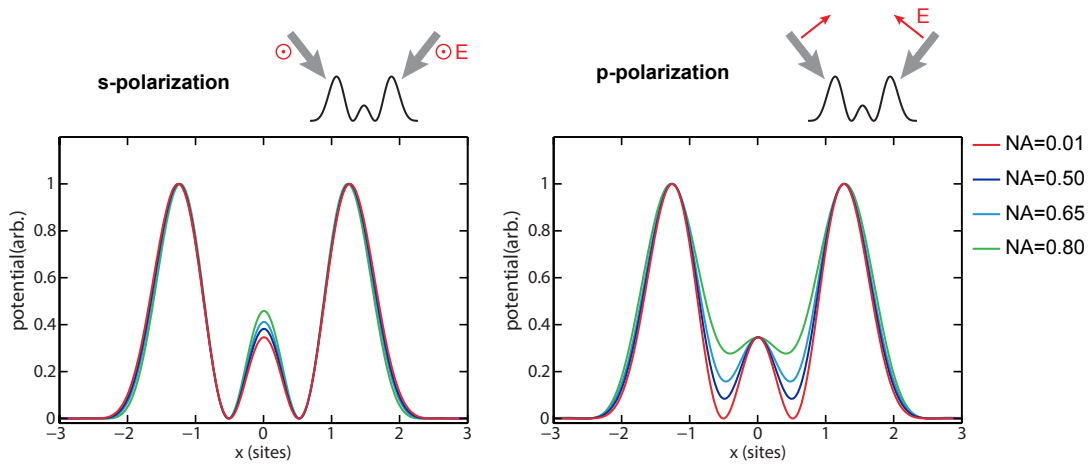
Figure 4.7: Polarization effects at large numerical aperture. Small-feature potentials should be created with s-polarized light, with the polarization vector in the plane of the atoms and full interference contrast. For p-polarized light, components of the light at large angles from the optical axis have close to orthogonal polarizations and do not interfere. The functional form of the potential, here a double-well, changes dramatically with increasing NA. The potentials are scaled to the same peak height for each curve. Numerical simulations implemented by Ruichao Ma based on reference [87].

for patterns with small features, but have not implemented an algorithm to generate fully accurate potentials at high NA.

Digitization   The noise on beam profiles is set by the finite resolution of the DMD. We measure an intensity noise floor of about 10^{-4} in our applications. Errors on the beam profiles can be significantly larger. Figure 4.8 illustrates the error for a potential with seven sharp Gaussian peaks. The hologram in Fourier space covers a narrow strip on the DMD chip, using $\sim 2,500$ of the $\sim 200,000$ pixels in the aperture. An estimate of the error due to digitization can be obtained by a numerical Fourier transform of the binary hologram. In this case, differences of several percent of the peak intensity between the desired and the actual potential are expected.
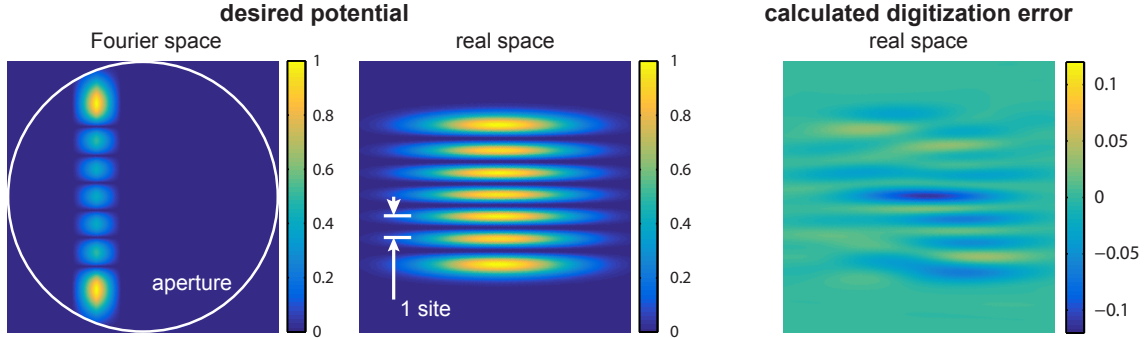
Figure 4.8: Digitization error. Left: Potentials with sharp real space features in one dimension and smooth profiles in the perpendicular direction use small areas of the DMD chip. The pattern shown here is defined by $\sim 2,500$ `on` pixels. Right: The expected binarization error for a particular hologram in units of the peak intensity. For this pattern, deviations from the desired potential on the order of a few percent are expected. The precise error depends on the probabilistic assignment of `off` and `on` pixels, and varies between realizations of the same hologram.

4.10   Single-atom addressing

The fully calibrated DMD can generate arbitrary repulsive potentials with depths comparable to the optical lattice. While many possible potentials can be displayed, the DMD used holographically in a Fourier plane is best suited to produce small, high-momentum potentials in the image plane.

4.10.1   State initialization

We use the single-site addressing scheme to initialize few-particle Fock states in a lattice by "cutting" individual atoms from Mott insulator states (Figure 4.9). We prepare a Mott insulator with one particle per site in the atomic limit $U \gg J$ in a two-dimensional lattice with $V_x = V_y = 45\,E_r$. The DMD then superimposes a beam with Hermite-Gauss profile in the transverse direction and a flattop profile along the longitudinal direction (length
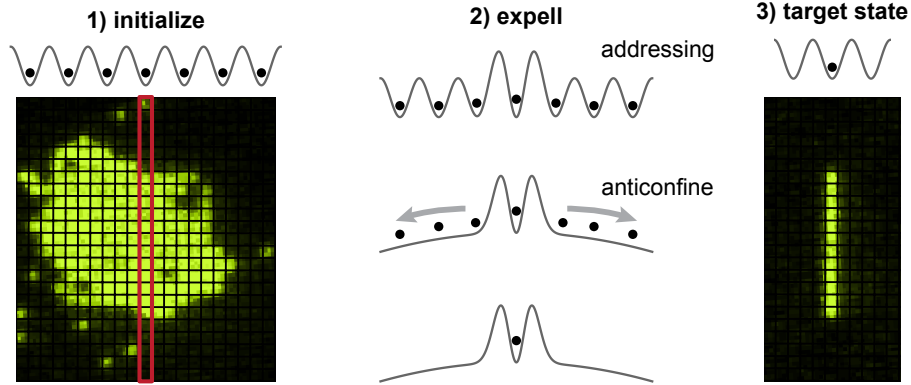
Figure 4.9: "Cutting" atoms out of a Mott insulator: An addressing beam with a repulsive Hermite-Gauss profile is superimposed onto a Mott insulator in a $45\,E_r$ optical lattice. A column of atoms is pinned in the minimum of the addressing beam while the transverse lattice is turned off and a deconfining Gaussian beam expels all other atoms. The pinned atoms are then loaded back into the optical lattice. By choosing higher orders of the addressing Hermite-Gauss beam, up to six adjacent columns can be prepared.

$10\,\mu$m). The distance between the peaks of the Hermite-Gauss profile is $930\,$nm, with a typical peak depth of $25\,E_r$. We switch off the transverse lattice in the presence of a large ($40\,\mu$m waist) anti-confining Gaussian beam at $760\,$nm. Only atoms in rows coinciding with the nodes of the Hermite-Gauss beam are retained, while all other atoms are expelled from the system within $40\,$ms before the transverse lattice is ramped back on. We thus deterministically prepare one row of atoms (length ≈ 10 sites). This cutting procedure retains atoms pinned by the DMD with a probability of $99(1)\,\%$, and the fidelity of preparing one atom per site is limited by the initialization fidelity of the Mott insulator, typically $\geq 98\%$.

The cutting procedure works with near perfect fidelity irrespective of the number of atoms on a particular site and can be carried out sequentially along both lattice directions in order to produce single, isolated plaquette systems of sizes up to $2{\times}6$, where the occupation of each site is controlled via the initial occupation in the Mott insulator.
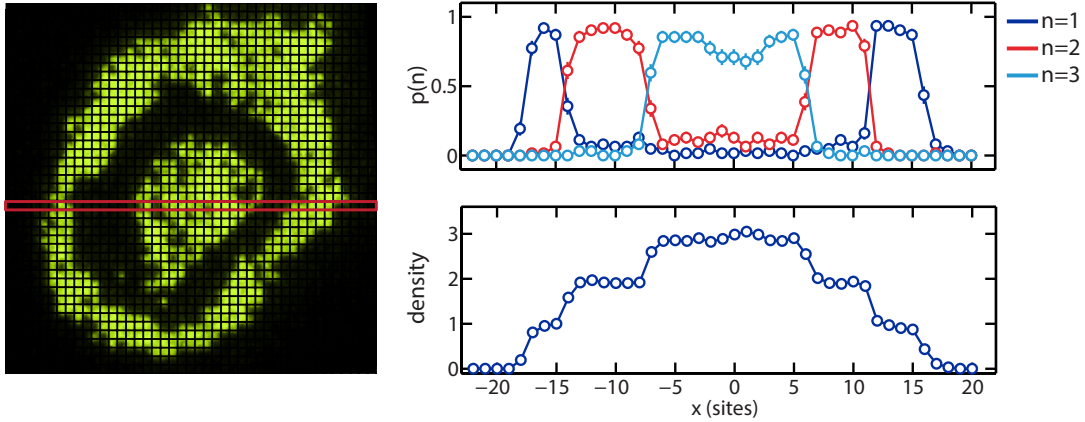
Figure 4.10: Full counting statistics in one dimension. Left: A Mott insulator with up to $n = 3$ atoms near the center appears as three concentric rings in parity-projecting fluorescence imaging. A single row of atoms (red box) can be cut from the Mott insulator and all atoms are detected after a short vertical expansion. Right: We obtain the full density profile and number statistics for each site in the one-dimensional profile.

4.10.2 Full counting statistics

Our method of isolating well-defined subsystems from a many-body state can be used to circumvent the parity projection in fluorescence imaging. This procedure is shown in Figure 4.10: A large Mott insulator with up to three atoms per site appears as a ring of concentric bright and dark rings when imaged in situ, corresponding to odd and even occupancy, respectively. To circumvent parity projection, we can cut one row of atoms from the Mott insulator, emptying all other sites. Before imaging, we turn off the DMD addressing beam and release the atoms into one-dimensional tubes transverse to the cut, performing a ~ 5 ms time-of-flight measurement in the vertical direction. Sites near the center of the Mott insulator contain more than one atom initially, which separate during the transverse time of flight and are imaged individually without being lost to parity projection. Summing counts along vertical tubes then yields the full number statistics of the one-dimensional cut

52

through the two-dimensional system. Figure 4.10 shows these results for an $n = 3$ Mott insulator, directly revealing the wedding cake structure and site-resolved number distributions.

The full number statistics obtained through the "cut and count" procedure contain all the information to construct high-order number correlation functions between all sites. Such measurements are ideal for characterizing density correlations, for example in one-dimensional impurity problems [88], or to detect entanglement through number fluctuations [89]. In combination with a transverse magnetic field gradient [90], it is possible to obtain fully spin- and number-resolved readout of one-dimensional, two-component quantum gases.

Part II

Interactions and quantum statistics in few-particle dynamics

Chapter 5

Quantum walks of strongly interacting bosons

Portions of this chapter have appeared in:

5.1   Introduction

One of the fundamental processes in physics is the random walk. Its simplest one-dimensional realization is a particle that is initialized to a particular point in space and randomly takes steps in either direction with equal probability. In the classical case, this setting leads to diffusion: The density distribution of such a particle expands as the square root of time and displays slow growth of the Gaussian probability distribution. A quantum particle, on the other hand, can take many paths at the same time, and the overall dynam-

ics of the particle will be governed by a coherent, simultaneous sampling of large parts of the system. Indeed, the quantum walker's wavefunction will expand linearly in time, displaying very different, ballistic behavior.

This stark contrast between the classical and quantum behavior points to the importance of the quantum walk as a basic probe of quantum dynamics. Many different scenarios have been considered theoretically and experimentally, and two distinct models of quantum walk with similar physical behavior were devised: The discrete time quantum walk [39], in which the particle propagates in discrete steps determined by a dynamic internal degree of freedom, and the continuous time quantum walk [40], in which the dynamics is described by a time-independent lattice Hamiltonian. Both frameworks provide descriptions of fundamental quantum transport.

The single particle quantum walk in either implementation is straightforward to treat, as it is described by classical wave equations. More interesting situations can be accessed when several indistinguishable particles perform quantum walks simultaneously. In such cases, quantum correlations can develop as a consequence of Hanbury Brown-Twiss (HBT) interference and quantum statistics, as was investigated theoretically [91, 92] and experimentally (see [93] and references therein). This problem is believed to lack full quantum complexity in the absence of interactions or auxiliary feed-forward measurements of the Knill-Laflamme-Milburn type [94], but can become intractable by classical computing [92].

The full complexity of quantum walks can be realized when interactions between indistinguishable quantum walkers are strong [95, 96]. Such interacting quantum walks provide a general framework for the exploration of many-body dynamics and the study of compu-

tationally hard and outstanding condensed matter problems, for example the dynamics of quantum disordered systems [97].

In this chapter I report on the experimental implementation of quantum walks of strongly interacting bosons: Using the naturally present interactions and the deterministic preparation of indistinguishable bosons in our quantum gas microscope, we study continuous single-particle and two-particle quantum walks in the regime where the dynamics are dominated by interactions. We show that strongly correlated quantum walks directly probe fundamental processes from quantum many-body physics, such as the fermionization of bosons and the formation and coherent propagation of repulsively bound pairs.

5.2   Quantum information processing and quantum walks

Considerable theoretical interest in quantum walks stems from the quantum information processing community [41]. It was realized early on that a particle performing a random walk on an arbitrary graph can be viewed as a basic unit of computation. A quantum particle can sample many paths through the graph simultaneously, and approach certain limits faster than a classical particle, leading for example to faster "hitting times" for the propagation to the boundary of a graph [40]. This enhanced propagation is the origin of a potential "quantum speedup" in random-walk based computation.

An example of this quantum enhancement is the problem of "boson sampling" [93]: Consider an n-port device that performs a random unitary operation on all of its inputs. It is strongly believed that computing the output generated from initializing this device with n indistinguishable non-interacting bosons is a classically hard problem [92], i.e. the required computational resources grow exponentially in n. On the other hand, it is clear

that n bosonic particles undergoing a simultaneous quantum walk, for example n photons in a simple multiport beamsplitter, provide a direct implementation of this scenario. This problem is now considered a prime example for the outperformance of classical computers by quantum devices, and has received a lot of theoretical and experimental attention [98].

More remarkably, it was shown recently that quantum walks can be used to implement universal and efficient quantum computation [99] if interactions between the quantum walkers are present, for example in Bose-Hubbard systems. While these considerations are still relatively abstract, quantum walks have turned into an active field of research at the interface of condensed matter physics and quantum information processing.

5.3 Quantum walks in atomic and optical systems

Experimentally, quantum walks have been implemented on a number of platforms (see reference [17] for a review). Using an internal state as a quantum "coin" state, cold trapped ions [100, 101] and neutral atoms in state-dependent lattices [102] can realize discrete quantum walks. Continuous quantum walks have been implemented for individual atoms [15] and for effective spin models in optical lattices [61] and trapped ion chains [103]. Significant progress has been made in implementing quantum walks in photonic systems due to outstanding coherence properties and the development of high-quality waveguide arrays on silica substrates [17]. Such devices offer great flexibility and control in defining the dynamics through integrated beamsplitters, phase shifters and controlled disorder [3]. Photonic quantum walks have been used to classically simulate the quantum walks of two interacting bosons by engineering effective interactions through conditional phase shifts in fiber networks or waveguide arrays [104, 105]. Progress to much more complex systems

58

with photonic quantum walks is currently hindered by the difficulty of generating many indistinguishable photons, which requires cascaded parametric downconversion [98], and the difficulty of engineering effective interactions at the level of single photons [17].

5.4 Experimental implementation

In our experiment, bosonic atoms perform quantum walks in decoupled one-dimensional tubes of the optical lattice. The atoms may tunnel in the x-direction with amplitude J and experience a repulsive on-site interaction U, realizing the Bose-Hubbard Hamiltonian 2.3 together with a potential gradient:

$$H = \sum_{\langle i,j \rangle} -J a_i^\dagger a_j + \sum_i \frac{U}{2} n_i(n_i - 1) + \sum_i E\,i\,n_i. \tag{5.1}$$

The values of J and U are tunable via the depth V_x of the optical lattice and the energy shift per lattice site E is set by a magnetic field gradient. We measure time in units of inverse tunneling rates, $\tau = tJ$, and define the dimensionless interaction $u = U/J$ and gradient $\Delta = E/J$.

We set the initial motional state of the atoms through the single-site addressing scheme described in chapter 4. Starting from a low-entropy two-dimensional Mott insulator with a fixed number of atoms per site, we prepare one or two rows of atoms along the y-direction of a deep optical lattice with $V_x = V_y = 45\,E_r$ (Figure 5.1). The quantum walk is performed at a reduced lattice depth V_x, while the y-lattice and the out-of-plane confinement are fixed at $V_y = 45E_r$ and $\omega_z = 2\pi \times 7.2\,\mathrm{kHz}$, respectively. The atom positions are recorded with single-site resolution using fluorescence imaging in a deep optical lattice [8].
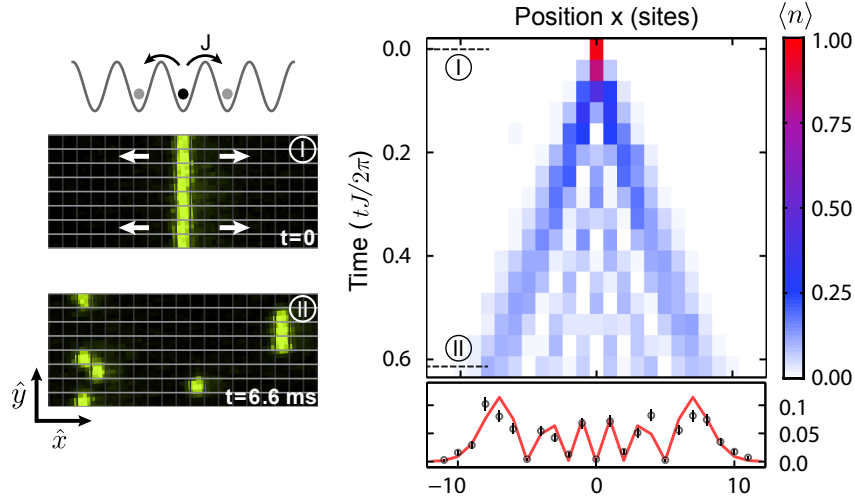
Figure 5.1: Single-particle quantum walks. Left: Starting from a Mott insulator, we deterministically prepare individual atoms in horizontal tubes of an optical lattice, separated by a deep lattice in the y-direction. From the localized initial state (I) atoms perform independent quantum walks in the x-direction (II). Right: The single-particle density distribution expands linearly in time, and atoms coherently delocalize over ~20 sites. The lower panel shows the averaged density distribution at the end of the quantum walk and a fit to equation (5.2) with the tunneling rate J as a free parameter. Densities are averages over ~700 outcomes.

5.5 Single-particle quantum walks

We first consider quantum walks of individual atoms (Figure 5.1). A single particle is initialized at a chosen site in each horizontal tube and propagates in the absence of external forcing ($\Delta = 0$). For each individual realization the particle is detected on a single lattice site, while the average over many experiments yields the single-particle probability distribution. In contrast to a classical random walk, for which slow, diffusive expansion of the Gaussian density distribution is expected, coherent interference of all single-particle paths leads to ballistic transport with well-defined wavefronts. The measured probability density $\langle n \rangle$ expands linearly in time (Figure 5.1, right panel), in good agreement with the
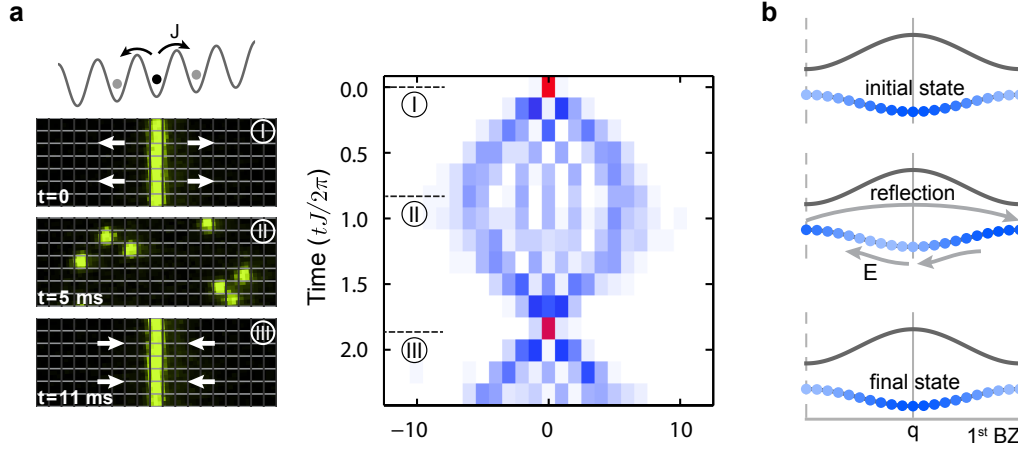
Figure 5.2: Single-particle Bloch oscillations in position space. a) In the presence of a gradient, a single particle undergoes Bloch oscillations. Starting from a localized initial state (I), each atom initially delocalizes (II) but maintains coherence and re-converges to its initial position after one period (III). The averaged density shows an oscillatory breathing motion with a high-fidelity revival. Densities are averages over ~200 realizations. b) Momentum space representation of single-particle Bloch oscillations. Initially, the particle is in a superposition of all momentum states within the first Brillouin zone (shaded to indicate their initial momentum). The external force E and Bragg reflection at the zone boundary cycle each momentum component through the Brillouin zone. After one oscillation, the initial state is recovered.

theoretical expectation [106]

$$\langle n_i \rangle = |\mathcal{J}_i(2Jt)|^2 \tag{5.2}$$

for lattice site i, where $\mathcal{J}_i$ is a Bessel function of the first kind and order i. At the end of the quantum walk, each particle is delocalized over almost $15\,\mu$m without appreciable signatures of decoherence.

5.6 Position-space Bloch oscillations

The light-cone like delocalization of a single particle performing a quantum walk is a strong indication that the propagation is indeed unitary. The degree of coherence can be verified by subjecting the particle to a potential gradient. Despite the strong external force, there is no net transport through the optical lattice: The maximum kinetic energy of the particle is set by the bandwidth of the lowest band, and in the absence of dissipation or excitations to higher bands, energy conservation prohibits the particle from propagating in the direction of the force while converting potential energy to kinetic energy. Instead, the potential gradient induces a position-dependent phase shift and causes atoms to undergo Bloch oscillations [107]. For a fully coherent single-particle quantum walk with gradient Δ, the atom remains localized to a small volume and performs a periodic breathing motion in position space [106, 108, 109, 110] with a maximal half width $L_B = 4/\Delta$ and temporal period $T_B = 2\pi/\Delta$ in units of the inverse tunneling. Figure 5.2 a shows a single-particle quantum walk with $\Delta = 0.56$, resulting in Bloch oscillations over ~ 14 lattice sites. A semiclassical explanation of the breathing motion is given in Figure 5.2 b: Initially, the particle is tightly localized in a superposition of all momentum eigenstates within the first Brillouin zone and its wavefunction fills the entire band. An external force now translates each momentum component through the Brillouin zone, leading to temporary delocalization of the particle in real space. At the Brillouin zone boundary, momentum components are Bragg scattered by a reciprocal lattice vector. After one period all components of the wavefunction have cycled through the Brillouin zone once and returned to their original quasimomentum modulo a common phase factor. The original wavefunction is hence restored, and the particle is localized again at the origin.

The refocusing of the single-particle wavefunction relies on the interference of different momentum components and hence provides a metric for the degree of coherence of the dynamics. In the experiment, we observe a high quality revival after one Bloch period and detect the particle back at the origin with a probability of up to 0.96(3) at $\tau = T_B$ in individual tubes. The average over six adjacent rows in Figure 5.2 a displays a revival probability of 0.88(2), limited by the timing of the measurements and broadening across different rows due to inhomogeneities in the lattice and the gradient . The fidelity,

$$f(t) = \sum_i \sqrt{n_i(t)\rho_i(t)} \tag{5.3}$$

for the measured and expected probability distributions $n_i(t)$ and $\rho_i(t)$, averaged over ~ 1.5 Bloch oscillations is $98.1(1)\,\%$, indicating that a high level of coherence is maintained while the particle delocalizes over $\sim 10\,\mu$m in the optical lattice.

The fidelity of the revival after many Bloch oscillations will eventually be limited by two factors. Firstly, spontaneous scattering of lattice photons leads to localization of the particle and a crossover to classical diffusive behavior at long times [111]. Secondly, even for fully coherent motion, weak additional potentials such as residual harmonic confinement cause gradual damping of the oscillations and can lead to a destruction of the revivals.

5.7   Hanbury Brown-Twiss interference

We now turn to simultaneous quantum walks of two particles. Even in the absence of interactions, quantum correlations and entanglement can emerge due to Hanbury Brown-Twiss interference of indistinguishable particles [112].

The concept of two-particle HBT interference is illustrated in Figure 5.3. Two indistin-
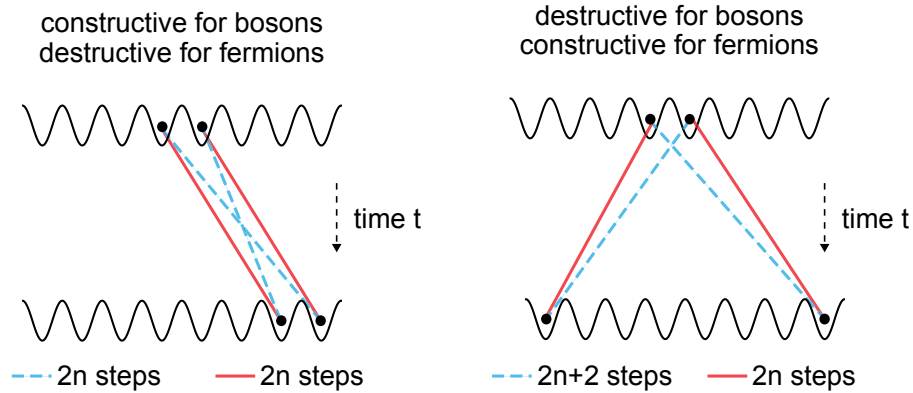
Figure 5.3: Hanbury Brown-Twiss interference. All processes connecting the initial and final states of indistinguishable particles interfere coherently. Each tunneling step contributes a phase i. For non-interacting bosons, processes of the same length add constructively (left), while processes differing in length by two steps interfere destructively (right). Particle exchange contributes an extra phase π for fermions, and the interference amplitudes are reversed. The resulting bosonic "bunching" and fermionic "anti-bunching" are unique signatures of the underlying statistics.

guishable particles emerge from two sources, in this case adjacent lattice sites. After some

evolution time, both particles are detected in a particular configuration in the optical lattice,

which can be thought of as two "clicks" in detectors on individual lattice sites. Since the

particles are indistinguishable, there is fundamentally no way to tell which source the par-

ticles registered at a particular detector emerged from. It is therefore necessary to add all

two-particle processes that connect the initial to the final state coherently to determine the

overall amplitude. Since each tunneling step in the lattice is associated with a phase factor

i, the relative phase between two-particle processes can be obtained from simply counting

the number of tunneling steps involved. The processes connecting to a final state with the

particles in close proximity to each other contain the same number of steps, and for bosonic

particles interfere constructively. Processes placing the two particles on opposite ends of

the lattice, on the other hand, differ in length by two steps and hence interfere destructively.
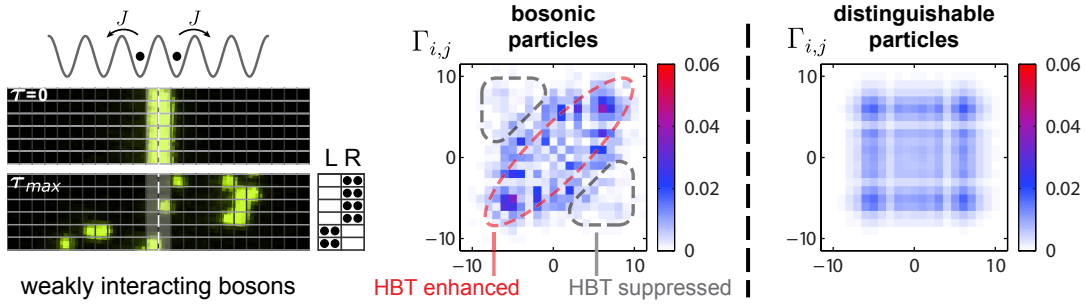
Figure 5.4: Bosonic bunching. Two bosons initialized on neighboring sites display bosonic bunching in simultaneous quantum walks, appearing close to each other with high probability. The weak interactions $u = 0.7 < 1$ do not significantly affect the dynamics. Bunching is reflected in enhanced weights near the diagonal of the experimentally observed two-particle correlator $\Gamma_{i,j}$ (middle). In comparison, the correlator expected for two distinguishable particles is featureless (right).

Bosonic particles are therefore detected in close proximity to each other much more likely than could be explained classically, and this "bosonic bunching" is a clear signature of their quantum statistics. For fermions, exchange of particles leads to an additional minus sign, resulting in opposite signs in the interference terms. Bunching is therefore suppressed, and fermions become "anti-bunched". We emphasize that there is no phase relation between the sources and it is the interference of two-particle paths rather than the interference of a single particle with itself that leads to correlations. If the two particles were both coherently delocalized over the two source sites at the beginning of the quantum walk, the two sites would have to be considered a common source for both particles and no HBT interference could be observed.

Experimentally, bosonic bunching has been observed in tunnel-coupled optical tweezers [42], expanding atomic clouds [113, 114] and photonic implementations of quantum walks [115, 116]. In our experiment, the bunching of free bosonic atoms is already apparent in single shot images of quantum walks with two particles starting from adjacent sites

in the state $a_0^\dagger a_1^\dagger |0\rangle$. For weak interactions, the two atoms are very likely to be detected close to each other because of HBT interference, as shown in raw images in Figure 5.4. We characterize the degree of bunching using the density-density correlator $\Gamma_{i,j} = \langle a_i^\dagger a_j^\dagger a_i a_j \rangle$ measured at time $\tau_{\max} \approx 2\pi \times 0.5$ for weak interactions ($u = 0.7$) (Figure 5.4, middle). Sharp features are caused by quantum interference and demonstrate the good coherence of the two-particle dynamics. Compared to the correlator expected for two distinguishable particles (computed as the outer product of the measured single-particle densities), the probability of outcomes on and near the diagonal of the correlator $\Gamma_{i,j}$ is clearly enhanced, indicating HBT interference of nearly free bosonic particles.

5.8   Fermionization

We use the sensitivity of the quantum walk to quantum statistics to probe the "fermionization" of bosonic particles caused by repulsive interactions in one-dimensional systems [58]. When such interactions are strong, double occupancies are suppressed by the large energy cost U, which takes the role of an effective Pauli exclusion principle for bosonic particles. In the limiting case of infinite, "hard-core" repulsive interactions, one-dimensional bosonic systems "fermionize". Their wavefunctions are identical to those of spinless, non-interacting fermionic systems, except for relative signs in the wavefunction that ensure the correct overall exchange symmetry of the state. Quantities that are not sensitive to relative signs in the wavefunction, such as densities and spatial correlations, are therefore the same in strongly repulsive bosonic and non-interacting fermionic systems [57]. This behavior has been observed in equilibrium in the pair-correlations and momentum distributions of large one-dimensional Bose-Einstein condensates [59, 117]. Bose-Hubbard systems below

66
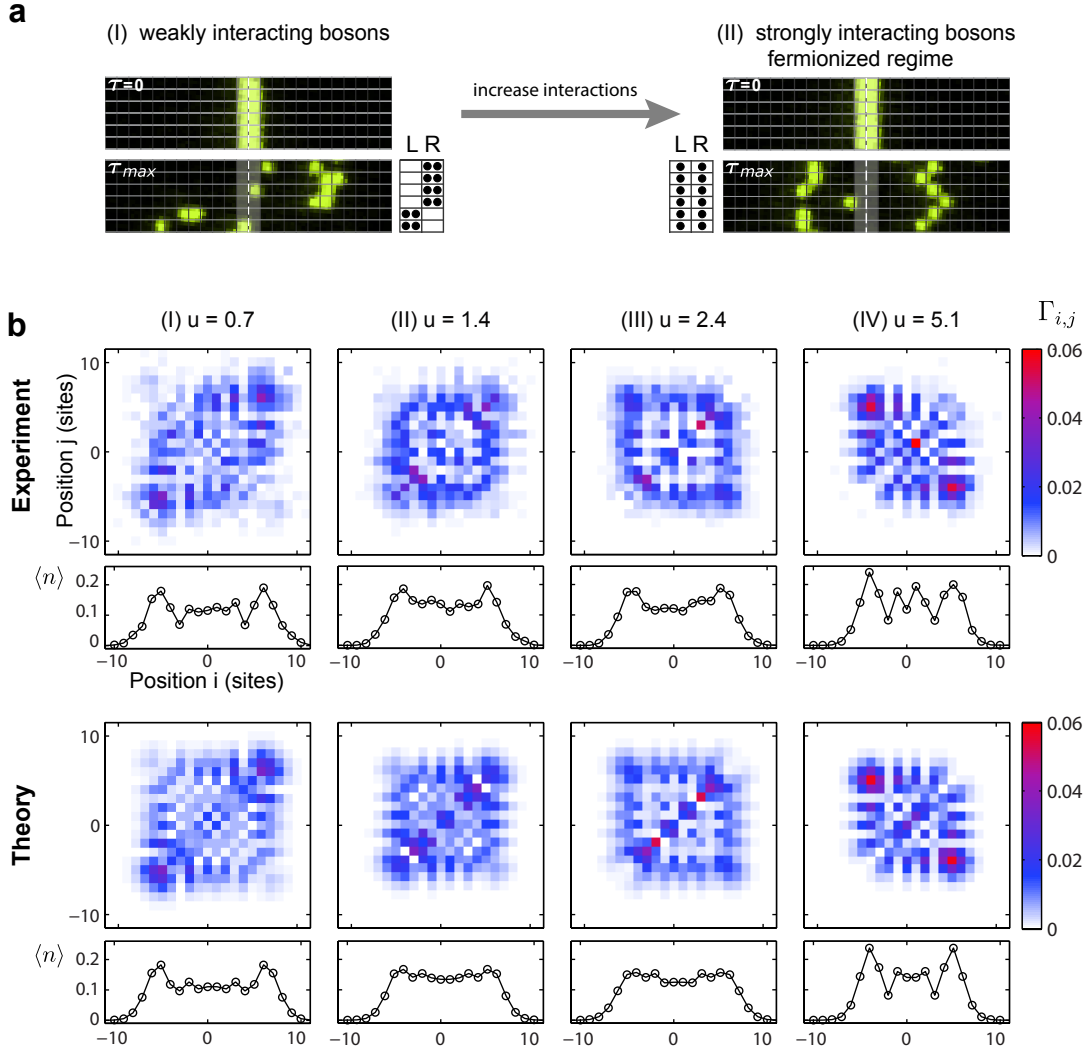
Figure 5.5: Fermionization. a) Weakly interacting bosons display strong bunching (I). Strong, repulsive on-site interactions cause bosons in one dimension to fermionize and develop long-range anti-correlations (II). (b) Measured correlator $\Gamma_{i,j}$ at time $\tau_{\max} \approx 2\pi \times 0.5$, averaged over ~ 3200 realizations. The interactions are tuned from weak ($u < 1$) to strong ($u \gg 1$) by choosing $V_x = 1\,E_r, 2.5\,E_r, 4\,E_r$, and $6.5\,E_r$.

unity filling enter the fermionized regime when $u = U/J \gg 1$.

We study the process of fermionization in the fundamental unit of two interacting particles by repeating the quantum walk from initial state $a_0^\dagger a_1^\dagger |0\rangle$ at increasing interaction strengths [95]. Figure 5.5 b shows $\Gamma_{i,j}$ for several values of u. Weakly interacting bosons ($u = 0.7$) display pronounced bunching, as shown in Figure 5.4. At intermediate values of the interaction $u = 1.4$ and $u = 2.4$, the correlation distribution is relatively uniform, as repulsive interactions compete with HBT interference. For the strongest interaction strength $u = 5.1$, most of the weight is concentrated on the anti-diagonal of $\Gamma_{i,j}$, corresponding to pronounced anti-bunching. The anti-correlations are strong enough to be visible in raw images of the quantum walk as in panel II of Figure 5.5 a, and $\Gamma_{i,j}$ is almost identical to the expected outcome for non-interacting fermions. Note that although the correlations change dramatically with increasing interaction, the densities remain largely unchanged. At all interaction strengths, the observed densities and correlations are in excellent agreement with a numerical integration of the Schrödinger equation with the Hamiltonian in equation (5.1).

Interactions in the observed two-particle scattering events take on a central role in closely related models that may be solved via the Bethe ansatz [57], where the phase shift acquired in two-particle scattering processes completely determines the microscopic and thermodynamic properties of the system.

5.9 Repulsively bound pairs

The precise control over the initial state in our system enables the study of quantum walks of two interacting bosons emerging from the same site. This initial state is not consistent with an effective Pauli blockade and cannot be described in the fermionization
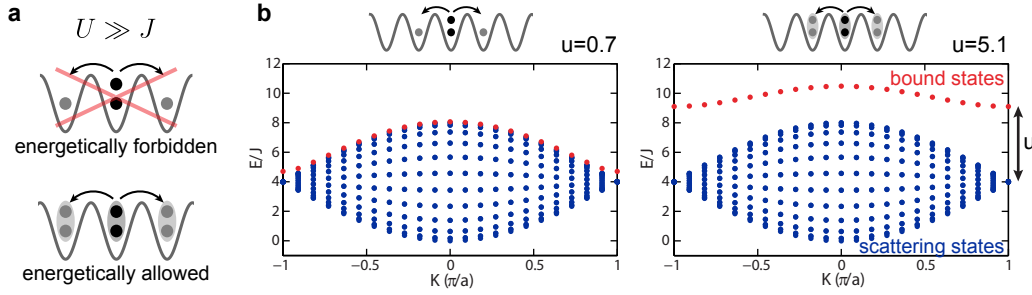
Figure 5.6: Repulsively bound paris. a) If $U \gg J$, two particles initialized on the same site correspond to a highly excited state. Separation of the particles is energetically forbidden. b) Energy spectra of an $m = 23$ site system with two particles. For $u \gg 1$, the spectrum separates into two bands. States initialized in the upper manifold of bound states cannot relax to the lower-lying scattering states, binding the two atoms together.

framework. Instead, unusual bound states caused by repulsive interactions emerge and the particles form a *repulsively bound pair* [118]. As illustrated in Figure 5.6 a, the pair of atoms corresponds to a highly excited state for repulsive interactions. If the interaction U is much larger than the tunneling energy J, the initial interaction energy cannot be converted into kinetic energy, and separation of the particles is forbidden by energy conservation. The particles propagate through the lattice as a bound state. This argument can be fleshed out by considering the eigenspectra of two particles on a finite lattice, as shown in Figure 5.6 b for $m = 23$ sites. The spectrum can be found analytically by transforming to center of mass and relative coordinates of the two particles, with the associated center of mass momentum K and relative momentum k [119]. For $u \gg 1$, the energy spectrum splits into two manifolds separated by the interaction energy U. The lower manifold corresponds to scattering states with vanishing probability of double occupancies, while the upper manifold corresponds to two-particle bound states. Two particles initialized on the same site are in a superposition of all bound states in the upper manifold. In the absence of dissi-
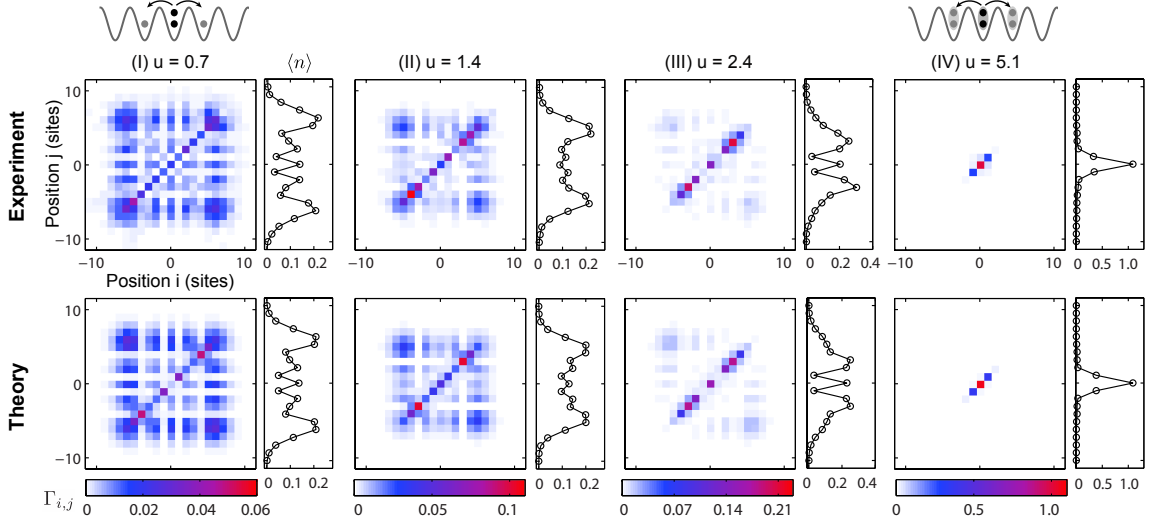
Figure 5.7: Formation of repulsively bound pairs. Two-particle correlations at $\tau_{\max} \approx 2\pi \times 0.5$ for two particles starting on site 0 in state $\frac{1}{\sqrt{2}} a_0^\dagger a_0^\dagger |0\rangle$. For weak interactions ($u = 0.7$), the atoms perform independent single-particle quantum walks. As the interaction strength is increased, repulsively bound pairs form and undergo an effective single-particle quantum walk along the diagonal of the two-particle correlator. Experimental parameters are identical to those in Figure 5.5.

pation, the two particles cannot relax to the low-lying scattering states, and the particles propagate with effective single-particle tight-binding dynamics governed by the dispersion of the bound state manifold.

Experimentally, ensembles of repulsively bound pairs have been created in optical lattices [118], and their correlated tunneling has been observed in double-wells [120] . In our quantum walk experiments, we are able to deterministically prepare individual repulsively bound pairs and systematically study their dynamics as a function of interactions.

Figure 5.7 shows the correlations and densities for two particles initialized together on site 0 in state $\frac{1}{\sqrt{2}} a_0^\dagger a_0^\dagger |0\rangle$. Because both atoms originate from the same site, HBT interference terms are not present. In the weakly interacting regime ($u = 0.7$), both particles

undergo independent free dynamics and the correlator is the direct product of the single-particle densities. As the interaction increases, separation of the individual atoms onto different lattice sites becomes suppressed, resulting in increased weights on the diagonal of the correlation matrix. For the strongest interactions, the particles are tightly bound together and the two-particle dynamics may be described as a quantum walk of the repulsively bound pair [95, 96] at a decreased tunneling rate J_{pair}. For large values of u, this pair tunneling rate reduces to the second-order tunneling [120] $J_{\text{pair}} = \frac{2J^2}{U} \ll J$, and the bound pair does not delocalize significantly on the time scale of the experiment $\tau \approx 2\pi \times 0.5$.

5.10 Correlated Bloch oscillations

The formation of repulsively bound pairs and their coherent dynamics can be observed in two-particle Bloch oscillations. We focus on the dynamics of two particles initially prepared on the same site with a gradient $\Delta \approx 0.5$ (Figure 5.8). In the weakly interacting regime ($u = 0.3$), both particles undergo symmetric Bloch oscillations as in the single-particle case, and we observe a high-quality revival after one Bloch period. When the interactions are sufficiently strong ($u = 3.5$), the pairs of atoms are tightly bound by the repulsive interaction and behave like a single composite particle. However, the effective gradient has doubled with respect to the single-particle case, and the pairs perform Bloch oscillations at twice the fundamental frequency and reduced spatial amplitude. The frequency-doubling of Bloch oscillations was predicted for electron systems [121] and cold atoms [96, 122] and has recently been simulated with photons in a waveguide array [105]. Throughout the breathing motion, the repulsively bound pairs themselves undergo coherent dynamics and delocalize without unbinding. The clean revival after half a Bloch period

71
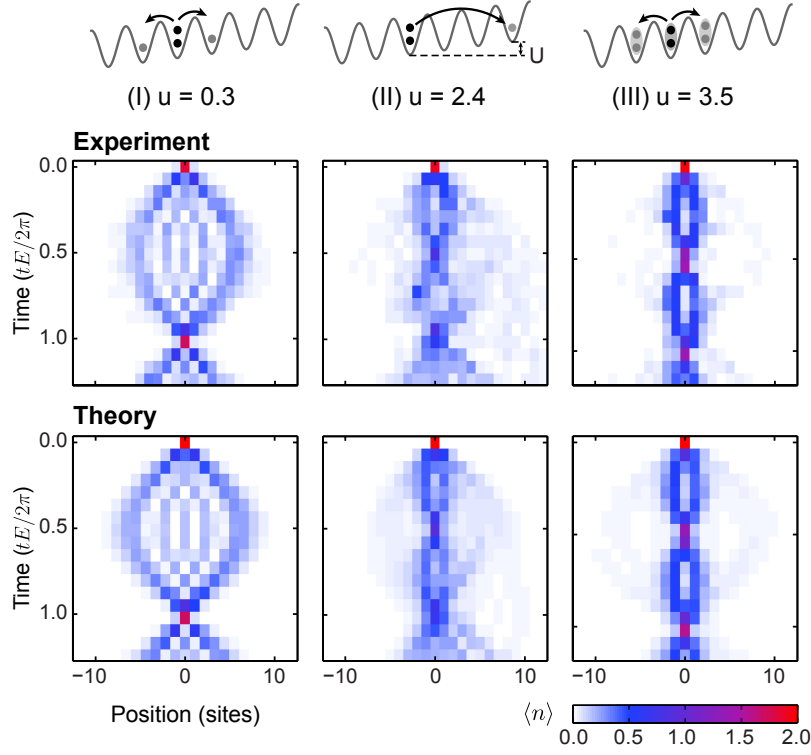
Figure 5.8: Correlated Bloch oscillations. In the weakly interacting regime (I), two particles initialized on the same site undergo clean, independent Bloch oscillations. Increasing the interaction strength (II) leads to complex dynamics involving paired and unpaired atoms. For the largest interactions (III), repulsively bound pairs perform coherent oscillations. The effective gradient for each pair is doubled with respect to the single-particle case, and the pair's oscillations occur at twice the fundamental Bloch frequency. Densities are averages over $\sim$220 independent quantum walks.

directly demonstrates the spatial entanglement of atom pairs during the oscillation.

The onset of bound pair oscillations can be seen already at intermediate interactions $u =$ 2.4. In this regime where J, U, and E are similar in magnitude, states both with and without double occupancy are energetically allowed and contribute to the dynamics. Figure 5.9 shows the density evolution separately for doublons and separated particles. Bound pairs perform oscillations near the origin, as for stronger interactions, while a significant number of pairs also separates. In such cases, interaction energy in the initial state is converted to
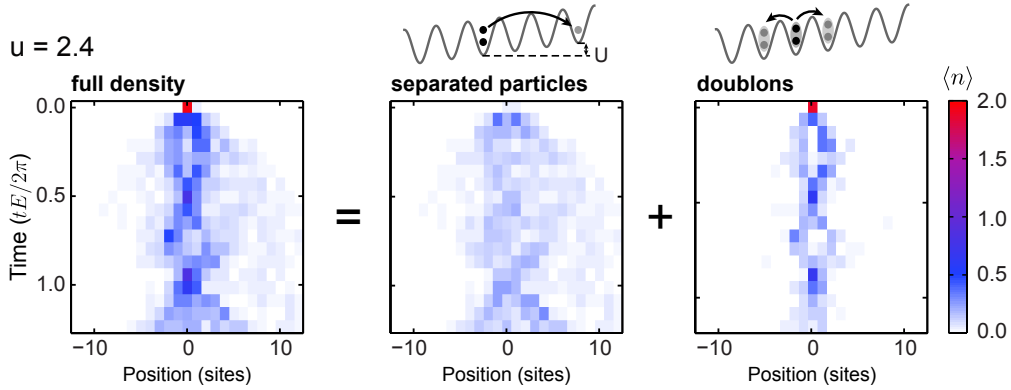
Figure 5.9: Asymmetric correlated Bloch oscillations. The dynamics shown for interme-
diate interactions $u = 2.4$ in Figure 5.8, plotted separately for outcomes with particles on
separate sites and with both particles on the same site (doublons): Atoms that remain bound
as pairs perform Bloch oscillations near the origin. If particles separate, one of the atoms
moves against the gradient, leading to an asymmetric density distribution.

potential energy, and one of the two particles tunnels resonantly against the gradient akin to

long-range tunneling [122, 123]. This process is shown schematically in Figure 5.9. There

are no resonant tunneling states on the "downhill" (left) side, and the skew to the right

against the applied force is expected and agrees with numerical simulation.

5.11 Data analysis

The experiments presented here are performed with a well-defined number of one or

two particles per horizontal tube of the optical lattice. This constraint can be used to sup-

press the effects of preparation or readout errors by post-selection of the data. For single-

particle quantum walks, we keep only outcomes with exactly one atom per one-dimensional

tube. In two-particle quantum walks, we cannot directly detect events with both particles

on the same lattice site due to parity projection in fluorescence imaging [8]. We therefore

retain outcomes with either two or zero atoms, and assume the latter always corresponds to
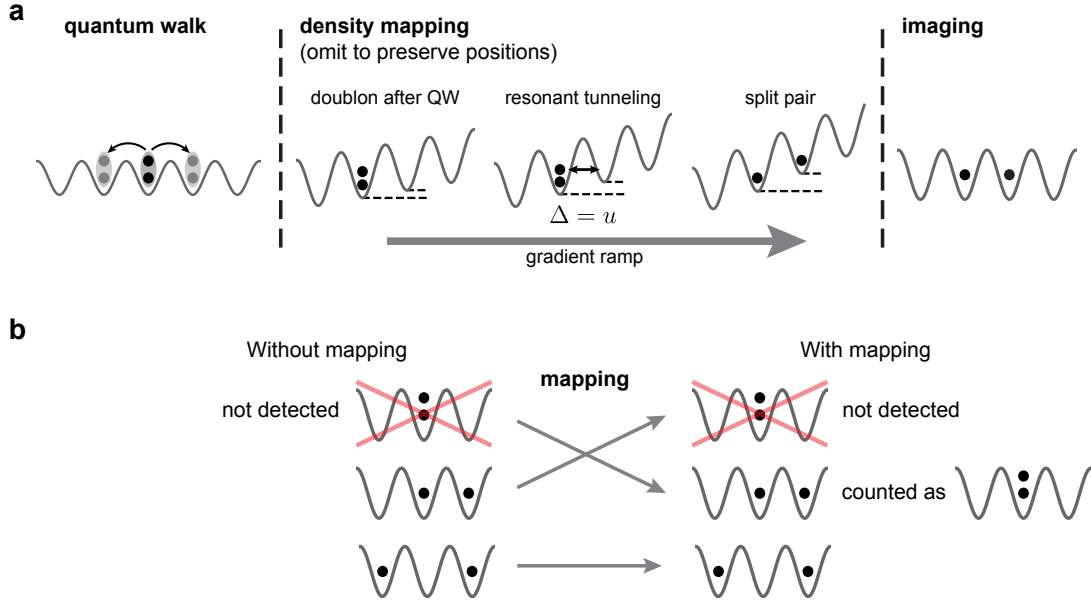
Figure 5.10: Circumventing parity projection. a) After the quantum walk in a shallow lattice, a magnetic field ramp in a deeper $V_x = 14\,E_r$ lattice splits doublons onto neighboring sites, and both atoms can be imaged. This step can be omitted to preserve the configuration after the quantum walk. b) The mapping process swaps doublons with neighboring atoms, but one set of outcomes is always lost due to parity projection. By combining data with and without the density mapping, the full correlation matrix $\Gamma_{i,j}$ can be constructed.

atom loss due to parity projection only.

To obtain the full density distribution and correlations in two-particle quantum walks, it is therefore necessary to apply a density mapping: Using a magnetic field gradient, it is possible to split pairs of particles along the direction of the quantum walk before imaging [62]: At the end of the quantum walk, the particles are pinned in a deep $V_x = 45\,E_r$ lattice. After ramping on a magnetic field gradient of $\Delta \approx 0.5u$, we reduce the x-lattice depth to $14\,E_r$, restoring a weak tunneling of $J \approx 2\pi \times 10\,\mathrm{Hz}$. The applied gradient is then swept from $\Delta \approx 0.5u$ to $\Delta \approx 2u$ in $200\,\mathrm{ms}$, before we return to the deep lattice and begin imaging. Because the gradient is larger than the tunneling at all times during the mapping

($\Delta \gg 1$), particles without neighbors remain pinned, i.e. their positions are not altered by the mapping. If, however, both particles are on the same site, one particle will tunnel uphill as the gradient is ramped through the resonance at $\Delta = u$. The particles are therefore split on two adjacent sites and can both be imaged. In data analysis, they will be counted as a doublon on the initial site. This procedure is sketched in Figure 5.10.

The mapping process is reversible, meaning that particles initially on adjacent sites after the quantum walk will be merged into a doublon. The mapping thus amounts to swapping the diagonal and first off-diagonal of the two-particle correlator prior to imaging. We therefore record all data sets with two settings, with and without the density mapping. In each realization we are blind to a particular set of outcomes, yet the full two-particle correlator can be constructed. The on-site correlation $\Gamma_{i,i}$ is obtained from the first off-diagonal elements of the histogram with the density mapping, while $\Gamma_{i,i+1}$ is determined directly from the histogram without the density mapping. To get the full correlator, we combine the two histograms weighted by the number of post-selected realizations in each half of the data set.

The aforementioned assumption in post-selection ensures the proper normalization of the histograms and is verified by comparing the far off-diagonal elements in the two weighted histograms, which are not affected by the density mapping and typically differ by less than 3%. For two particles, the density distribution $\langle n_i \rangle$ is then obtained by summing the correlator along one axis: $\langle n_i \rangle = \sum_j \Gamma_{i,j}$.

Data Set	V_x [E_r]	$J_{sp}/(2\pi)$ [Hz]	$U/(2\pi)$ [Hz]	$J_{fit}/(2\pi)$ [Hz]	$E_{fit}/(2\pi)$ [Hz]	t_{max} [ms]
Fig. 5.1	4.5	97(6)	-	107	-	6.6
Fig. 5.2	2.5	160(9)	-	166	93	14
Fig. 5.5 & 5.7 (I)	1	227(12)	161	274	-	2.1
Fig. 5.5 & 5.7 (II)	2.5	160(9)	216	168	-	3.0
Fig. 5.5 & 5.7 (III)	4	108(4)	255	109	-	5.0
Fig. 5.5 (IV)	6.5	59(3)	299	42	-	10.9
Fig. 5.7 (IV)	6.5	59(3)	299	34	-	10.9
Fig. 5.8 (I)	2.5	160(9)	53	173	97	12.8
Fig. 5.8 (II)	4	108(4)	255	101	54	22.8
Fig. 5.8 (III)	5	80(6)	279	81	34	34

Table 5.1: Bose-Hubbard parameters used for theory plots. V_x are approximate lattice depths. J_{sp} is the nearest-neighbor tunneling obtained from single-particle Bloch oscillations or directly from a band structure calculation. Typical errors on U are 3% from the uncertainty in the calibration. J_{fit} and E_{fit} are the results from fitting density distributions.

5.12 Numerical simulations

Throughout this chapter, the observed dynamics are compared to theoretical results from a direct numerical solution of the Schrödinger equation with the Hamiltonian in equation (5.1). Since the Hamiltonian is time-independent, the state at time t can obtained by matrix exponentiation of the Hamiltonian

$$|\Psi(t)\rangle = e^{iHt} |\Psi(0)\rangle \tag{5.4}$$

where $|\Psi\rangle$ and H are expressed numerically in the basis of all Fock states with the correct particle number. The calculations are performed in the Hilbert space of two particles on 23 lattice sites. The values of U and t_{max} are fixed, while J (and E in the case of Bloch oscillations) are left as free parameters to minimize the RMS error between measured and calculated densities.

We initially calibrate lattice depths using Kapitza-Dirac scattering with an uncertainty of $10\,\%$. Single-particle Bloch oscillations serve as our most sensitive probe of the tunneling J with a typical uncertainty of $5\,\%$, in agreement with a band structure calculation. The interaction U is measured at $14\,E_r$ with photon-assisted tunneling in a tilted lattice [65], and extrapolated to other lattice depths using a numerical calculation.

The minimization is performed simultaneously on data sets from Figures 5.5 and 5.7, except for panel IV. Parameter values for all data sets are listed in Table 5.1. The fitted values J_{fit} are generally in good agreement with the measurements from single-particle dynamics. At low lattice depths of $1-3\,E_r$, next-nearest-neighbor tunneling is significant, resulting in dynamics up to $20\,\%$ faster than expected from Hamiltonian (5.1). For the deep lattice at $6.5\,E_r$, residual gradients of $\sim 20\,\text{Hz/site}$ affect the dynamics, leading to a slower quantum walk than for $\Delta = 0$ and to the strong peak near the origin in panel IV of Figure 5.5 b.

5.13 Conclusions and outlook

We have demonstrated that cold atoms in optical lattices are a powerful platform for quantum walks of interacting, indistinguishable particles. The present two-particle implementation provides intuitive access to essential features of many-body systems, such as localization caused by interactions or fermionization of bosons. Going beyond the few-particle scenario, quantum walks offer an ideal starting point for the "bottom up" study of many-body quantum dynamics. The particle-by-particle assembly of interacting systems may give access to the crossover from few- to many-body physics and reveal the microscopic details of disordered quantum systems [97].

a **anyonic statistics ↔ conditional bosonic tunneling**

single particle: no phase shifts

two particles: occupation-dependent phase

b

density $\theta = 0$ $\theta = -\pi/2$ $\theta = -\pi$

Simulation

Time ($tJ/2\pi$)

Position i (sites)

$\Gamma_{\mathbf{i,j}}$

Position j (sites)

Position i (sites)
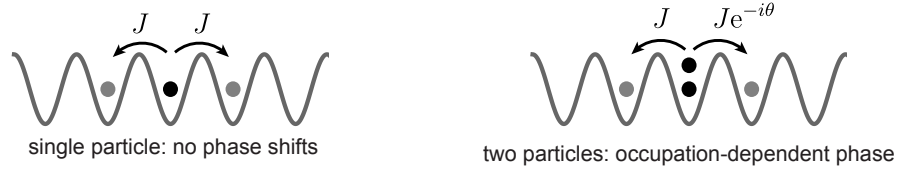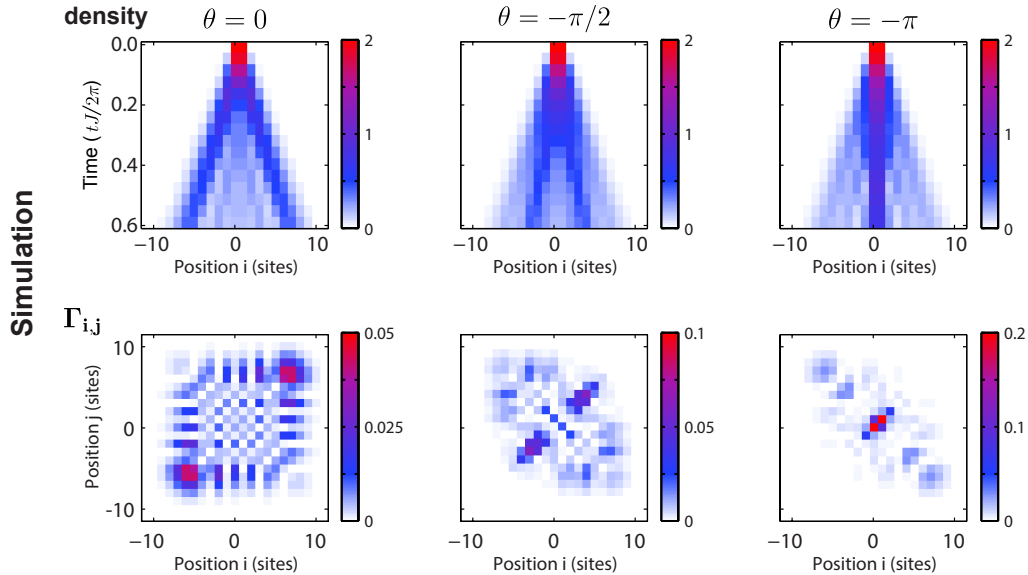
Figure 5.11: Anyonic quantum walks. a) In one dimension, anyonic quantum statistics with tunable phase angle θ can be mimicked by bosons with occupation-dependent and parity-breaking tunneling terms. b) Simulations of quantum walks of non-interacting anyons show the impact of the phase angle on the dynamics. For $\theta = 0$ (left), the particles are regular bosons. As the phase angle θ is decreased, bosonic bunching is suppressed and two-particle interference leads to a slower expansion of the density (middle). For $\theta = -\pi$, the particles obey fermionic statistics off-site, and bosonic statistics on-site. The particles do not exhibit regular fermionic anti-bunching, but remain localized near the origin.

78

An exciting possibility would be to realize quantum walks of anyonic particles [116, 124, 125]. Interpolating between bosonic and fermionic quantum statistics, anyonic particles obey quantum statistics

$$a_j a_k^\dagger - e^{-i\theta\,\mathrm{sgn}(j-k)} a_k^\dagger a_j = \delta_{jk}, \qquad a_j a_k = e^{i\theta\,\mathrm{sgn}(j-k)} a_k a_j \tag{5.5}$$

with a phase angle θ ($\theta = 0$ corresponds to bosons, $\theta = \pi$ to fermions). The sign function is defined such that $\mathrm{sgn}(0) = 0$, i.e. the particles obey on-site bosonic statistics, regardless of the phase angle θ. In one dimension, anyons can be simulated by bosons with conditional tunneling phases. This is illustrated in Figure 5.11 a: Individual anyons behave just like bosons, but in the presence of other particles, anyonic statistics are mimicked by tunneling phases that are both occupation-dependent and parity-breaking. Conditional tunneling can be engineered in a tilted optical lattice, where direct tunneling is suppressed and motion is restored through occupation-dependent tunneling via photon- or Raman-assisted tunneling [126], as already demonstrated in our experiment [65]. Figure 5.11 b shows simulations for quantum walks of two such non-interacting anyons. The realization of anyonic quantum walks, even including interactions, should be feasible in our experiment.

Chapter 6

Hong-Ou-Mandel interference of bosonic atoms in optical lattices

Portions of this chapter have appeared in:

"Measuring entanglement entropy in a quantum many-body system", R. Islam, R. Ma, P. M. Preiss, M. E. Tai, A. Lukin, M. Rispoli, and M. Greiner, *Nature* **528**, 77-83 (2015).

6.1 Introduction

One of the cornerstones of quantum optics is Hong-Ou-Mandel (HOM) interference of bosonic particles. The Hong-Ou-Mandel effect describes the interference that occurs when several indistinguishable particles delocalize over a set of modes. In such cases, many-particle paths may interfere coherently, leading to strong correlations in many-body observables. There is no classical analog for such many-particle interference, and the outcome of many experiments with indistinguishable particles is uniquely determined by the

80

a

photonic Hong-Ou-Mandel

b

atomic Hong-Ou-Mandel

$|1,1\rangle$

$(|0,2\rangle + |2,0\rangle)/\sqrt{2}$
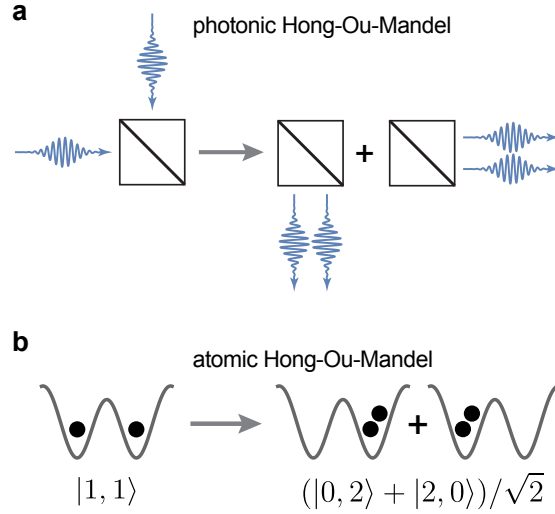
Figure 6.1: Hong-Ou-Mandel interference of bosonic particles. a) In a photonic HOM experiment, two identical photons are incident on a balanced beamsplitter. Due to the photons' bosonic statistics and interference of two-particle paths, the two photons always leave through the same exit port. b) Massive bosonic particles may undergo HOM interference in a double-well potential. Tunneling in the double-well delocalizes each atom over both sites, but due to HOM interference the two particles are always detected in the same well.

particles' quantum statistics.

The most common setting for HOM interference is shown in Figure 6.1 a: Two indistinguishable photons are incident on a balanced, non-polarizing beamsplitter. The two-particle paths leading to coincidence detection (i.e. one particle in each output port) interfere destructively and the two particles always leave the beamsplitter through the same output port. The average intensity in each output is unaffected by two-particle interference, and the correlated states with entanglement between the output modes can be detected only on the level of two-particle observables. Experimentally, this can be achieved by monitoring the probability of joint detection of a single photon in each output port, $\mathcal{P}(1,1)$ [18]. For perfect Hong-Ou-Mandel interference of non-interacting, indistinguishable bosons, $\mathcal{P}(1,1)$ is suppressed to zero.

Mathematically, the HOM interference of two photons can be described by the operator transformation performed by the beamsplitter on its inputs $i1, i2$ and outputs $o1, o2$

$$a_{i1}^{\dagger} \to (a_{o1}^{\dagger} + ia_{o2}^{\dagger})/\sqrt{2},$$
$$a_{i2}^{\dagger} \to (ia_{o1}^{\dagger} + a_{o2}^{\dagger})/\sqrt{2}. \tag{6.1}$$

Two particles incident on the inputs of this device are then transformed as

$$\begin{aligned} |1,1\rangle_i = a_{i1}^{\dagger}a_{i2}^{\dagger}|0\rangle &\to \frac{1}{2}(a_{o1}^{\dagger} + ia_{o2}^{\dagger})(ia_{o1}^{\dagger} + a_{o2}^{\dagger})|0\rangle \\ &= \frac{i}{2}(a_{o1}^{\dagger}a_{o1}^{\dagger} + a_{o2}^{\dagger}a_{o2}^{\dagger})|0\rangle \\ &= \frac{i}{\sqrt{2}}(|2,0\rangle_o + |0,2\rangle_o) \end{aligned} \tag{6.2}$$

where $|m,n\rangle_{i,o}$ labels a state with m, n photons on the input and outputs, respectively.

The complete suppression of coincidence counts is a direct experimental signature of the particles' quantum statistics. As classical noise tends to restore distinguishability to the bosonic particles, the observation of high contrast HOM interference indicates the suppression of excitations in unwanted degrees of freedom and is often used to verify the purity of quantum states, for example in the validation of single-photon sources [127]. Alternatively, the mode entanglement generated through HOM interference can be used to entangle distant qubits [128]. Recently, a fermionic version of Hong-Ou-Mandel experiments with enhanced coincidence detection was realized in the solid state [129].

6.2 Hong-Ou-Mandel interference

HOM interference is a consequence of the quantum statistics of the participating particles, and hence applies to massive bosonic atoms in optical lattices just as it does to photons.

In analogy to optical interference, two indistinguishable bosonic atoms can undergo HOM interference on a "beamsplitter" device that mixes two spatial modes. In an optical lattice, this operation can be performed through controlled tunneling in a double-well.

The double-well is governed by the Bose-Hubbard Hamiltonian

$$H_{\mathrm{DW}} = -J(a_{\mathrm{L}}^{\dagger} a_{\mathrm{R}} + a_{\mathrm{R}}^{\dagger} a_{\mathrm{L}}) + \frac{U}{2} \sum_{i=\mathrm{L,R}} n_i(n_i - 1) + \delta n_{\mathrm{R}}. \tag{6.3}$$

In the ideal non-interacting case without bias ($U = 0, \delta = 0$), the atomic "beamsplitter operation" is realized by turning on tunneling for a controlled time $\frac{2\pi}{8J}$. A particle initialized on one side of the double-well coherently delocalizes over both wells with equal amplitude (Figure 6.1 b), where a phase i is associated with each tunneling event. At the operator level, the beamsplitter operation can be described by

$$a_{\mathrm{L}}^{\dagger} \to (a_{\mathrm{L}}^{\dagger} + i a_{\mathrm{R}}^{\dagger})/\sqrt{2},$$
$$a_{\mathrm{R}}^{\dagger} \to (i a_{\mathrm{L}}^{\dagger} + a_{\mathrm{R}}^{\dagger})/\sqrt{2} \tag{6.4}$$

in exact analogy to the optical beamsplitter, where the left and right wells have take on the roles of the two output ports. Performing this beamsplitter operation with two indistinguishable bosons on the two sides of the double-well produces the superposition state $(|0, 2\rangle + |2, 0\rangle)/\sqrt{2}$, and both particles are detected in the same well. The first observations of Hong-Ou-Mandel interference of massive bosonic particles were recently made in optical tweezers [42] and momentum states of helium BECs [43].

6.3 Beamsplitter operations in double-well potentials

In our experiment, we create individual double-well potentials by combining the square optical lattice with repulsive potentials generated with the DMD, as described in chapter 4.
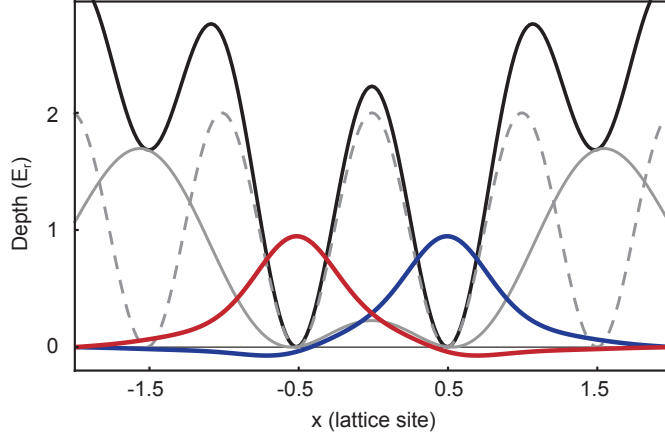
Figure 6.2: Double-well potential for the beamsplitter. The intensity profile of the projected potential (equation (6.5), gray), the lattice (gray, dashed), and the combined potential for the beamsplitter operation (black solid). Also shown are sketches of the amplitude of the ground band Wannier wavefunctions (blue, red) in each well at the beamsplitter depth.

We project a potential with a double-well profile along x and a smooth flat top profile along y:

$$
\begin{aligned}
V(x,y) &= V_{\mathrm{dw}} \left(e^{-\frac{(x-d)^2}{w_1^2}} - V_{\mathrm{rel}} e^{-\frac{x^2}{w_2^2}} + e^{-\frac{(x+d)^2}{w_1^2}} \right)^2 \\
&\times \left(\arctan\left(\frac{y+L}{s}\right) - \arctan\left(\frac{y-L}{s}\right) \right)^2
\end{aligned}
$$

(6.5)

where x and y are in units of the lattice spacing and V_{dw} is the potential depth of the projected double-well. For the Hong-Ou-Mandel experiments we use $d = 1.5, V_{\mathrm{rel}} = 0.52, w_1 = 0.95, w_2 = 0.9, L = 18$, and $s = 5.5$.

The beamsplitter operation is realized by controlled tunneling in the combined potential of the above projected potential and a shallow x-lattice, as depicted in Figure 6.2. We choose depths $V_{\mathrm{dw}} = 1.7\,E_r$ and $V_{latt} = 2\,E_r$, for which we observe a tunneling rate of $J = 2\pi \times 193(4)\,\mathrm{Hz}$ during the beamsplitter operation (Figure 6.3), in reasonable agree-
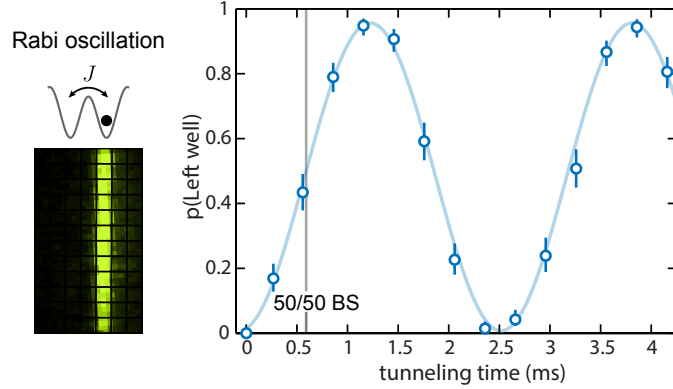
Figure 6.3: Rabi oscillations in the double-well. A single particle is initialized on the right side of the double-well and oscillates coherently between the two wells with fitted tunneling rate $J = 2\pi \times 193(4)\,\text{Hz}$ and contrast of $95(1)\,\%$.

ment with an exact diagonalization predicting $J = 2\pi \times 170\,\text{Hz}$. In the beamsplitter potential, the energy gap to the first excited band is $\sim 2\pi \times 1.3\,\text{kHz}$, and states outside the ground band do not contribute significantly to the dynamics.

6.4 Many-particle interference of massive particles

The projected potential allows the realization of an individual double-well in the optical lattice. We verify the balance between the two sides of the double-well via single-particle Rabi oscillations, as shown in Figure 6.3. A single column of atoms is initialized in a deep optical lattice with $V_x = V_y = 45\,E_r$ and the double-well is ramped on to overlap the right well with the column of atoms. V_x is then reduced to $V_{\text{latt}} = 2\,E_r$ in $500\,\mu\text{s}$ for a variable hold time, before ramping back to $V_x = 45\,E_r$ and imaging. The y-lattice remains at $45\,E_r$ throughout, and we observe decoupled Rabi oscillations in each row. In order to mitigate preparation and detection errors, we post-select outcomes with exactly one particle per row. Figure 6.3 shows resonant Rabi oscillations averaged over two adjacent rows with a fitted
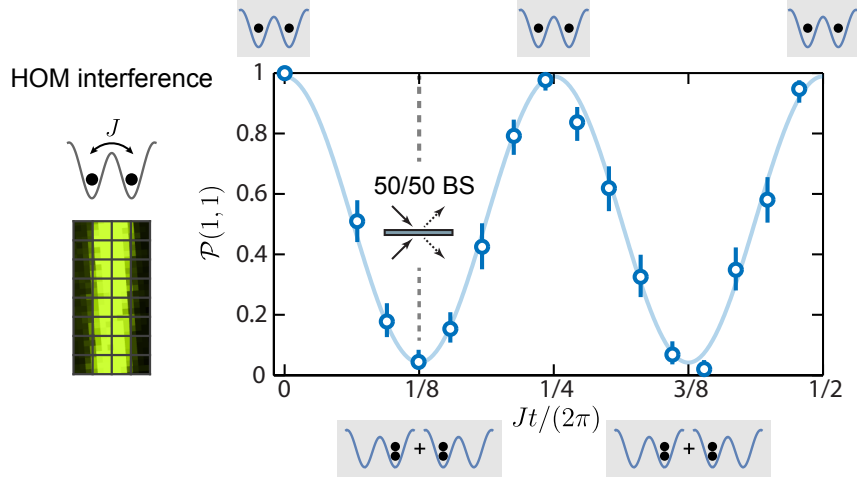
Figure 6.4: Hong-Ou-Mandel interference of bosonic atoms. Two bosonic atoms initialized on either side of the double-well interfere and the coincidence detection $\mathcal{P}(1,1)$ oscillates at $2\pi \times 772(16)\,\mathrm{Hz} \approx 4J$. At the beamsplitter times $t_{\mathrm{BS}}^{(n)}$, $\mathcal{P}(1,1)$ almost fully vanishes due to bosonic quantum statistics and takes on a residual value of $0.05(2)$.

contrast of $95(1)\,\%$.

Hong-Ou-Mandel interference of massive bosonic particles occurs when the atomic beamsplitter is initialized with one particle on each side (Figure 6.4). While the particles are tunneling in the double-well, the probability of coincidence detection $\mathcal{P}(1,1)$ oscillates at $2\pi \times 772(16)\,\mathrm{Hz} \approx 4J$ with full amplitude and is minimized for times $t = t_{\mathrm{BS}}^{(n)} = \frac{2\pi(2n-1)}{8J}$, with $n = 1, 2, \ldots$ corresponding to beamsplitter operations. As above, we post-select outcomes with even atom numbers and average dynamics over two adjacent rows. At the first realization of the beamsplitter at time $t_{\mathrm{BS}} = t_{\mathrm{BS}}^{(1)}$, we observe a residual $\mathcal{P}(1,1) = 0.05(2)$. The almost complete suppression of coincidence detections is a clear consequence of the bosonic quantum statistics and is the key to many-body interference experiments described in chapter 8.

6.5 Interference contrast

To determine the contrast of single-particle Rabi oscillations (Figure 6.3) and HOM-interference (Figure 6.4) we use Bayesian inference for the fit to the measured parity, which is more robust than a least-squares fit in situations where error probabilities are small and the visibility is close to 1. This approach prevents unphysical fits that extend past the possible bounds of the measurement and appropriately adjusts the error bars for points measured to lie near the physical bound. For each time point, we report the median and the 1σ (68 %) confidence interval of a Beta-distribution $\beta(p, m, N)$ for m successful outcomes in N experimental runs. The fitted sine curves in Figures 6.3 and 6.4 are maximum-likelihood fits to the Beta-distributions at each time point, which are determined by maximizing the product of all the Beta-distributions where the fitted curve samples them [130].

The measured Hong-Ou-Mandel interference contrast of $95(3)\,\%$ indicates a high level of control [42, 43]. Several sources might contribute to the residual $\mathcal{P}(1, 1)$ after the beamsplitter operation.

Potential imperfections   The leading order imperfection of the projected double-well potential are imperfect zero-crossings in the electric field, resulting in energy offsets between the two sides of the double-well. At the double-well depth for our beamsplitter operation, we observe offsets of $\delta \approx 2\pi \times 50\,\mathrm{Hz} \approx J/4$ or less, which do not significantly affect the HOM interference contrast (see Figure 6.5).

Alignment stability   For the balanced beamsplitter operation it is critical to avoid energy offsets between the two sides of the double-well. The projected potential is chosen such that the energy levels on either side of the double-well are first-order insensitive to
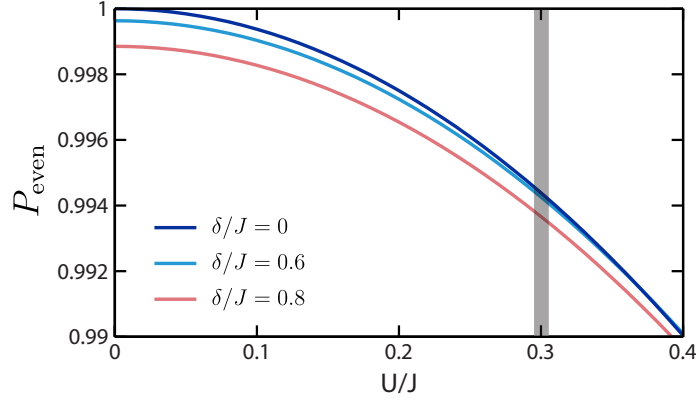
Figure 6.5: Fidelities of the beamsplitter operation. Finite interactions and energy offsets due to imperfections in the double-well potential reduce the Hong-Ou-Mandel interference contrast, as measured by the probability to detect even atom numbers at the beamsplitter time $tJ = \frac{2\pi}{8}$. For a beamsplitter operation starting with one atom on each side of the double-well and typical experimental parameters $J = 2\pi \times 200\,\mathrm{Hz}$, $U = 2\pi \times 70\,\mathrm{Hz}$, and offset $\delta = 2\pi \times 50\,\mathrm{Hz}$ (corresponding to $U/J = 0.3$ and $\delta/J = 0.25$, indicated by the gray bar), the interference contrast is expected to be reduced by $\sim 0.6\,\%$. This simulation is performed within the Bose-Hubbard model and does not take the effects of higher bands into account.

displacements between the optical lattice and the DMD-generated potential. At the chosen depths for the beamsplitter operation, a relative shift of 0.1 sites leads to an offset of $\delta \approx 2\pi \times 20\,\mathrm{Hz}$. In the experiment, we achieve a relative position stability of 0.04 sites RMS or better and fluctuations in the alignment do not create relevant offsets on the scale of $J \approx 2\pi \times 200\,\mathrm{Hz}$.

Interaction effects Interactions during the beamsplitter operation potentially reduce the HOM interference contrast. We minimize interactions by performing all experiments in a weak out-of-plane confinement of $\omega_z = 2\pi \times 800\,\mathrm{Hz}$. During the beamsplitter operation we achieve an interaction of $U = 2\pi \times 70\,\mathrm{Hz}$ (measured with photon-assisted tunneling in a deep double-well and extrapolated to lower depths), corresponding to $U/J = 0.3$. This

residual interaction reduces the HOM interference contrast by $\sim 0.6\,\%$ (see Figure 6.5).

Coherent admixture of higher bands   Interactions of two particles on the same site distort the particles' wavefunctions and coherently admix higher bands. This wavefunction is thus different from that of a single particle, restoring some distinguishability to the bosonic atoms. The dominant contribution of higher bands occurs in the z-direction, along which the confinement is weakest, and the second excited band is admixed to the wavefunction. The admixture is $\epsilon \approx (\frac{U}{2\omega_z})^2 = (\frac{2\pi \times 70\text{Hz}}{2 \times 2\pi \times 800\text{Hz}})^2 = 0.2\,\%$.

Taking into account the above considerations, the expected HOM interference contrast in the beamsplitter operation for two atoms is greater than $\sim 98\,\%$, slightly larger than the observed contrast $95(1)\,\%$.

6.6   Multi-particle Hong-Ou-Mandel interference

We have probed bosonic HOM interference for more general initial states than one boson per site [131, 132]. Figure 6.6 shows the HOM process for a double-well initialized with two particles per site. Bosonic interference results in an output state of all even combinations, and the beamsplitter transformation 6.1 predicts

$$|2,2\rangle \rightarrow \frac{\sqrt{3}}{2\sqrt{2}}(|4,0\rangle + |0,4\rangle) + \frac{1}{2}\,|2,2\rangle\,, \tag{6.6}$$

where $|n_L, n_R\rangle$ labels a state with n_L particles on the left and n_R particles on the right side of the double-well.

The presence of weak interactions $U/J \approx 0.3$ modifies the expected outcome slightly, as shown in Figure 6.6. Experimentally, we measure the number statistics of the output
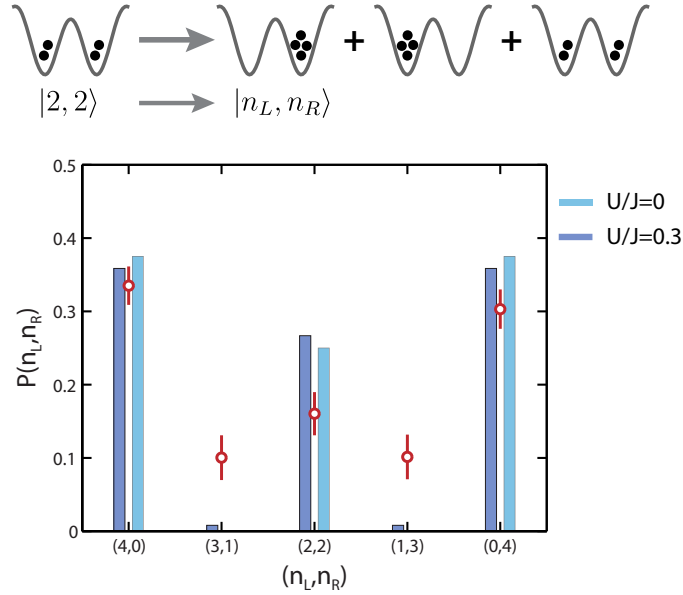
Figure 6.6: 4-particle Hong-Ou-Mandel interference. a) Initializing the double-well with two particles on each side, the beamsplitter operation is expected to produce superpositions of all combinations of even atom numbers. b) Expected (blue) and measured (red) occupations after the beamsplitter operation.

state by loading the double-well with two particles per site from an $n = 2$ Mott insulator. After the beamsplitter operation, we project a narrow "wall" potential between the two sides of the double-well before turning off the lattice and letting atoms expand in the direction of the double-well before imaging. Similarly to the full counting procedure in chapter 4, we circumvent parity projection and obtain full counting statistics for each site. The measured number statistics (red data points in Figure 6.6) display more outcomes with odd atoms numbers ($|1, 3\rangle$) than expected from the single-band Bose-Hubbard simulation. The discrepancy is potentially due to increased contributions from higher bands at the large interaction energies up to $6U \approx 2\pi \times 420\,\mathrm{Hz}$. Nevertheless, the probability of $0.80(4)$ of measuring an even number of bosons after the beamsplitter is a strong indication of 4-particle Hong-Ou-Mandel interference.

The full contrast interference of massive bosonic particles highlights the high level of control over coherent few-particle dynamics in DMD-generated potentials. We leverage this control in chapter 8 to measure the quantum mechanical purity of many-body states.

Part III

Measuring entanglement entropy

Chapter 7

Entanglement entropy

7.1 Entanglement in different physical systems

Entanglement is one of the most counterintuitive aspects of quantum mechanics, as entangled objects can be correlated more strongly than allowed by classical, local theories [19]. A maximally entangled Bell pair of spins shared between two observers, for example, is perfectly correlated in *any* measurement basis chosen by the observers [133]. The experimental observation of such correlations violating classical bounds, for example Bell or CHSH inequalities [134], rules out "hidden variable" theories and confirms quantum mechanics as a correct description of nature on a fundamental level [135].

The "spooky action at a distance" between entangled objects can also be of practical significance: Novel schemes in quantum information processing and quantum communication rely on the non-local character of shared, entangled states to perform tasks that are impossible classically. The robust generation and distribution of entangled states is one of the central goals of applied quantum science [20].

In this context, synthetic quantum systems such as cold atoms [5, 1], photonic networks [136], and some microscopic solid state devices [2] have unique advantages: their almost arbitrary control and detection of single particles, experimental access to relevant dynamical time scales, and isolation from the environment. In these systems, specific entangled states of few qubits can be created. Deterministic two-qubit gate operations, for example in trapped ion systems, can generate highly entangled states such as the Greenberger-Horne-Zeilinger (GHZ) state [24]. Stochastic methods to generate entanglement, through optical parametric downconversion [137] or projective measurements [138] are frequently used in photonic systems.

In contrast to these few-qubit states, where particles can be identified unambiguously, entanglement is more difficult to quantify in systems of delocalized particles [22]. For many itinerant indistinguishable particles, massive entanglement in the spatial degrees of freedom of all particles can emerge through the interplay of tunneling, quantum statistics and interactions. Such entanglement can be present in strongly correlated condensed matter systems or synthetic quantum matter, for example ultracold atoms in optical lattices [139]. Because indistinguishable particles, such as spinless bosons, cannot be identified by their position or other labels, entanglement between subsystems or regions, rather than individual constituents has to be considered.

7.2   Entropy of entanglement

A general way of quantifying entanglement is provided by its relation to quantum mechanical purity [19]: For a pure quantum state, entanglement between two subsystems is manifest in coherent correlations between two parts of the system. However, if an observer
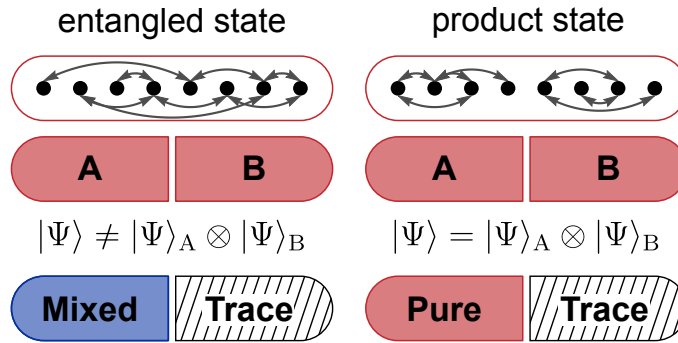
Figure 7.1: Entanglement and quantum purity. The subsystem purity for a state $|\Psi\rangle$ is inherently connected to the presence of entanglement. Subsystems A and B are entangled if quantum correlations (indicated by arrows) span their boundary (left). Tracing over subsystem B (that is, ignoring all information about B), puts subsystem A into a statistical mixture ρ_A, to a degree given by the amount of entanglement present. Non-entangled states, on the other hand, can be written as product states of subsystem states, which remain pure upon partial tracing (right). Determining the global and subsystem purity hence provides a path to measuring entanglement.

performs measurements on one of the subsystems only, while completely ignoring the state of the other, such quantum correlations appear as classical, incoherent fluctuations. A subsystem of an entangled, pure quantum mechanical state hence appears as a mixed state (Figure 7.1). This classical mixture in a density matrix ρ can be quantified by measuring the quantum purity, defined as $\mathrm{Tr}(\rho^2)$. For a pure quantum state $\mathrm{Tr}(\rho^2) = 1$, whereas for a mixed state $\mathrm{Tr}(\rho^2) < 1$. In the case of a product state, the subsystems A and B of a many-body system AB described by a wavefunction $|\psi_{AB}\rangle$ are individually pure as well, i.e. $\mathrm{Tr}(\rho_A^2) = \mathrm{Tr}(\rho_B^2) = \mathrm{Tr}(\rho_{AB}^2) = 1$ (Figure 7.1). Here the reduced density matrix of A is $\rho_A = \mathrm{Tr}_B(\rho_{AB})$, where $\rho_{AB} = |\psi_{AB}\rangle\langle\psi_{AB}|$ is the density matrix of the full system. Tr_B indicates tracing over or ignoring all information about the subsystem B. For an entangled state, the subsystems are less pure than the full system as the correlations between A and B are ignored in the reduced density matrix, $\mathrm{Tr}(\rho_A^2) = \mathrm{Tr}(\rho_B^2) < \mathrm{Tr}(\rho_{AB}^2) = 1$.

The emergence of classical mixtures due to entanglement and partial measurements leads to the concept of entropy of entanglement. This entropy associated with quantum correlations is fundamentally different from classical entropy: It can be non-extensive, such that a subsystem can carry more entropy than the full system, which may even be in a zero-entropy, pure state.

Most commonly, the entanglement entropy is quantified in terms of the von Neumann entropy for the subsystem density matrix ρ_A as

$$S_{VN} = -\mathrm{Tr}(\rho_A \ln \rho_A). \tag{7.1}$$

The very general property of entanglement entropy arising from partial measurements on entangled systems applies to an extreme variety of systems, including few-qubit systems, extended many-body states, and cosmological objects. For example, the question of what happens if part of an entangled system crosses the event horizon of a black hole and information appears to be lost entirely, has triggered significant progress in quantum gravity [28].

7.3 Entanglement entropy in many-body systems

In the context of condensed matter physics, recent theoretical developments point to entanglement entropy as a powerful means to characterize many-body states [22]. This is clear for phases for which local observables do not show unambiguous signatures of the nature of the state and a local order parameter in the Landau-Ginzburg framework cannot be defined. For example, fractional quantum Hall states [32, 31, 140] or spin liquids [141, 142] have no clear manifestation in local observables and are most appropriately characterized
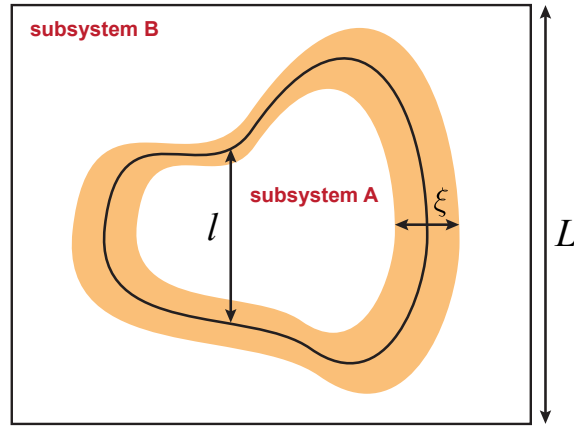
Figure 7.2: Scaling laws of entanglement entropy. Entanglement between subsystems A and B originates from correlations across the surface between the two systems, which are limited in range by the correlation length ξ. For finite correlation lengths, an area law scaling of the entanglement between A and B is expected.

by their non-local entanglement.

Entanglement entropy can also be used to identify quantum phase transitions. As opposed to diverging correlations, which are also present for classical phase transitions, entanglement entropy uniquely captures the quantum mechanical aspects of a phase transition. Its scaling near critical points is a direct signature of a system's universality class [26]. Sharp features in the entanglement between neighboring sites or the entropy of a single lattice site are predicted to occur at quantum critical points [143, 144]. Analytic and numerical results have been obtained for the behavior of entanglement entropy in many models, including Ising and Heisenberg spin systems and fermionic and bosonic lattice models (see references in [22]).

7.4 Scaling laws

Of fundamental interest in the theoretical analysis of entanglement entropy is its scaling with system size [145]. The typically considered scenario is sketched in Figure 7.2: A d-dimensional many-body system in a pure quantum state of interest is divided into two subsystems A and B, with the linear size l of the smaller subsystem large compared to the lattice constant, but small in comparison to the full system size L. An important question is then how the entanglement entropy of region A, $S(A)$, scales with the subsystem size l. The encountered scaling laws can be classified as *area laws* or *volume laws*. In a system obeying an area law, the entropy of entanglement is expected to grow as the surface area W of the boundary between subsystems, or as $S \propto l^{d-1}$ in the linear subsystem size l. Volume laws predict a scaling $S \propto l^d$.

Qualitative arguments for the origin of area laws can be made by considering for example bounded regions in spin systems [146]. Information about one subsystem from another can only be encoded on lattice sites within the correlation length ξ from the boundary, as shown in Figure 7.2. The number of sites contributing to quantum correlations across the boundary is then proportional to the shell volume $\sim \xi W$, and for a finite correlation length an area law $S \propto W \approx l^{d-1}$ should hold. The precise scaling laws for different systems in and out of equilibrium can be derived from conformal field theories. Quantitative measurements of the entanglement entropy can give access to the central charge c of the underlying conformal field theory in critical phases [147], and anyonic statistics can be inferred from the entanglement entropy in topological systems [32, 31].

Within the Bose-Hubbard model, scaling laws for entanglement entropy can be used directly to distinguish many-body phases. In the gapped Mott insulator phase, correlations

are short range and an area law strictly holds. In the atomic limit of $J = 0$, the Mott insulating state is in fact a product state and the entanglement between distinct spatial regions vanishes. For one-dimensional Bose-Hubbard systems in the gapless superfluid regime, on the other hand, the entanglement is finite. The area law, which in one dimension implies size-independent entanglement across the point contacts between A and B, is expected to be weakly violated and the entanglement entropy grows logarithmically as $S \propto \log l$ [147].The weak dependence of the entanglement entropy on subsystem size in the superfluid regime is in fact a very special property of the ground state. Generic, highly excited states of the Bose-Hubbard Hamiltonian will display a volume law, for which $S \propto l$.

For the scaling laws considered here, the subsystems are typically assumed to be simply connected and continuous. However, more interesting partitioning schemes, such as alternating subsystems can be considered to detect for example entanglement in dimerized lattices [148]. It should be noted that entanglement entropy is only meaningful when considered with respect to a particular spatial partitioning of the system. It is possible for states which are not entangled in a non-local basis (for example a BEC with all particles in the $q = 0$ momentum eigenstate) to still exhibit entanglement entropy when a particular spatial partitioning is considered.

7.5   Experimental verification of entanglement

Despite the growing importance of entanglement in theoretical physics, current condensed matter experiments do not have a direct probe to detect and measure entanglement. In synthetic few-qubit systems, entanglement can be detected by entanglement witnesses [24]: Specifically constructed observables establish a sufficient condition for

non-separability and verify the presence of entanglement. Such witness measurements are state-specific, and do not provide a meaningful scale for the amount of entanglement. For arbitrary states, an exhaustive reconstruction of the entire quantum state through tomography [149] can be used to measure entanglement. This has been accomplished in small systems of photonic qubits [150] and trapped ion spins [25], but there is no known scheme to perform tomography for systems involving itinerant delocalized particles.

In the following, we present a method to directly measure entanglement in such itinerant systems, in our case one-dimensional Bose-Hubbard chains. Our method relies on many-body interference of two identical copies of a quantum state akin to Hong-Ou-Mandel interference. Chapter 6 has introduced the experimental framework for bosonic many-particle interference in optical lattices. Chapter 8 describes direct measurements of quantum state purity and entanglement entropy via collective measurements in two-copy systems [44, 29, 30].

Chapter 8

Measuring entanglement entropy via many-body interference

Portions of this chapter have appeared in:

"Measuring entanglement entropy in a quantum many-body system", R. Islam, R. Ma, P. M. Preiss, M. E. Tai, A. Lukin, M. Rispoli, and M. Greiner, *Nature* **528**, 77-83 (2015).

In this chapter, I present quantitative measurements of entanglement in one-dimensional bosonic systems. Using DMD-generated potentials, we prepare and interfere two copies of the same many-body state, which enables us to measure quadratic functions of the density matrix [44, 29, 151, 30, 152, 137, 153]. We measure the quantum purity, Rényi entropy, and mutual information and observe the emergence of entanglement in motional degrees of freedom as a Bose-Hubbard system crosses from the Mott insulator to the superfluid regime.

8.1 Bipartite entanglement and quantum purity

The fundamental connection between entanglement entropy in an extended system and the quantum mechanical purity of its subsystems was introduced in chapter 7: Quantum correlations, or entanglement, across the boundary between two spatially distinct regions A and B lead to a reduction of the quantum mechanical purity of the subsystems. For a globally pure entangled state ($\mathrm{Tr}(\rho_{AB}^2) = 1$), partial measurements on one subsystem result in mixed states in the subsystems with density matrices $\rho_{A/B}$. Even if the many-body state is mixed ($\mathrm{Tr}(\rho_{AB}^2) < 1$), it is still possible to measure entanglement between the subsystems [19]. To prove this entanglement, it is sufficient [154] to show that the subsystems are less pure than the full system, i.e.

$$\mathrm{Tr}(\rho_A^2) < \mathrm{Tr}(\rho_{AB}^2),$$

$$\mathrm{Tr}(\rho_B^2) < \mathrm{Tr}(\rho_{AB}^2). \tag{8.1}$$

These inequalities provide a tool for detecting entanglement in the presence of experimental imperfections. Furthermore, quantitative bounds on the entanglement present in a mixed many-body state can be obtained from these state purities [155].

Equation (8.1) can be framed in terms of entropic quantities [19, 154]. A useful and well-studied quantity is the n-th order Rényi entropy,

$$S_n(A) = \frac{1}{1-n} \ln \mathrm{Tr}(\rho_A^n). \tag{8.2}$$

The second-order ($n = 2$) Rényi entropy and purity are related by $S_2(A) = -\ln \mathrm{Tr}(\rho_A^2)$. The subsystem Rényi entropy $S_2(A)$ provides a lower bound for the von Neumann entanglement entropy $S_{VN}(A) = S_1(A) = -\mathrm{Tr}(\rho_A \ln \rho_A)$ extensively studied theoretically. Note that we use logarithms to base e throughout.

The Rényi entropies play an important role in theoretical condensed matter physics, as they can be used to extract information about the "entanglement spectrum" [156], which can provide more information about the quantum state than just the von Neumann entropy. In terms of the second-order Rényi entropy, the sufficient conditions to demonstrate entanglement [154, 19] become $S_2(A) > S_2(AB)$, and $S_2(B) > S_2(AB)$, i.e. the subsystems have more entropy than the full system. These entropic inequalities are more powerful in detecting certain entangled states than other inequalities like the Clauser-Horne-Shimony-Holt (CHSH) inequality [152, 154].

8.2   Probing indistinguishability by interference

In order to experimentally detect Rényi entropies, it is necessary to measure polynomial functions of the density matrix, such as the purity $\mathrm{Tr}\rho^2$, for a many-body system and its subsystems. Probing such quantities, which depend on populations and coherences of the density matrix, is challenging in many-body systems with large-dimensional Hilbert spaces. For simple single- or two-particle Fock states, Hong-Ou-Mandel interference was introduced in chapter 6 as a metric for quantum purity. To see how such an interferometric measurement of indistinguishability might be extended to more interesting many-body states, consider the situation shown in Figure 8.1: A quantum system consisting of two segments, here two potential wells with a single spatial mode each, is prepared with the same arbitrary bosonic quantum state $|\Psi\rangle$ in each copy.

A useful basis to describe the two-copy state $|\theta\rangle = |\Psi\rangle \otimes |\Psi\rangle$ in terms of the bosonic
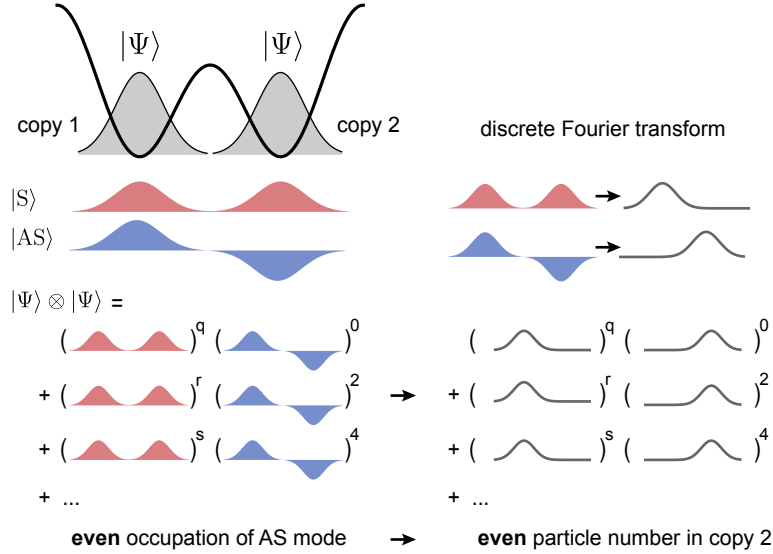
Figure 8.1: Measuring indistinguishability of many-body states. The combined state $|\theta\rangle = |\Psi\rangle \otimes |\Psi\rangle$ of a two-copy system prepared with the same many-particle quantum state $|\Psi\rangle$ in each copy can be expressed in the basis of symmetric $|\mathrm{S}\rangle$ and antisymmetric $|\mathrm{AS}\rangle$ states. Because the global state $|\theta\rangle$ must be invariant under the transformation $a_1^\dagger \leftrightarrow a_2^\dagger$, only states with *even occupation of the state* $|\mathrm{AS}\rangle$ are populated. A discrete Fourier transform maps $|\theta\rangle$ to a state with only *even particle numbers in copy* 2. The occupation $q, r, s \ldots$ of the symmetric mode is not constrained.

creation operators $a_i^\dagger$ acting on copy i are the symmetric and antisymmetric combinations

$$|\mathrm{S}\rangle = (a_1^\dagger + a_2^\dagger)/\sqrt{2},$$

$$|\mathrm{AS}\rangle = (a_1^\dagger - a_2^\dagger)/\sqrt{2}. \tag{8.3}$$

The full two-copy state can then be expressed in terms of the states

$$(1/\sqrt{2})^{c+l}(a_1^\dagger + a_2^\dagger)^c(a_1^\dagger - a_2^\dagger)^l|0\rangle \tag{8.4}$$

with l particles in the antisymmetric mode and c particles in the symmetric mode.

Since the full system contains the same bosonic state $|\Psi\rangle$ in each copy, it is invariant under a swap of states between the copies, that is under the transformation $a_1^\dagger \leftrightarrow a_2^\dagger$. The

104

two-copy state hence only populates the subset of states for which l, the number of particles in the antisymmetric mode, is even.

This restriction to the symmetric subspace can be measured by interfering the two copies of $|\Psi\rangle$, as described by a discrete Fourier transform (DFT)

$$(a_1^\dagger + a_2^\dagger)/\sqrt{2} \to a_1^\dagger,$$

$$(a_1^\dagger - a_2^\dagger)/\sqrt{2} \to a_2^\dagger. \tag{8.5}$$

Under this operation, the modes $|S\rangle$ and $|AS\rangle$ are mapped to copy 1 and 2, respectively

$$(1/\sqrt{2})^{c+l}(a_1^\dagger + a_2^\dagger)^c(a_1^\dagger - a_2^\dagger)^l|0\rangle \to (a_1^\dagger)^c(a_2^\dagger)^l|0\rangle, \tag{8.6}$$

and the particle number in well 2 after the interference step reveals the initial occupation of the antisymmetric mode (Figure 8.1).

Performing a DFT between two quantum states provides a general framework to verify the indistinguishability of quantum states: If the two copies of the quantum system are prepared in the same pure quantum state, the detected particle number in copy 2 after the DFT is always even. On the other hand, if the initial quantum states are not perfectly pure or perfectly identical, states with odd particle number in copy 2 after the DFT will be populated. Comparing the relative occurrence of odd and even particle numbers in copy 2 hence quantifies the indistinguishability of the initial quantum states.

This scheme applies to any bosonic state. In particular, if the two copies are prepared in coherent states $|\alpha\rangle$ with fluctuating particle numbers but well-defined, identical phases, the occupation of the antisymmetric mode is zero, and no particles are detected in copy 2. If the coherent states become squeezed, pairs of particles will appear in copy 2, but no odd occupation numbers are possible as long as the initial states remain identical. For

initial Fock states of individual particles, the DFT corresponds to the Hong-Ou-Mandel interference of bosons discussed in chapter 6.

8.3 Measuring purity

A quantitative description of many-body Hong-Ou-Mandel interference can be given in terms of the `swap` operator, which exchanges any two quantum states between two copies:

$$V_2(|\Psi_1\rangle \otimes |\Psi_2\rangle) = |\Psi_2\rangle \otimes |\Psi_1\rangle, \tag{8.7}$$

where $|\phi\rangle \otimes |\chi\rangle$ denotes a system with state $|\phi\rangle$ in copy 1 and $|\chi\rangle$ in copy 2.

Two successive applications of the `swap` operator leave the system unchanged, $V_2^2 = \mathbb{1}$. Therefore V_2 has eigenvalues ± 1, corresponding to subspaces of the 2-copy system that are symmetric or antisymmetric with respect to the state exchange between the systems. It can be shown that $\mathrm{Tr}(\rho_1 \rho_2) = \mathrm{Tr}(V_2(\rho_1 \otimes \rho_2))$, that is the expectation value of the `swap` operator measures the quantum state overlap between the two copies (see appendix A). Now if the states in the two copies are the same, $\rho_1 = \rho_2$, then $\mathrm{Tr}(\rho^2) = \mathrm{Tr}(V_2(\rho \otimes \rho))$, i.e. the purity of a *single* system is equal to the expectation value of V_2 *in the two-copy system* [44, 30].

As shown previously, the discrete Fourier transform (8.5) maps the antisymmetric and symmetric subspaces of V_2 to states with odd and even atom numbers in copy 2 [30]. Assigning a parity P_i, equal to ± 1 for an even or odd number of particles in copy i after the DFT, the expectation value of V_2 can be evaluated and the purity of the initial states ρ is given by

$$\mathrm{Tr}(\rho^2) = \mathrm{Tr}(V_2(\rho \otimes \rho)) = \langle P_2 \rangle. \tag{8.8}$$
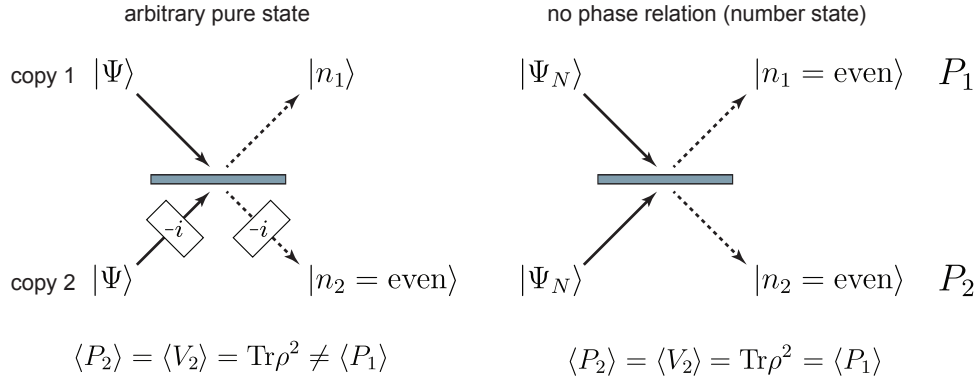
Figure 8.2: Beamsplitter for many-body interference. Left: With the beamsplitter opera-
tion and proper phase shift operations, the discrete Fourier transform probes quantum state
overlap and quantum purity by measuring the average parity in output port 2 of the beam-
splitter. For pure identical incident states, the atom number is always even in output 2.
Right: For states with well-defined particle number N, no macroscopic phase relationship
exists between the input states, and the phase shifts in the input/output ports have no phys-
ical significance. Both outputs are equivalent and may be used to measure the expectation
value $\langle V_2 \rangle$ of the `swap` operator.

The complex task of measuring quadratic functions of a density matrix ρ is thus reduced
to the problem of counting particles after a discrete Fourier transform between two copies
of ρ.

The particular role of copy 2 is a consequence of the phases chosen in the discrete
Fourier transform (8.5), which is realized by a beamsplitter operation and phase shifts in
copy 2 (Figure 8.2). The phase shifts ensure the destructive interference of states with
well-defined phase in output port 2 of the beamsplitter. In the case that there is no defined
phase relationship between the initial states in each copy, such as for Fock states, phase
shifts can be omitted and the DFT is replaced by the beamsplitter operation introduced in
chapter 6 (see appendix A). The two copies are then equivalent, and the interference of
indistinguishable states results in even atom numbers in both copies ($\langle P_1 \rangle = \langle P_2 \rangle = \langle P \rangle$).
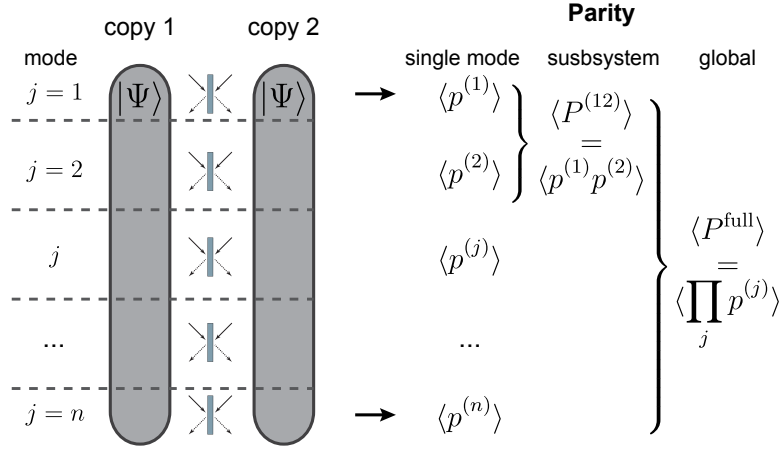
Figure 8.3: Mulitmode bosonic interference. Two copies of the quantum state $|\Psi\rangle$ interfere by simultaneous application of the beamsplitter transformation to all n modes. The parity $\langle p^{(j)} \rangle$ probes the purity of the density matrix ρ_j describing the state in each mode j. The full system and subsystem purity can be obtained from the appropriate product of parities over individual modes $\prod_j p^{(j)}$.

We assume this experimentally relevant case from here on.

8.4   Multimode interference

So far we have described the measurement of quantum purity of states restricted to a single spatial mode. In order to measure entanglement in itinerant systems, it is necessary to evaluate full system and subsystem purity for states with many spatial degrees of freedom.

The comparison of many-body quantum states by interference can be extended from the single- to the multimode case (Figure 8.3). Each initial state $|\Psi\rangle$ then extends over several modes j, such as different spin states or lattice sites. In order to measure quantum purity of the full state $|\Psi\rangle$ and its subsystems, the beamsplitter operation is applied to all modes simultaneously.

The beamsplitter transformation now measures the parity of each mode $\langle p^{(j)} \rangle$, giving

the purity of the single mode density matrix ρ_j via equation (8.8).

For a subsystem comprised of a set of modes, the purity is given by the product over mode parities $\langle P \rangle = \left\langle \prod_j p^{(j)} \right\rangle = \mathrm{Tr}(\rho_{\mathrm{sub}}^2)$. Arbitrary subsystem sizes and geometries, including non-contiguous subsystems, can be probed by extracting the appropriate product of single-mode parities. The full system purity is given by the product over all modes [29, 30]. In particular, if the two copies are prepared in the same global quantum state, the two-copy state is symmetric under the simultaneous transformation $a_{1,j}^\dagger \leftrightarrow a_{2,j}^\dagger$ for all modes j. The parity of the full system is 1 and the summed occupations in each copy after the beamsplitter are always even.

Several theoretical works have proposed to quantify entanglement via Hong-Ou-Mandel interference [30, 44, 29, 152]. An experiment can be devised as follows: Two copies of a bosonic many-body state are prepared and interfered. The resulting HOM interference contrast, that is the extent to which the outcomes are comprised of even atom numbers, is a direct measure of the purity of the quantum mechanical states on the inputs. In product states, for which the beamsplitter network receives pure quantum states in each mode, full HOM interference contrast is observed for each mode or set of modes. In entangled states, interference contrast is reduced for each entangled mode individually. The product of beamsplitter outcomes over all modes, however, still displays full HOM interference contrast as the full quantum state is pure. The unique signature of an entangled state is full contrast HOM interference of the system on a global scale, while the local interference contrast for each subsystem, or subset of modes, is reduced. This situation requires the outcomes of beamsplitter operations on different subsystems to be correlated, which precisely probes the entanglement between subsystems.

8.5 Collective measurements

The necessity of performing measurements on two copies of a quantum state in order to quantify entanglement can be understood from considering the notion of entanglement hierarchies. As there is no direct observable associated with entanglement, the quantification of the "amount" of entanglement in a system can seem ambiguous at first. A widely accepted measure of the degree of entanglement is provided by the concept of invariance under local operations and classical communication (LOCC): The entanglement between two subsystems of a pure state, which are shared between two observers, cannot increase under local operations (LO), including measurements, applied to each subsystem independently, or by classical communication (CC) between the observers [157]. Under such conditions, it is possible to obtain a "less entangled" state from a "more entangled" state, but not vice-versa, and a hierarchy of entanglement is established [158]. The impossibility for an observer to create entanglement under LOCC underlies the need to generate and share entanglement between observers in quantum communication protocols.

Conversely, the requirement that entanglement cannot increase under LOCC severely restricts the possibilities of measuring entanglement: Any observable chosen to quantify entanglement in a subsystem has to be invariant under all reversible, local operations [159]. For a single quantum-mechanical system, there is no such observable and full state tomography is the only means to quantify entanglement.

A resolution is offered by *collective measurements* on n-fold copies of the same quantum mechanical state [159]. For n copies of a quantum state, it is possible to construct non-trivial observables that are invariant under local operations applied to each copy independently, yet measure the amount of entanglement in the subsystem [30, 160]. In the

case of $n = 2$, the `swap` operator provides an appropriate observable. This operator commutes with any unitary that acts on part of each copy identically, and its expectation value provides an entanglement measure that respects invariance under LOCC.

The concept of collective measurements can readily be extended to $n > 2$ copies, for which n-th order polynomial functions of ρ and hence higher-order Rényi entropies can be measured.

8.6   Experimental implementation

We probe entanglement in small one-dimensional bosonic systems governed by the Bose-Hubbard Hamiltonian with tunneling J and on-site interaction U. To initialize two independent and identical copies of a state with fixed particle number N, we start with a low-entropy, two-dimensional Mott insulator with unity filling in the atomic limit [55] and deterministically retain a plaquette of $2 \times N$ atoms while removing all others (see chapter 4). This is illustrated in Figure 8.4 a. The plaquette of $2 \times N$ atoms contains two copies (along the y-direction) of an N-atom one-dimensional system (along the x-direction), with $N = 4$ in this figure. The desired quantum state is prepared by manipulating the depth of the optical lattice along x, varying the parameter U/J_x where J_x is the tunneling rate along x. A box potential created by the DMD is superimposed onto this optical lattice to constrain the dynamics to the sites within each copy. During the state preparation, a deep lattice barrier separates the two copies and makes them independent of each other. We rapidly freeze the tunneling along x without destroying the coherence in the many-body state and apply the beamsplitter along y. Finally, we rapidly turn on a very deep 2D lattice to suppress all tunneling and detect the number parity (even $= 1$, odd $= -1$) at each site.
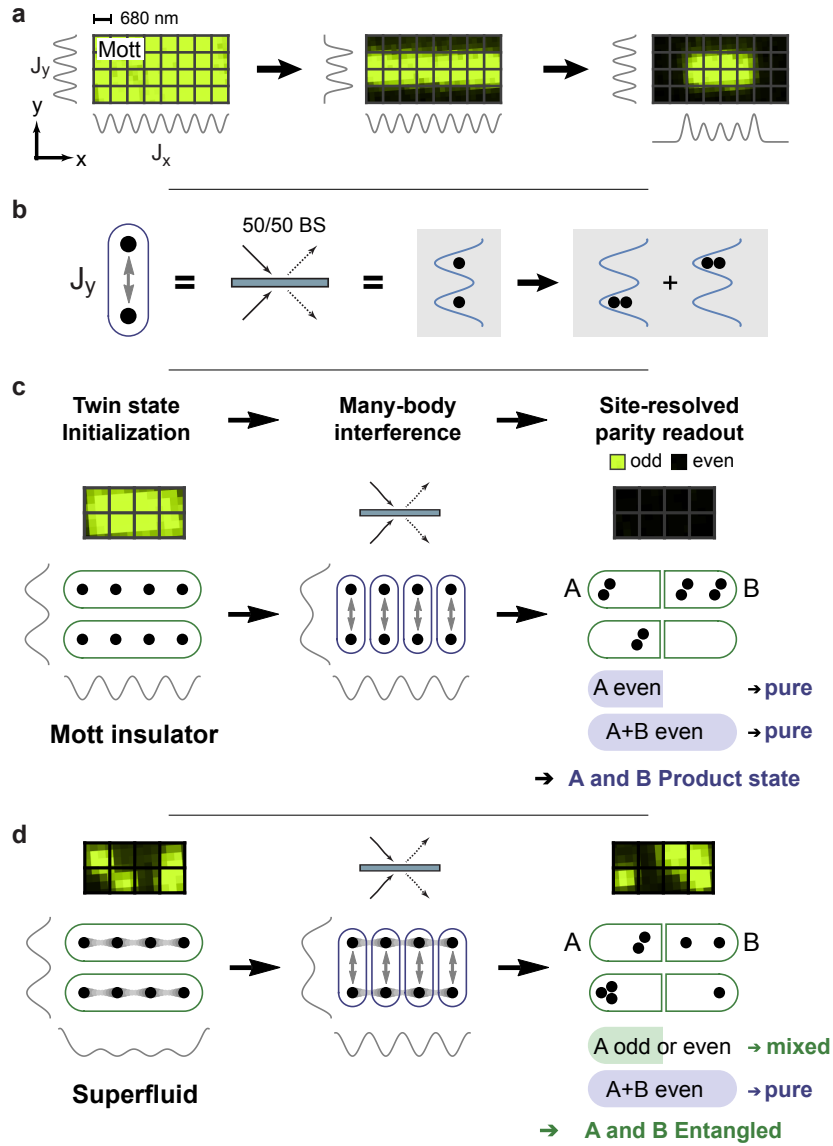
Figure 8.4: Many-body interference to probe entanglement in optical lattices. a) We initialize a 2×4 plaquette by sequential cutting procedures with DMD-generated potentials. b) The centerpiece of many-body interference is the beamsplitter operation, realized in a double-well potential in the y-direction. In the Mott insulating state, the beamsplitter operation creates a two-particle superposition state via HOM interference. c) When two copies of a product state, such as the Mott insulator are interfered, the output states contain even particle number globally (full system) as well as locally (subsystem), indicating pure states in both. d) For two copies of an entangled state, such as a superfluid state, the output states contain even particle number globally (pure state) but a mixture of odd and even outcomes locally (mixed state). This directly demonstrates entanglement.

112

The beamsplitter operation is here applied on all N sites of the system simultaneously. We can therefore determine the purity of all possible subsystems in a single data set by using different partitioning schemes in analysis. We construct the parity of a spatial region by multiplying the parities of all the sites within that region. The average parity over repeated realizations measures the quantum purity, both globally and locally according to equation (8.8), enabling us to determine the second-order Rényi entropy globally and for every subsystem.

The beamsplitter operation required for the many-body interference is realized in a double-well potential along y, as described in detail in chapter 6 (Figure 8.4 b). The fidelity of the beamsplitter operation is characterized by the suppression of coincidence detection $\mathcal{P}(1,1)$ to $0.05(2)$ for an initial state of one boson per site. The results from this interference can be interpreted as a measurement of the quantum purity of the initial Fock state as measured from the average parity (equation (8.8)), $\langle P \rangle = 1 - 2 \times \mathcal{P}(1,1) = 0.90(4)$. The imperfections in the beamsplitter operation currently limit the system size in our experiments to 2×4.

Note that for the experimental measurement of the state overlap $\text{Tr}(\rho_1 \rho_2)$ to be meaningful, we have to ensure that the different states ρ_1 and ρ_2 do not evolve between the state preparation and the beamsplitter operation, while we ramp to a deep square lattice and into the double-well potential. It can be shown (see appendix A) that time evolution which preserves particle configurations, but includes phase accumulation due to gradients or interactions (as expected for evolution in a deep lattice) does not affect the measured values of $\text{Tr}(\rho_1 \rho_2)$, as long as the evolution is *the same in both copies*. Differential gradients of only a few Hz/site along x, for example, can lead to complete loss of the overlap

$\text{Tr}(\rho_1\rho_2)$ over tens of milliseconds. We therefore keep the time in the deep lattice as short as possible, $\sim 4\,\text{ms}$. Experimentally, we measure full system purities close to the maximum expected for the measured beamsplitter fidelity, indicating that no significant differential evolution takes place between state preparation and the interference, and that many-body coherence is preserved.

8.7 Entanglement in the ground state

The Bose-Hubbard model provides an interesting system to investigate entanglement. In optical lattice systems, a lower bound of the spatial entanglement has been previously estimated from time-of-flight measurements [161] and entanglement dynamics in spin degrees of freedom has been investigated with partial state reconstruction [90]. Here, we directly measure entanglement in spatial degrees of freedom in a site-resolved way. In the strongly interacting, atomic limit of $U/J_x \gg 1$, the ground state is a Mott insulator corresponding to a Fock state of one atom at each lattice site. The quantum state has no spatial entanglement with respect to any partitioning in this phase – it is in a product state of the Fock states. As the interaction strength is reduced adiabatically, atoms begin to tunnel across the lattice sites, and ultimately the Mott insulator melts into a superfluid with a fixed atom number. The delocalization of atoms creates entanglement between spatial subsystems. This entanglement originates [162, 163] from correlated fluctuations in the number of particles between the subsystems due to the super-selection rule that the total particle number in the full system is fixed, as well as coherence between various configurations without any such fluctuation.

To probe the emergence of entanglement, we first prepare the ground state of the Bose-

Mott insulator   adiabatic melt   superfluid

mixed

Renyi Entropy S_2

Purity = $\langle P \rangle$

U/J_x

pure
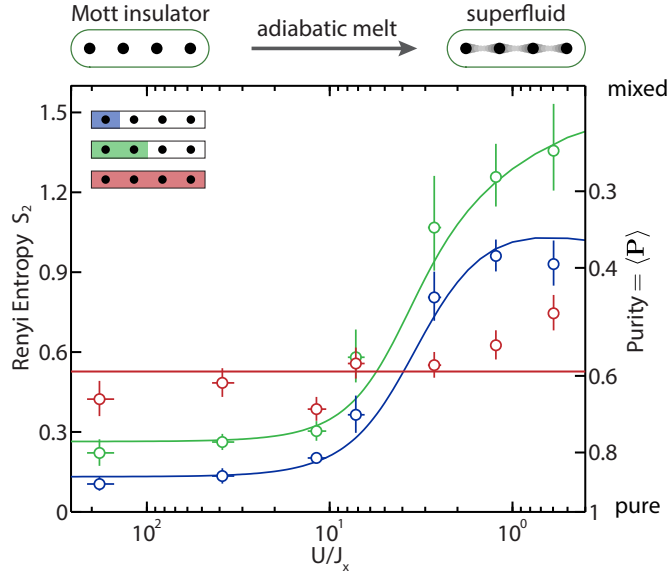
Figure 8.5: Entanglement in the ground state of the 4-site Bose-Hubbard model. As the interaction strength U/J_x is adiabatically reduced, the Rényi entropy $S_2(A)$ of subsystem A (green and blue) becomes larger than that of the full system (red). This non-extensive entropy demonstrates entanglement in the superfluid phase, generated by coherent tunneling of bosons across lattice sites. In the Mott insulator phase ($U/J_x \gg 1$) the full system has more Rényi entropy than the subsystems due to classical entropy. The circles are data and the solid lines are theory calculated from exact diagonalization with an offset to account for classical entropy. The vertical error bars in all figures indicate 1 σ in combined statistical and systematic errors (see appendix A). Horizontal error bars correspond to a typical uncertainty in the lattice depth of $\pm 2\,\%$.

Hubbard model in both copies by controlling the optical lattice depth along x. In the atomic Mott limit (Figure 8.4 c), the state is separable. Hence, the interference signal between two copies should show even parity in all subsystems, indicating a pure state with zero entanglement entropy. Towards the superfluid regime (Figure 8.4 d), the buildup of entanglement leads to mixed states in subsystems, corresponding to a finite entanglement entropy. Hence, the measurement outcomes do not have a pre-determined parity. Remarkably, the outcomes should still retain even global parity, indicating a pure global state. Higher entropy in the

subsystems than the global system cannot be explained classically and demonstrates bipartite entanglement.

Experimentally, we find exactly this behavior for our two 4-site Bose-Hubbard systems (Figure 8.5). We observe the emergence of spatial entanglement as the initial atomic Mott insulator melts into a superfluid. The measured quantum purity of the full system is ~ 0.6 across the Mott to superfluid crossover, corresponding to a Rényi entropy, $S_2(AB) \approx 0.5$. The measured purity deep in the superfluid phase is slightly reduced, likely due to the reduced beamsplitter fidelity in presence of increased single site occupation number, heating, and residual differential gradients between the two copies. The nearly constant global purity indicates high level of quantum coherence during the crossover. For lower interaction strength U/J_x (superfluid regime) we observe that the subsystem Rényi entropy is higher than the full system, $S_2(A) > S_2(AB)$. This demonstrates the presence of spatial entanglement in the superfluid state. In the Mott insulator regime ($U/J_x \gg 1$), $S_2(A)$ is lower than $S_2(AB)$ and proportional to the subsystem size, consistent with a product state that has only classical entropy.

The dominant source of errors in these experiments are single-particle loss processes during state preparation, the experimental sequence, and in the detection process. We suppress the associated noise by post-selecting outcomes of the experiment for which the total number of atoms detected in both copies is even. This constitutes about $60\,\%$ of all the data (see appendix A). The reduced full system purity of ~ 0.6 is likely limited by measurement errors due to the finite $95(3)\,\%$ fidelity of the beamsplitter operation on each site. For a Mott insulating product state, the expected full system purity is given by the product of individual parities, $\langle P \rangle = \prod_j \langle p^{(j)} \rangle = 0.90^4 \approx 0.66$, in good agreement with the exper-

imentally measured purity in Figure 8.5. The consistency of the measured purity with an imperfect beamsplitter operation alone suggests a significantly higher purity for the actual many-body state. The measured full system entropy is a sum of entanglement entropy and extensive classical entropy caused by beamsplitter imperfections.

The observed subsystem entropies agree very well with the theoretical predictions from an exact diagonalization (solid lines in Figure 8.5). The only free parameter is a vertical offset corresponding to the classical extensive entropy caused by beamsplitter imperfections. We obtain this offset from the average measured full system entropy and scale to the appropriate subsystem size.

8.8   Multipartite entanglement

Our site-resolved measurement simultaneously provides information about all possible spatial partitionings of the system. It is hence possible to study interesting partitionings beyond the case of bi-partite continuous subsystems shown in Figure 8.5.

The left panel of Figure 8.6 shows the entanglement entropy of all possible splittings in the 4-site system, including non-continuous subsystems of the form ABAB. Data points for subsystems are connected by lines, where line color indicates subsystem size, and red circles show the full system entropy across the superfluid-Mott insulator crossover.

In the Mott phase ($U/J_x \gg 1$), the measured entropy is directly proportional to subsystem size and always smaller than the full system entropy, indicating extensive classical entropy and lack of entanglement. In the superfluid phase (small U/J_x), however, all possible subsystems have more entropy than the full system. The prepared state can hence not be written as a product state with respect to *any* bi-partitioning and exhibits genuine

117
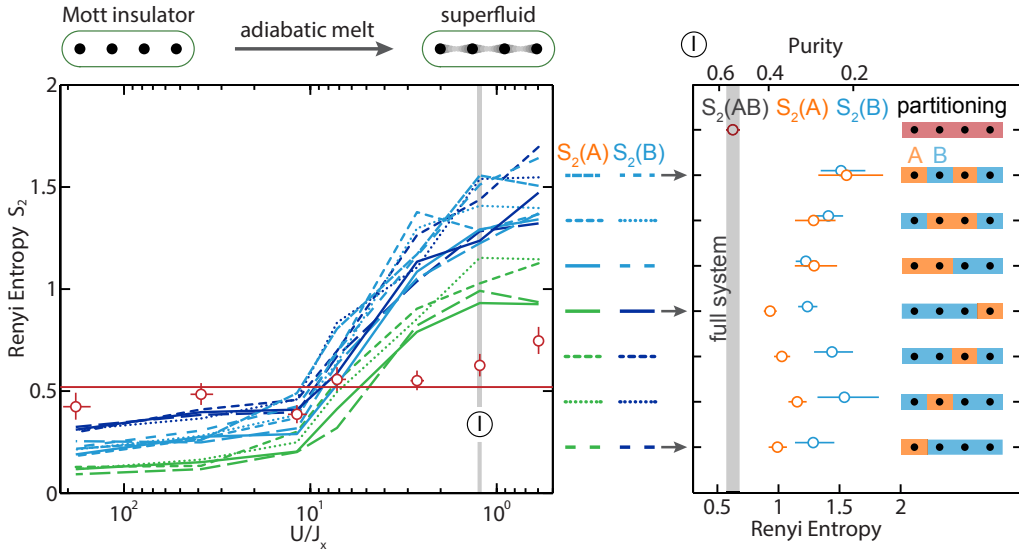
Figure 8.6: Multipartite entanglement. Left: Second-order Rényi entropy of all possible bi-partitionings of the system. In the superfluid regime (small U/J_x), all subsystems (data points connected by green and blue lines) have more entropy than the full system (red circles), indicating full multipartite entanglement between the four lattice sites. In the Mott insulating regime ($U/J_x \gg 1$), the entropy of each subsystem is proportional to its size (indicated by line color), corresponding to extensive entropy. Right: The values of all Rényi entropies of the particular case of $U/J_x \approx 1$, demonstrating spatial multipartite entanglement in the superfluid.

multipartite entanglement, with all sites being entangled with each other [29, 164]. The right panel of Figure 8.6 shows this explicitly for $U/J_x \approx 1$.

8.9 Mutual information

By measuring the second-order Rényi entropy we can calculate other useful quantities, such as the associated mutual information $I_{AB} = S_2(A) + S_2(B) - S_2(AB)$. Mutual information captures quantum and classical correlations between subsystems. In the case of pure quantum states with entanglement between subsystems A and B, $S_2(A) = S_2(B)$ and
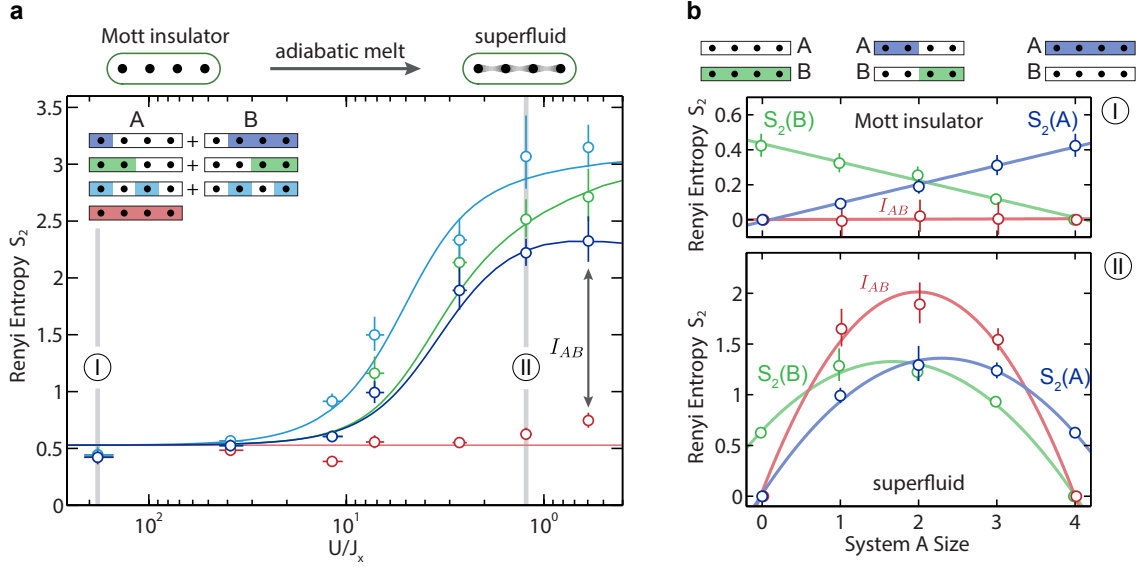
Figure 8.7: Rényi mutual information in the ground state. a) Mutual information is the difference between the summed entropy $S_2(A) + S_2(B)$ for the partitions shown and the entropy of the full system $S_2(AB)$ shown in red. In the Mott insulator phase ($U/J_x \gg 1$) the sites are not correlated, and $I_{AB} \approx 0$. Correlations start to build up for smaller U/J_x, resulting in a non-zero mutual information. b) Top: In the Mott insulator phase classical entropy dominates over entanglement entropy and $S_2(A)$ and $S_2(B)$ increase with the size of the subsystem. The mutual information $I_{AB} \approx 0$. Bottom: S_A, S_B show non-monotonic behavior, due to the dominance of entanglement over classical entropy, which makes the curves asymmetric. I_{AB} restores the symmetry by removing the classical uncorrelated noise. The solid lines are linear (top) and quadratic (bottom) fits as guide to the eye.

$S_2(AB) = 0$, so $I_{AB} = 2S_2(A)$. For a completely uncorrelated system with extensive entropy, on the other hand, $S_2(AB) = S_2(A) + S_2(B)$, and the mutual information vanishes.

Mutual information exhibits interesting scaling properties with respect to the subsystem size, which can be key to studying area laws in interacting quantum systems [146]. In some cases, such as in the "data hiding states" [165], mutual information is more appropriate than the more conventional two-point correlators which might take arbitrarily small values despite the presence of strong correlations. Mutual information is also immune to the extensive classical entropy present in the experiments, and hence is of practical use in
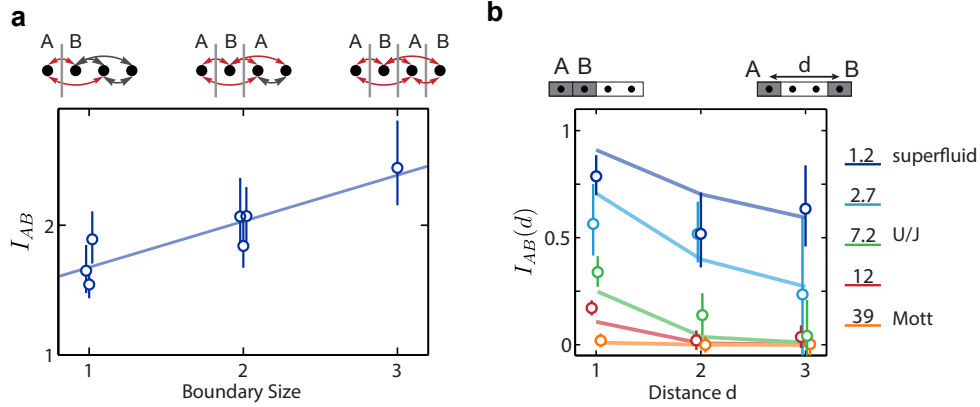
Figure 8.8: Mutual information for different partitionings. a) Mutual information originates from truncated correlations across the boundary (red arrows) and increases with boundary area. The data points are for the superfluid regime at $U/J_x \approx 1$ for partitionings shown in Figure 8.6. The solid line is a guide to the eye. b) I_{AB} for two individual lattice sites as a function of the distance d between them. As the Mott insulator adiabatically melts into a superfluid, correlations develop over increasingly large distances. Data points are offset horizontally for visibility. Solid lines connect the theoretical values from an exact diagonalization.

experimental studies of larger systems.

We explore the behavior of the mutual information in the superfluid-insulator crossover in the 4-site system in Figure 8.7 a. For the various partitionings shown, we plot the sum of the subsystem entropies, $S_2(A) + S_2(B)$, and the entropy of the full system $S_2(AB)$. Mutual information is the difference between them. We find that for the Mott insulator state ($U/J_x \gg 1$), the entropy of the full system is the sum of the entropies for the subsystems. The mutual information $I_{AB} \approx 0$ for this state, consistent with a product state in the presence of extensive classical entropy due to measurement imperfections. At $U/J_x \approx 10$, correlations between the subsystems begin to grow as the system adiabatically melts into a superfluid, resulting in non-zero mutual information, $I_{AB} > 0$.

It is instructive to investigate the scaling of Rényi entropy and mutual information with

subsystem size [146, 145] since in larger systems they can characterize quantum phases, for example by measuring the central charge of the underlying quantum field theory [27]. Figure 8.7 b shows these quantities for continuous subsystems A and B, as the boundary between them is translated between the edges of the system.

In the Mott insulating regime (upper panel), the subsystem entropies $S_2(A)$ and $S_2(B)$ are linear in their subsystem size, consistent with a product state and classical, extensive entropy introduced by measurement imperfections. The mutual information shown in red is not sensitive to extensive entropy, and $I_{AB} \approx 0$ for all positions of the boundary.

The superfluid at $U/J_x \approx 1$ displays a very different scaling of the entropies, as shown in the bottom panel of Figure 8.7 b. Here, the subsystem entropies $S_2(A)$ and $S_2(B)$ are dominated by entanglement entropy and subsystem entropies are much larger than in the Mott insulator. The measured Rényi entropy first increases with the system size, then falls again as the subsystem size approaches that of the full system. This non-monotonicity is a signature of the entanglement entropy, as for a pure state the entropy of the subsystems has to be equal ($S_2(A) = S_2(B)$), and is set by the size of the smaller subsystem. The entropy vanishes completely when the subsystem size is zero or the full system. The measured entropies display a small skew due to the presence of extensive classical entropy, as in the Mott insulator. This asymmetry is absent in the mutual information, which is maximized when the two subsystems A and B each comprise one half of the system.

The mutual information between two subsystems originates from the correlations across their separating boundary. We probe this effect by comparing partitionings for a superfluid at $U/J_x \approx 1$ in Figure 8.8 a. We show the mutual information for partitionings from Figure 8.6 as a function of their boundary area, irrespective of subsystem size. Increasing the

surface area between subsystems increases the mutual information, as more correlations are interrupted by the partitioning. The partitioning into discontinuous regions ABAB maximizes the surface area between the subsystems and the mutual information between them.

Mutual information also elucidates the onset of correlations between various sites as the few-body system crosses over from a Mott insulator to a superfluid phase. Figure 8.8 b shows the mutual information between two individual lattice site versus their separation. In the Mott insulator phase ($U/J_x \gg 1$) the mutual information between all sites vanishes. As the particles start to tunnel only the nearest neighbor correlations start to build up ($U/J_x \approx 12$) and the long range correlations remain negligible. Further into the superfluid phase, the correlations extend beyond the nearest neighbor and become long range for smaller U/J_x. These results suggest disparate spatial behavior of the mutual information in the ground state of an uncorrelated (Mott insulator) and a strongly correlated phase (superfluid). For larger systems this scaling behavior can be exploited to identify quantum phases and the onset of quantum phase transitions.

8.10   Non-equilibrium entanglement dynamics

The measurement of entanglement entropy is particularly instructive for dynamics far away from the ground state, such as in many-body quenches. In generic systems, the entropy of entanglement between subsystems grows linearly in time after a quench [166], for example from the strongly to the weakly interacting regime. Qualitatively, this behavior can be understood from the light-cone like spreading of correlations that entangle a subsystem with an increasingly large fraction of the full system. The maximum amount of entanglement is then limited by the size of the subsystem, and the entanglement entropy
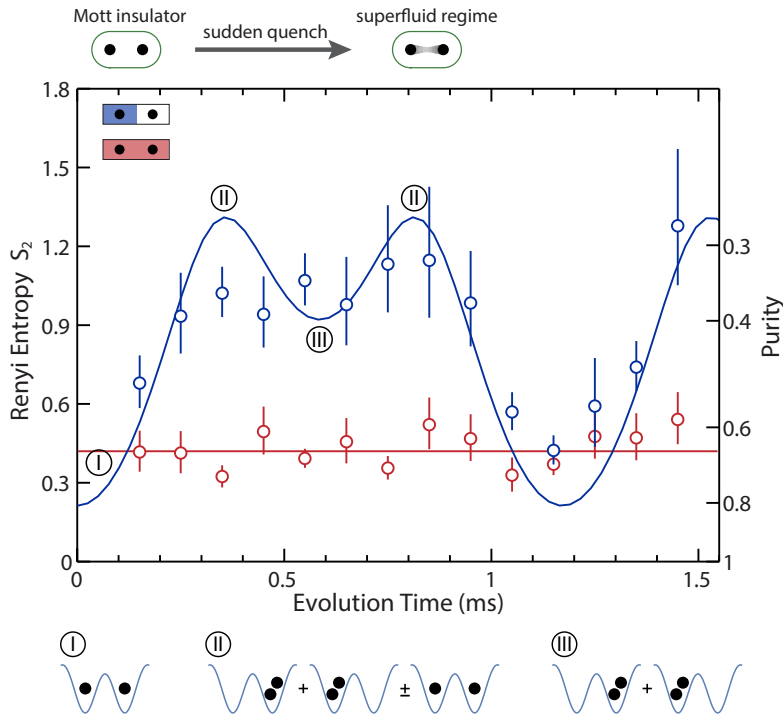
Figure 8.9: Entanglement entropy in a few-particle quench. Dynamics of two atoms in two sites after a sudden quench of the Hamiltonian from $U/J_x \gg 1$ to $U/J_x \approx 0.3$, with $J_x \approx 2\pi \times 210$ Hz. The system oscillates between the Mott-like state (I) and quenched superfluid states (II, III). Solid lines are the theory curves with vertical offsets to include the classical entropy.

will saturate to this value in a state that appears to be thermal in local observables [167].

The linear growth of entanglement entropy in quenches often renders numerical simulations of the dynamics impossible. Entanglement entropy is precisely the quantity that determines the size of the relevant Hilbert spaces in numerical techniques such as the time dependent Density Matrix Renormalization Group (tDMRG) method [168]. Dynamics with large entropy require unfeasibly large computational spaces, establishing an effective upper limit on how much entanglement entropy can be tolerated in numerical simulations, or equivalently a maximum time over which the dynamics can be calculated [169].

We experimentally study entanglement dynamics for the simple case of two particles oscillating in a double-well described by the Bose-Hubbard model, shown in Figure 8.9. We start in the Mott insulating regime ($U/J_x \gg 1$) with a particle localized on either side of the double-well, and suddenly quench the interaction parameter to a low value, $U/J_x \approx 0.3$. The non-equilibrium dynamics leads to oscillations in the second-order Rényi entropy of the subsystem, while the full system assumes a constant value originating from classical entropy.

The quantum state of the system oscillates between unentangled (particles localized in separate wells) and entangled states in the Hilbert space spanned by $|1, 1\rangle$, $|2, 0\rangle$ and $|0, 2\rangle$. Here, $|m, n\rangle$ denotes a state with m and n atoms in the two subsystems (wells), respectively. Starting from the product state $|1, 1\rangle$ the system evolves through the maximally entangled states $|2, 0\rangle + |0, 2\rangle \pm |1, 1\rangle$ and the symmetric, HOM-like state $|2, 0\rangle + |0, 2\rangle$. In the maximally entangled states the subsystems are completely mixed, with a probability of $1/3$ to have zero, one, or two particles. This measurement also demonstrates entanglement in HOM-like interference of two massive particles.

In this experiment, the size of the Hilbert space of the full system is only 3. We therefore observe oscillatory dynamics, with a clear revival after a time set by the inverse energy spacing of the eigenstates, at which the system returns to its non-entangled initial state. These oscillatory dynamics give way to the typical, saturated quench behavior of many-body states as the size of the system increases. Already for 6 bosons on 6 sites, the dimension of the Hilbert space is 462, and no revivals are expected to occur on experimentally relevant timescales.

8.11 Measurement precision

Entanglement entropy is a direct measure of how much of the available configuration space a particular quantum state populates. Observations of highly entangled states hence typically require resource-intensive measurements on high-dimensional spaces.

We encounter this complication in the regime of large entanglement entropy: As the entanglement entropy between subsystems increases, the systems samples an increasingly large number of microstates. The probability of detecting odd parity after the beamsplitter pulse, $p_{\mathrm{odd}} = 1/2(1 - \mathrm{e}^{-S})$, exponentially approaches $1/2$. Extremely small statistical errors on p_{odd} are hence required to determine the entropy accurately. In the limit of large entropies, the number of measurements required to obtain a fractional error ϵ in the entropy is given by $N \approx \left(\frac{1}{\epsilon}\right)^2 \frac{\mathrm{e}^{2S}}{S^2}$. Determining an entropy of 4 with a fractional error of $\pm\,10\,\%$ hence requires $\sim\!20,000$ measurements. Even with massive parallelization, this is likely near the limit of statistics obtainable with current ultracold atom experiments.

However, we emphasize that measuring large entanglement entropy only requires smaller *statistical errors*. In contrast to state tomography, the *number of operations* is independent of system size and entanglement entropy. Verifying that a many-body state is pure (i.e. the probability of odd outcomes is close to zero) remains efficient even for large systems with significant entanglement between subsystems.

8.12 Conclusions

Using generalized Hong-Ou-Mandel interference of many-body states, we have performed a direct measurement of quantum purity, the second-order Rényi entanglement en-

tropy, and mutual information in a Bose-Hubbard system. Our measurement scheme does not rely on full density matrix reconstruction or the use of specialized witness operators to detect entanglement. Instead, by preparing and interfering two identical copies of a many-body quantum state, we probe entanglement with the measurement of only a single operator. Our experiments represent an important demonstration of the usefulness of the many-body interference for the measurement of entanglement. It is straightforward to extend the scheme to fermionic systems [33] and systems with internal degrees of freedom [29]. By generalizing the interference to n copies of the quantum state [151], arbitrary observables written as as n-th order polynomial function of the density matrix, e.g. $n > 2$ order Rényi entropies, can be measured.

With modest technical upgrades to suppress classical fluctuations and residual interactions, it should be possible to further improve the beamsplitter fidelity enabling us to work with significantly larger systems. Mutual information is an ideal tool for exploring these larger systems as it is insensitive to any residual extensive classical entropy. Verifying the scaling laws for entanglement entropy introduced in chapter 7 would be of great significance for the characterization of quantum phases using entanglement entropy.

For non-equilibrium systems, entanglement entropy can grow in time (indefinitely in infinite systems). This leads to interesting many-body physics, such as thermalization in closed quantum systems [167]. The long time growth of entanglement entropy is considered to be a key signature of many-body localized states [170] arising in the presence of disorder. The ability to measure the quantum purity for these systems would allow experimental distinction of quantum fluctuations and classical statistical fluctuations.

More generally, by starting with two different quantum states in the two copies our

scheme can be applied to measure the quantum state overlap between them. This would provide information about the underlying quantum state. For example, the many-body ground state is very sensitive to perturbations near a quantum critical point. Hence, the overlap between two ground states with slightly different parameters (such as U/J in the Bose-Hubbard Hamiltonian) could be used as a sensitive probe of quantum criticality [171]. Similarly the overlap of two copies undergoing non-equilibrium evolution under different perturbations can be used to probe temporal correlation functions in non-equilibrium quantum dynamics.

Chapter 9

Conclusions and outlook

In this thesis, I have presented measurements that directly investigate the defining quantum mechanical characteristics of many-body Bose-Hubbard systems. The effects of quantum statistics, interactions, and entanglement, which are usually observed in the bulk properties of many-particle systems, can be accessed directly in engineered few-body systems, which we control on the single-particle level.

We directly observe bosonic quantum statistics in Hong-Ou-Mandel interference experiments. Controlled tunneling in a double-well potential realizes the equivalent of a beamsplitter for massive particles, and we detect high-contrast two-particle interference. The high interference contrast indicates almost complete loss of distinguishability and high quantum state purity. A possible route to improving the contrast of Hong-Ou-Mandel interference even further would be to use a species with Feshbach resonances for tunable interactions, where the HOM experiment could be performed at zero interaction strength. ^{85}Rb is a suitable candidate for our experiment.

Quantum statistics, together with tunable repulsive interactions, also determine the dy-

namics we observe in two-particle quantum walks. The deterministic preparation of few-body states here realizes an idealized model for quantum systems, where fundamental effects can be explored in conceptually simple settings. We directly observe the fermionization of bosons due to strong interactions and the formation of individual repulsively bound pairs. Ultracold quantum gases are an excellent platform to study many-particle quantum walks because of the deterministic preparation of many indistinguishable particles and the available single-particle control. Interesting problems to tackle would be the boson sampling problem, which requires non-interacting particles, or quantum walks in quasi-periodic systems [172].

Entanglement between the constituent particles of a many-body system is revealed in our measurements of many-body Hong-Ou-Mandel interference. This collective measurement based on two copies of a quantum state gives access to entanglement entropy, which so far has not been measured in itinerant systems. Entanglement entropy plays an important role in many areas of theoretical research, including quantum phase transitions and high energy theory. Our results should elucidate the role of entanglement entropy in different contexts, for example its connection with superselection rules [173].

Outlook

Based on the methods developed in this thesis, many measurements on engineered few-particle systems are within direct reach:

Engineered potentials

Advanced optical potentials Our single-site addressing capabilities can be extended to state-dependent lattices using magic wavelengths [15]. Arbitrary polarization patterns can be created by illuminating the DMD with two beams of orthogonal polarization.

Disorder potentials The DMD can project programmable disorder with correlation lengths as small as one lattice site. Quantum walks in such disordered potentials can probe localization physics [97]. In combination with measurements of entanglement entropy, we could measure entanglement growth in many-body localized systems [38].

Engineered dissipation Using resonant light on the DMD, localized and dynamically variable dissipation on individual lattice sites can be engineered. In the Gross-Pitaevski regime, local dissipation can lead to breathers and self-localization of condensates [174]. Whether such behavior exists in strongly interacting Bose-Hubbard systems is largely an open question. Techniques based on engineered dissipation might also be used for quantum state stabilization [175].

Quantum information processing Low-entropy Mott insulators in combination with optical single-site addressing provide a platform for quantum information processing with thousands of qubits. Quantum logic operations can be performed with dynamically controlled potentials and qubits based on hyperfine states [176]. Alternatively, logic states can be encoded in motional states and gate operations can be performed in static, tailored optical potentials [177].

New cooling techniques   As new methods for ground-state preparation based on Raman sideband cooling are becoming available [178, 179], it might be realistic to assemble few-particle Mott insulators "from scratch" starting with individually trapped atoms. In combination with arbitrary potential landscapes created with DMDs, such systems with fast repetition rates would be a very useful platform to study few-particle entanglement and dynamics.

Many-body interference

The interference of many-body states provides an experimental verification of the purity of a many-body state. This information can be very important for measurements on many-body localized systems [38] in order to distinguish quantum effects from decoherence due to classical noise at long times.

An interesting topic is the evolution of isolated quantum systems after a quench: The dynamics of a closed many-body system after a quench are governed by unitary and reversible evolution to a highly entangled, but pure quantum state. This quantum state in principle preserves complete memory of the initial conditions. On the other hand, from our classical intuition we expect highly excited many-particle systems to settle to an ergodic, thermalized state at long times, with complete memory loss of the precise initial state.

This apparent disparity between classical thermodynamics and unitary evolution can be resolved by the "Eigenstate Thermalization Hypothesis" (ETH) [167]: All eigenstates of a non-integrable many-body system within a certain energy window predict very similar, thermal distributions for most reasonable local observables. The precise distribution of population across eigenstates does not matter, and to close approximation the information

about the initial state is lost.

Our direct measurements of quantum purity combined with evaluations of local observables, such as number fluctuations on individual sites, can directly verify this hypothesis. Even for small systems of $6-8$ sites, clear signatures of ETH should be observable.

Bibliography

[1] R. Blatt and C. F. Roos. Quantum simulations with trapped ions. *Nat. Phys.*, 8:277, 2012.

[2] A. A. Houck, H. E. Türeci, and J. Koch. On-chip quantum simulation with super-conducting circuits. *Nat. Phys.*, 8:292, 2012.

[3] I. L. Garanovich, S. Longhi, A. A. Sukhorukov, and Y. S. Kivshar. Light propagation and localization in modulated photonic lattices and waveguides. *Phys. Rep.*, 518:1, 2012.

[4] V. Mourik, K. Zuo, S. M. Frolov, S. R. Plissard, E. P. A. M. Bakkers, and L. P. Kouwenhoven. Signatures of Majorana fermions in hybrid superconductor-semiconductor nanowire devices. *Science*, 336:1003, 2012.

[5] I. Bloch, J. Dalibard, and S. Nascimbène. Quantum simulations with ultracold quantum gases. *Nat. Phys.*, 8:267, 2012.

[6] M. Lewenstein, A. Sanpera, and V. Ahufinger. *Ultracold atoms in optical lattices*. Oxford University Press, Oxford, 2012.

[7] C. Chin, R. Grimm, P. Julienne, and E. Tiesinga. Feshbach resonances in ultracold gases. *Rev. Mod. Phys.*, 82:1225, 2010.

[8] W. S Bakr, J. I. Gillen, A. Peng, S. Fölling, and M. Greiner. A quantum gas micro-scope for detecting single atoms in a Hubbard-regime optical lattice. *Nature*, 462:74, 2009.

[9] J. F. Sherson, C. Weitenberg, M. Endres, M. Cheneau, I. Bloch, and S. Kuhr. Single-atom resolved fluorescence imaging of an atomic Mott insulator. *Nature*, 467:68, 2010.

[10] M. Miranda, R. Inoue, Y. Okuyama, A. Nakamoto, and M. Kozuma. Site-resolved imaging of ytterbium atoms in a two-dimensional optical lattice. *Phys. Rev. A*, 91:063414, 2015.

[11] E. Haller, J. Hudson, A. Kelly, D. A. Cotta, B. Peaudecerf, G. D. Bruce, and S. Kuhr. Single-atom imaging of fermions in a quantum gas microscope. *Nat. Phys.*, 11:738, 2015.

[12] M. F. Parsons, F. Huber, A. Mazurenko, C. S. Chiu, W. Setiawan, K. Wooley-Brown, S. Blatt, and M. Greiner. Site-resolved imaging of fermionic ^{6}Li in an optical lattice. *Phys. Rev. Lett.*, 114:213002, 2015.

[13] L. W. Cheuk, M. A. Nichols, M. Okan, T. Gersdorf, V. V. Ramasesh, W. S. Bakr, T. Lompe, and M. W. Zwierlein. Quantum-gas microscope for fermionic atoms. *Phys. Rev. Lett.*, 114:193001, 2015.

[14] M. Endres, M. Cheneau, T. Fukuhara, C. Weitenberg, P. Schauß, C. Gross, L. Mazza, M. C. Bañuls, L. Pollet, I. Bloch, and S. Kuhr. Observation of correlated particle-hole pairs and string order in low-dimensional Mott insulators. *Science*, 334:200, 2011.

[15] C. Weitenberg, M. Endres, J. F. Sherson, M. Cheneau, P. Schauß, T. Fukuhara, I. Bloch, and S. Kuhr. Single-spin addressing in an atomic Mott insulator. *Nature*, 471:319, 2011.

[16] Y. Wang, X. Zhang, T. A. Corcovilos, A. Kumar, and D. S. Weiss. Coherent addressing of individual neutral atoms in a 3D optical lattice. *Phys. Rev. Lett.*, 115:043003, 2015.

[17] K. Manouchehri and J. Wang. *Physical Implementation of Quantum Walks*. Springer-Verlag, Berlin, 2014.

[18] C. K. Hong, Z. Y. Ou, and L. Mandel. Measurement of subpicosecond time intervals between two photons by interference. *Phys. Rev. Lett.*, 59:2044, 1987.

[19] R. Horodecki, P. Horodecki, M. Horodecki, and K. Horodecki. Quantum entanglement. *Rev. Mod. Phys.*, 81:865, 2009.

[20] M. A. Nielsen and I. L. Chuang. *Quantum computation and quantum information*. Cambridge University Press, Cambridge, 2010.

[21] V. Giovannetti, S. Lloyd, and L. Maccone. Advances in quantum metrology. *Nat. Phys.*, 5:222, 2011.

[22] L. Amico, R. Fazio, A. Osterloh, and V. Vedral. Entanglement in many-body systems. *Rev. Mod. Phys.*, 80:517, 2008.

[23] O. Gühne and G. Tóth. Entanglement detection. *Phys. Rep.*, 474:1, 2009.

[24] D. Bouwmeester, J.-W. Pan, M. Daniell, H. Weinfurter, and A. Zeilinger. Observation of three-photon Greenberger-Horne-Zeilinger entanglement. *Phys. Rev. Lett.*, 82:1345, 1999.

[25] H. Häffner, W. Hänsel, C. F. Roos, J. Benhelm, D. Chek-al kar, M. Chwalla, T Körber, U. D. Rapol, M. Riebe, P. O. Schmidt, C. Becher, O. Gühne, W. Dür, and R. Blatt. Scalable multiparticle entanglement of trapped ions. *Nature*, 438:643, 2005.

[26] A. Osterloh, L. Amico, G. Falci, and R. Fazio. Scaling of entanglement close to a quantum phase transition. *Nature*, 416:608, 2002.

[27] P. Calabrese and J. Cardy. Entanglement entropy and conformal field theory. *J. Phys. A: Math. Theor.*, 42:504005, 2009.

[28] T. Nishioka, S. Ryu, and T. Takayanagi. Holographic entanglement entropy: an overview. *J. Phys. A: Math. Theor.*, 42:504008, 2009.

[29] C. Moura Alves and D. Jaksch. Multipartite entanglement detection in bosons. *Phys. Rev. Lett.*, 93:110501, 2004.

[30] A. J. Daley, H. Pichler, J. Schachenmayer, and P. Zoller. Measuring entanglement growth in quench dynamics of bosons in an optical lattice. *Phys. Rev. Lett.*, 109:020505, 2012.

[31] M. Levin and X.-G. Wen. Detecting topological order in a ground state wave function. *Phys. Rev. Lett.*, 96:110405, 2006.

[32] A. Kitaev and J. Preskill. Topological entanglement entropy. *Phys. Rev. Lett.*, 96:110404, 2006.

[33] H. Pichler, L. Bonnes, A. J. Daley, A. M. Läuchli, and P. Zoller. Thermal versus entanglement entropy: a measurement protocol for fermionic atoms with a quantum gas microscope. *New J. Phys.*, 15:063003, 2013.

[34] R. P. Feynman. Simulating physics with computers. *Int. J. Theor. Phys.*, 21:467, 1982.

[35] M. Aidelsburger, M. Atala, S. Nascimbène, S. Trotzky, Y.-A. Chen, and I. Bloch. Experimental realization of strong effective magnetic fields in an optical lattice. *Phys. Rev. Lett.*, 107:255301, 2011.

[36] H. Miyake, G. A. Siviloglou, C. J. Kennedy, W. C. Burton, and W. Ketterle. Realizing the Harper Hamiltonian with laser-assisted tunneling in optical lattices. *Phys. Rev. Lett.*, 111:185302, 2013.

[37] G. Jotzu, M. Messer, R. Desbuquois, M. Lebrat, T. Uehlinger, D. Greif, and T. Esslinger. Experimental realization of the topological Haldane model with ultracold fermions. *Nature*, 515:237, 2014.

[38] M. Schreiber, S. S. Hodgman, P. Bordia, H. P. Lüschen, M. H. Fischer, R. Vosk, E. Altman, U. Schneider, and I. Bloch. Observation of many-body localization of interacting fermions in a quasi-random optical lattice. *Science*, 349:842, 2015.

[39] Y. Aharonov, L. Davidovich, and N. Zagury. Quantum random walks. *Phys. Rev. A*, 48:1687, 1993.

[40] E. Farhi and S. Gutmann. Quantum computation and decision trees. *Phys. Rev. A*, 58:915, 1998.

[41] S. E. Venegas-Andraca. Quantum walks: a comprehensive review. *Quantum Inf. Process.*, 11:1015, 2012.

[42] A. M. Kaufman, B. J. Lester, C. M. Reynolds, M. L. Wall, M. Foss-Feig, K. R. A Hazzard, A. M. Rey, and C. A. Regal. Two-particle quantum interference in tunnel-coupled optical tweezers. *Science*, 345:306, 2014.

[43] R. Lopes, A. Imanaliev, A. Aspect, M. Cheneau, D. Boiron, and C. I. Westbrook. Atomic Hong-Ou-Mandel experiment. *Nature*, 520:66, 2015.

[44] A. K. Ekert, C. Moura Alves, D. K. L. Oi, M. Horodecki, P. Horodecki, and L. C. Kwek. Direct estimations of linear and nonlinear functionals of a quantum state. *Phys. Rev. Lett.*, 88:217901, 2002.

[45] R. Horodecki and P. Horodecki. Quantum redundancies and local realism. *Phys. Lett. A*, 194:147, 1994.

[46] M. Greiner, O. Mandel, T. Esslinger, T. W. Hänsch, and I. Bloch. Quantum phase transition from a superfluid to a Mott insulator in a gas of ultracold atoms. *Nature*, 415:39, 2002.

[47] C. Becker, P. Soltan-Panahi, J. Kronjäger, S. Dörscher, K. Bongs, and K. Sengstock. Ultracold quantum gases in triangular optical lattices. *New J. Phys.*, 12:065025, 2010.

[48] G.-B. Jo, J. Guzman, C. K. Thomas, P. Hosur, A. Vishwanath, and D. M. Stamper-Kurn. Ultracold atoms in a tunable optical Kagome lattice. *Phys. Rev. Lett.*, 108:045305, 2012.

[49] D. Greif, T. Uehlinger, G. Jotzu, L. Tarruell, and T. Esslinger. Short-range quantum magnetism of ultracold fermions in an optical lattice. *Science*, 340:1307, 2013.

[50] M. Greiner. *Ultracold quantum gases in three-dimensional optical lattice potentials*. PhD thesis, Ludwig-Maximilians-Universität München, 2003.

[51] S. Folling. *Probing strongly correlated states of ultracold atoms in optical lattices*. PhD thesis, Johannes Gutenberg-Universität Mainz, 2008.

[52] L.-M. Duan, E. Demler, and M. D. Lukin. Controlling spin exchange interactions of ultracold atoms in optical lattices. *Phys. Rev. Lett.*, 91:090402, 2003.

[53] A. Kleine, C. Kollath, I. P. McCulloch, T. Giamarchi, and U. Schollwöck. Spin-charge separation in two-component Bose gases. *Phys. Rev. A*, 77:013607, 2008.

[54] S. Sachdev. *Quantum Phase Transitions*. Cambridge University Press, Cambridge, 2011.

[55] W. S. Bakr, A. Peng, M. E. Tai, R. Ma, J. Simon, J. I. Gillen, L. Fölling, S.and Pollet, and M. Greiner. Probing the superfluid–to–Mott insulator transition at the single-atom level. *Science*, 329:547, 2010.

[56] T. Stöferle, H. Moritz, C. Schori, M. Köhl, and T. Esslinger. Transition from a strongly interacting 1D superfluid to a Mott insulator. *Phys. Rev. Lett.*, 92:130403, 2004.

[57] M. A. Cazalilla, R. Citro, T. Giamarchi, E. Orignac, and M. Rigol. One dimensional bosons: From condensed matter systems to ultracold gases. *Rev. Mod. Phys.*, 83:1405, 2011.

[58] M. Girardeau. Relationship between systems of impenetrable bosons and fermions in one dimension. *J. Math. Phys.*, 1:516, 1960.

[59] B. Paredes, A. Widera, V. Murg, O. Mandel, S. Fölling, I. Cirac, G. Shlyapnikov, T. W. Hänsch, and I. Bloch. Tonks-Girardeau gas of ultracold atoms in an optical lattice. *Nature*, 429:277, 2004.

[60] T. Kinoshita, T. Wenger, and D. S. Weiss. A quantum Newton's cradle. *Nature*, 440:900, 2006.

[61] T. Fukuhara, P. Schauß, M. Endres, S. Hild, M. Cheneau, I. Bloch, and C. Gross. Microscopic observation of magnon bound states and their dynamics. *Nature*, 502:76, 2013.

[62] J. Simon, W. S. Bakr, R. Ma, M. E. Tai, P. M. Preiss, and M. Greiner. Quantum simulation of antiferromagnetic spin chains in an optical lattice. *Nature*, 472:307, 2011.

[63] T. Giamarchi. *Quantum physics in one dimension*. Clarendon Press, Oxford, 2003.

[64] O. Jürgensen, F. Meinert, M. J. Mark, H.-C. Nägerl, and D.-S. Lühmann. Observation of density-induced tunneling. *Phys. Rev. Lett.*, 113:193003, 2014.

[65] R. Ma, M. E. Tai, P. M. Preiss, W. S. Bakr, J. Simon, and M. Greiner. Photon-assisted tunneling in a biased strongly correlated Bose gas. *Phys. Rev. Lett.*, 107:095301, 2011.

[66] D.-S. Lühmann, O. Jürgensen, and K. Sengstock. Multi-orbital and density-induced tunneling of bosons in optical lattices. *New J. Phys.*, 14:033021, 2012.

[67] U. Bissbort, F. Deuretzbacher, and W. Hofstetter. Effective multibody-induced tunneling and interactions in the Bose-Hubbard model of the lowest dressed band of an optical lattice. *Phys. Rev. A*, 86:023617, 2012.

[68] S. Trotzky, P. Cheinet, S. Fölling, M. Feld, U. Schnorrberger, A. M. Rey, A. Polkovnikov, E. A. Demler, M. D. Lukin, and I. Bloch. Time-resolved observation and control of superexchange interactions with ultracold atoms in optical lattices. *Science*, 319:295, 2008.

[69] N. Goldman, G. Juzeliūnas, P. Öhberg, and I. B. Spielman. Light-induced gauge fields for ultracold atoms. *Rep. Prog. Phys.*, 77:126401, 2014.

[70] M. Aidelsburger, M. Lohse, C. Schweizer, M. Atala, J. T. Barreiro, S. Nascimbène, N. R. Cooper, I. Bloch, and N. Goldman. Measuring the Chern number of Hofstadter bands with ultracold bosonic atoms. *Nat. Phys.*, 11:162, 2015.

[71] J. I. Gillen. *The quantum gas microscope*. PhD thesis, Harvard University, 2009.

[72] A. Peng. *Quantum gas microscope with optical lattice*. PhD thesis, Harvard University, 2010.

[73] W. Bakr. *Microscopic studies of quantum phase transitions in optical lattices*. PhD thesis, Harvard University, 2011.

[74] R. Ma. *Engineered potentials and dynamics of ultracold quantum gases under the microscope*. PhD thesis, Harvard University, 2014.

[75] K. D. Nelson, X. Li, and D. S. Weiss. Imaging single atoms in a three-dimensional array. *Nat. Phys.*, 3:556, 2007.

[76] J. Catani, G. Lamporesi, D. Naik, M. Gring, M. Inguscio, F. Minardi, A. Kantian, and T. Giamarchi. Quantum dynamics of impurities in a one-dimensional Bose gas. *Phys. Rev. A*, 85:023623, 2012.

[77] S. Palzer, C. Zipkes, C. Sias, and M. Köhl. Quantum transport through a Tonks-Girardeau gas. *Phys. Rev. Lett.*, 103:150601, 2009.

[78] N. Lundblad, J. M. Obrecht, I. B. Spielman, and J. V. Porto. Field-sensitive addressing and control of field-insensitive neutral-atom qubits. *Nat. Phys.*, 5:575, 2009.

[79] T. Gericke, P. Würtz, D. Reitz, T. Langen, and H. Ott. High-resolution scanning electron microscopy of an ultracold quantum gas. *Nat. Phys.*, 4:949, 2008.

[80] D. R. Scherer, C. N. Weiler, T. W. Neely, and B. P. Anderson. Vortex formation by merging of multiple trapped Bose-Einstein condensates. *Phys. Rev. Lett.*, 98:110402, 2007.

[81] P. Schauß. *High-resolution imaging of ordering in Rydberg many-body systems*. PhD thesis, Ludwig-Maximilians-Universität München, February 2015.

[82] V. Boyer, R. M. Godun, G. Smirne, D. Cassettari, C. M. Chandrashekar, A. B. Deb, Z. J. Laczik, and C. J. Foot. Dynamic manipulation of Bose-Einstein condensates with a spatial light modulator. *Phys. Rev. A*, 73:031402, 2006.

[83] A. L. Gaunt and Z. Hadzibabic. Robust digital holography for ultracold atom trapping. *Sci. Rep.*, 2:721, 2012.

[84] F. Nogrette, H. Labuhn, S. Ravets, D. Barredo, L. Béguin, A. Vernier, T. Lahaye, and A. Browaeys. Single-atom trapping in holographic 2D arrays of microtraps with arbitrary geometries. *Phys. Rev. X*, 4:021034, 2014.

[85] Čižmár T., M. Mazilu, and K. Dholakia. *In situ* wavefront correction and its application to micromanipulation. *Nature Photon.*, 4:388, 2010.

[86] P. Zupancic. Dynamic holography and beamshaping using digital micromirror devices. Master's thesis, Ludwig-Maximilians-Universität München, 2013.

[87] M. Leutenegger, R. Rao, R. A. Leitgeb, and T. Lasser. Fast focus field calculations. *Opt. Express*, 14:11277, 2006.

[88] A. Kantian, U. Schollwöck, and T. Giamarchi. Competing regimes of motion of 1D mobile impurities. *Phys. Rev. Lett.*, 113:070601, 2014.

[89] P. Smacchia, M. Knap, E. Demler, and A. Silva. Exploring dynamical phase transitions and prethermalization with quantum noise of excitations. *Phys. Rev. B*, 91:205136, 2015.

[90] T. Fukuhara, S. Hild, J. Zeiher, P. Schauß, I. Bloch, M. Endres, and C. Gross. Spatially resolved detection of a spin-entanglement wave in a Bose-Hubbard chain. *Phys. Rev. Lett.*, 115:035302, 2015.

[91] Y. Bromberg, Y. Lahini, R. Morandotti, and Y. Silberberg. Quantum and classical correlations in waveguide lattices. *Phys. Rev. Lett.*, 102:253904, 2009.

[92] S. Aaronson and A. Arkhipov. The computational complexity of linear optics. *Proc. 43rd ACM STOC*, page 333, 2011.

[93] M. C. Tichy. Interference of identical particles from entanglement to boson-sampling. *J. Phys. B: At. Mol. Opt. Phys.*, 47:103001, 2014.

[94] E. Knill, R. Laflamme, and G. J. Milburn. A scheme for efficient quantum computation with linear optics. *Nature*, 409:46, 2001.

[95] Y. Lahini, M. Verbin, S. D. Huber, Y. Bromberg, R. Pugatch, and Y. Silberberg. Quantum walk of two interacting bosons. *Phys. Rev. A*, 86:011603, 2012.

[96] A. Ahlbrecht, A. Alberti, D. Meschede, V. B. Scholz, A. H. Werner, and R. F. Werner. Molecular binding in interacting quantum walks. *New J. Phys.*, 14:073050, 2012.

[97] D. L. Shepelyansky. Coherent propagation of two interacting particles in a random potential. *Phys. Rev. Lett.*, 73:2607, 1994.

[98] N. Spagnolo, C. Vitelli, M. Bentivegna, D. J. Brod, A. Crespi, F. Flamini, S. Giacomini, G. Milani, R. Ramponi, P. Mataloni, R. Osellame, E. F. Galvao, and F. Sciarrino. Experimental validation of photonic boson sampling. *Nature Photon.*, 8:615, 2014.

[99] A. M. Childs, D. Gosset, and Z. Webb. Universal computation by multiparticle quantum walk. *Science*, 339:791, 2013.

[100] H. Schmitz, R. Matjeschk, C. Schneider, J. Glueckert, M. Enderlein, T. Huber, and T. Schaetz. Quantum walk of a trapped ion in phase space. *Phys. Rev. Lett.*, 103:090504, 2009.

[101] F. Zähringer, G. Kirchmair, R. Gerritsma, E. Solano, R. Blatt, and C. F. Roos. Realization of a quantum walk with one and two trapped ions. *Phys. Rev. Lett.*, 104:100503, 2010.

[102] M. Karski, L. Förster, J.-M. Choi, A. Steffen, W. Alt, D. Meschede, and A. Widera. Quantum walk in position space with single optically trapped atoms. *Science*, 325:174, 2009.

[103] P. Jurcevic, B. P. Lanyon, P. Hauke, C. Hempel, P. Zoller, R. Blatt, and C. F. Roos. Quasiparticle engineering and entanglement propagation in a quantum many-body system. *Nautre*, 511:202, 2014.

[104] A. Schreiber, A. Gábris, P. P. Rohde, K. Laiho, M. Štefaňák, V. Potoček, C. Hamilton, I. Jex, and C. Silberhorn. A 2D quantum walk simulation of two-particle dynamics. *Science*, 336:55, 2012.

[105] G. Corrielli, A. Crespi, G. Della Valle, S. Longhi, and R. Osellame. Fractional Bloch oscillations in photonic lattices. *Nat. Commun.*, 4:1555, 2013.

[106] T. Hartmann, F. Keck, H. J. Korsch, and S. Mossmann. Dynamics of Bloch oscillations. *New J. Phys.*, 6:2, 2004.

[107] M. B. Dahan, E. Peik, J. Reichel, Y. Castin, and C. Salomon. Bloch oscillations of atoms in an optical potential. *Phys. Rev. Lett.*, 76:4508, 1996.

[108] A. Alberti, V. V. Ivanov, G. M. Tino, and G. Ferrari. Engineering the quantum transport of atomic wavefunctions over macroscopic distances. *Nature Phys.*, 5:547, 2009.

[109] E. Haller, R. Hart, M. J. Mark, J. G. Danzl, L. Reichsöllner, and H.-C. Nägerl. Inducing transport in a dissipation-free lattice with super Bloch oscillations. *Phys. Rev. Lett.*, 104:200403, 2010.

[110] M. Genske, W. Alt, A. Steffen, A. H. Werner, R. F. Werner, D. Meschede, and A. Alberti. Electric quantum walks with individual atoms. *Phys. Rev. Lett.*, 110:190601, 2013.

[111] M. A. Broome, A. Fedrizzi, B. P. Lanyon, I. Kassal, A. Aspuru-Guzik, and A. G. White. Discrete single-photon quantum walks with tunable decoherence. *Phys. Rev. Lett.*, 104:153602, 2010.

[112] R. Hanbury Brown and R. Q. Twiss. Correlations between photons in two coherent beams of light. *Nature*, 177:27, 1956.

[113] S. Fölling, F. Gerbier, A. Widera, O. Mandel, T. Gericke, and I. Bloch. Spatial quantum noise interferometry in expanding ultracold atom clouds. *Nature*, 434:481, 2005.

[114] T. Jeltes, J. M. McNamara, W. Hogervorst, W. Vassen, V. Krachmalnicoff, M. Schellekens, A. Perrin, H. Chang, D. Boiron, A. Aspect, and C. I. Westbrook. Comparison of the Hanbury Brown-Twiss effect for bosons and fermions. *Nature*, 445:402, 2007.

[115] A. Peruzzo, M. Lobino, J. C. F. Matthews, N. Matsuda, A. Politi, K. Poulios, X.-Q. Zhou, Y. Lahini, N. Ismail, K. Wörhoff, Y. Bromberg, Y. Silberberg, M. G. Thompson, and J. L. O'Brien. Quantum walks of correlated photons. *Science*, 329:1500, 2010.

[116] L. Sansoni, F. Sciarrino, G. Vallone, P. Mataloni, A. Crespi, R. Ramponi, and R. Osellame. Two-particle bosonic-fermionic quantum walk via integrated photonics. *Phys. Rev. Lett.*, 108:010502, 2012.

[117] T. Kinoshita, T. Wenger, and D. S. Weiss. Observation of a one-dimensional Tonks-Girardeau gas. *Science*, 305:1125, 2004.

[118] K. Winkler, G. Thalhammer, F. Lang, R. Grimm, J. Hecker Denschlag, A. J. Daley, A. Kantian, H. P. Büchler, and P. Zoller. Repulsively bound atom pairs in an optical lattice. *Nature*, 441:853, 2006.

[119] J. Hecker Denschlag and A. J. Daley. Exotic atom pairs: Repulsively bound atom pairs in an optical lattice. *arXiv:cond-mat/0610393*, 2006.

[120] S. Fölling, S. Trotzky, P. Cheinet, M. Feld, R. Saers, A. Widera, T. Müller, and I. Bloch. Direct observation of second-order atom tunnelling. *Nature*, 448:1029, 2007.

[121] W. S. Dias, E. M. Nascimento, M. L. Lyra, and F. A. B. F. de Moura. Frequency doubling of Bloch oscillations for interacting electrons in a static electric field. *Phys. Rev. B*, 76:155124, 2007.

[122] R. Khomeriki, D. O. Krimer, M. Haque, and S. Flach. Interaction-induced fractional Bloch and tunneling oscillations. *Phys. Rev. A*, 81:065601, 2010.

[123] F. Meinert, M. J. Mark, E. Kirilov, K. Lauber, P. Weinmann, M. Gröbner, A. J. Daley, and H.-C. Nägerl. Observation of many-body dynamics in long-range tunneling after a quantum quench. *Science*, 344:1259, 2014.

[124] J. C. F. Matthews, K. Poulios, J. D. A. Meinecke, A. Politi, A. Peruzzo, N. Ismail, K. Wörhoff, M. G. Thompson, and J. L. O'Brien. Observing fermionic statistics with photons in arbitrary processes. *Scientific Reports*, 3:1539, 2013.

[125] L. Wang, L. Wang, and Y. Zhang. Quantum walks of two interacting anyons in one-dimensional optical lattices. *Phys. Rev. A*, 90:063618, 2014.

[126] T. Keilmann, S. Lanzmich, I. McCulloch, and M. Roncaglia. Statistically induced phase transition and anyons in 1D optical lattices. *Nat. Comm.*, 2:361, 2011.

[127] A. Sipahigil, M. L. Goldman, E. Togan, Y. Chu, M. Markham, D. J. Twitchen, A. S. Zibrov, A. Kubanek, and M. D. Lukin. Quantum interference of single photons from remote nitrogen-vacancy centers in diamond. *Phys. Rev. Lett.*, 108:143601, 2012.

[128] D. L. Moehring, P. Maunz, S. Olmschenk, Younge K. C., D. N. Matsukevich, L.-M. Duan, and C. Monroe. Entanglement of single-atom quantum bits at a distance. *Nature*, 449:68, 2007.

[129] E. Bocquillon, V. Freulon, J.-M. Berroir, P. Degiovanni, B. Plaçais, A. Cavanna, Y. Jin, and Fève. Coherence and indistinguishability of single electrons emitted from independent sources. *Science*, 339:1054, 2013.

[130] K. M. R. Audenaert and S. Scheel. Statistical inference from imperfect photon detection. *New J. Phys.*, 12:113052, 2009.

[131] Z. Y. Ou. Multi-photon interference and temporal distinguishability of photons. *Int. J. Mod. Phys. B*, 21:5033, 2007.

[132] O. Cosme, S. Pádua, F. A. Bovino, A. Mazzei, F. Sciarrino, and F. De Martini. Hong-Ou-Mandel interferometer with one and two photon pairs. *Phys. Rev. A*, 77:053822, 2008.

[133] J. S. Bell. On the Einstein-Podolsky-Rosen paradox. *Physics*, 1:195, 1964.

[134] J. F. Clauser, M. A. Horne, A. Shimony, and R. A. Holt. Proposed experiment to test local hidden-variable theories. *Phys. Rev. Lett.*, 23:880, 1969.

[135] A. Aspect. Bell's inequality test: more ideal than ever. *Nature*, 398:189, 1999.

[136] A. Aspuru-Guzik and P. Walther. Photonic quantum simulators. *Nat. Phys.*, 8:285, 2012.

[137] S. P. Walborn, P. H. Souto Ribeiro, L. Davidovich, F. Mintert, and A. Buchleitner. Experimental determination of entanglement with a single measurement. *Nature*, 440:1022, 2006.

[138] H. Bernien, B. Hensen, W. Pfaff, G. Koolstra, M. S. Blok, L. Robledo, T. H. Taminiau, M. Markham, D. J. Twitchen, L. Childress, and R. Hanson. Heralded entanglement between solid-state qubits separated by three metres. *Nature*, 497:86, 2013.

[139] O. Mandel, M. Greiner, A. Widera, T. Rom, T. W. Hänsch, and I. Bloch. Controlled collisions for multi-particle entanglement of optically trapped atoms. *Nature*, 425:937, 2003.

[140] H.-C. Jiang, Z. Wang, and L. Balents. Identifying topological order by entanglement entropy. *Nat. Phys.*, 8:902, 2012.

[141] Y. Zhang, T. Grover, and A. Vishwanath. Entanglement entropy of critical spin liquids. *Phys. Rev. Lett.*, 107:067202, 2011.

[142] S. V. Isakov, M. B. Hastings, and R. G. Melko. Topological entanglement entropy of a Bose-Hubbard spin liquid. *Nat. Phys.*, 7:772, 2011.

[143] G. Vidal, J. I. Latorre, E. Rico, and A. Kitaev. Entanglement in quantum critical phenomena. *Phys. Rev. Lett.*, 90:227902, 2003.

[144] S.-J. Gu, S.-S. Deng, Y.-Q. Li, and H.-Q. Lin. Entanglement and quantum phase transition in the extended Hubbard model. *Phys. Rev. Lett.*, 93:086402, 2004.

[145] J. Eisert, M. Cramer, and M. B. Plenio. Colloquium: Area laws for the entanglement entropy. *Rev. Mod. Phys.*, 82:277, 2010.

[146] M. M. Wolf, F. Verstraete, M. B. Hastings, and J. I. Cirac. Area laws in quantum systems: Mutual information and correlations. *Phys. Rev. Lett.*, 100:070502, 2008.

[147] P. Calabrese and J. Cardy. Entanglement entropy and quantum field theory. *J. Stat. Mech.*, 2004:P06002, 2004.

[148] J. P. Keating, F. Mezzadri, and M. Novaes. Comb entanglement in quantum spin chains. *Phys. Rev. A*, 74:012311, 2006.

[149] D. F. V. James, P. G. Kwiat, W. J. Munro, and A. G. White. Measurement of qubits. *Phys. Rev. A*, 64:052312, 2001.

[150] J.-W. Pan, Z.-B. Chen, C.-Y. Lu, H. Weinfurter, A. Zeilinger, and M. Żukowski. Multiphoton entanglement and interferometry. *Rev. Mod. Phys.*, 84:777, 2012.

[151] T. A. Brun. Measuring polynomial functions of states. *Quantum Information and Computation*, 4:401, 2004.

[152] F. A. Bovino, G. Castagnoli, A. Ekert, P. Horodecki, C. Moura Alves, and A. V. Sergienko. Direct measurement of nonlinear properties of bipartite quantum states. *Phys. Rev. Lett.*, 95:240407, 2005.

[153] C. Schmid, N. Kiesel, W. Wieczorek, H. Weinfurter, and A. Mintert, F.and Buchleitner. Experimental direct observation of mixed state entanglement. *Phys. Rev. Lett.*, 101:260505, 2008.

[154] R. Horodecki and M. Horodecki. Information-theoretic aspects of inseparability of mixed states. *Phys. Rev. A*, 54:1838, 1996.

[155] F. Mintert and A. Buchleitner. Observable entanglement measure for mixed quantum states. *Phys. Rev. Lett.*, 98:140505, 2007.

[156] H. Li and F. D. M. Haldane. Entanglement spectrum as a generalization of entanglement entropy: Identification of topological order in non-abelian fractional quantum Hall effect states. *Phys. Rev. Lett.*, 101:010504, 2008.

[157] M. C. Tichy, F. Mintert, and A. Buchleitner. Essential entanglement for atomic and molecular physics. *J Phys. B.: At. Mol. Opt. Phys.*, 44:192001, 2011.

[158] M. A. Nielsen. Conditions for a class of entanglement transformations. *Phys. Rev. Lett.*, 83:436, 1999.

[159] F. Mintert. Entanglement measures as physical observables. *Appl. Phys. B*, 89:493, 2007.

[160] D. A. Abanin and E. Demler. Measuring entanglement entropy of a generic many-body system with a quantum switch. *Phys. Rev. Lett.*, 109:020504, 2012.

[161] M. Cramer, A. Bernard, N. Fabbri, L. Fallani, C. Fort, S. Rosi, F. Caruso, M. Inguscio, and M. B. Plenio. Spatial entanglement of bosons in optical lattices. *Nat. Commun.*, 4:2161, 2013.

[162] S. D. Bartlett and H. M. Wiseman. Entanglement constrained by superselection rules. *Phys. Rev. Lett.*, 91:097903, 2003.

[163] N. Schuch, F. Verstraete, and J. I. Cirac. Nonlocal resources in the presence of superselection rules. *Phys. Rev. Lett.*, 92:087904, 2004.

[164] R. N. Palmer, C. Moura Alves, and D. Jaksch. Detection and characterization of multipartite entanglement in optical lattices. *Phys. Rev. A*, 72:042335, 2005.

[165] B. M. Terhal, D. P. DiVincenzo, and D. W. Leung. Hiding bits in Bell states. *Phys. Rev. Lett.*, 86:5807, 2001.

[166] P. Calabrese and J. Cardy. Evolution of entanglement entropy in one-dimensional systems. *J. Stat. Mech.*, 2005:P04010, 2005.

[167] M. Rigol, V. Dunjko, and M. Olshanii. Thermalization and its mechanism for generic isolated quantum systems. *Nature*, 452:854, 2008.

[168] G. Vidal. Efficient simulation of one-dimensional quantum many-body systems. *Phys. Rev. Lett.*, 93:040502, 2004.

[169] S. Trotzky, Y.-A. Chen, A. Flesch, I. P. McCulloch, U. Schollwöck, J. Eisert, and I. Bloch. Probing the relaxation towards equilibrium in an isolated strongly correlated one-dimensional Bose gas. *Nat. Phys.*, 8:325, 2012.

[170] J. H. Bardarson, F. Pollmann, and J. E. Moore. Unbounded growth of entanglement in models of many-body localization. *Phys. Rev. Lett.*, 109:017202, 2012.

[171] P. Zanardi and N. Paunković. Ground state overlap and quantum phase transitions. *Phys. Rev. E*, 74:031123, 2006.

[172] S. Flach, M. Ivanchenko, and R. Khomeriki. Correlated metallic two-particle bound states in quasiperiodic chains. *EPL*, 98:66002, 2012.

[173] F. Verstraete and J. I. Cirac. Quantum nonlocality in the presence of superselection rules and data hiding protocols. *Phys. Rev. Lett.*, 91:010404, 2003.

[174] H. Hennig and R. Fleischmann. Nature of self-localization of Bose-Einstein condensates in optical lattices. *Phys. Rev. A*, 87:033605, 2013.

[175] S. Diehl, A. Micheli, A. Kantian, B. Kraus, H. P. Büchler, and P. Zoller. Quantum states and phases in driven open quantum systems with cold atoms. *Nat. Phys.*, 4:878, 2008.

[176] C. Weitenberg, S. Kuhr, K. Mølmer, and J. F. Sherson. Quantum computation architecture using optical tweezers. *Phys. Rev. A*, 84:032322, 2011.

[177] Y. Lahini, G. R. Steinbrecher, A. D. Bookatz, and D. Englund. Quantum logic with interacting bosons in 1D. *arXiv:1501.04349*, 2015.

[178] A. M. Kaufman, B. J. Lester, and C. A. Regal. Cooling a single atom in an optical tweezer to its quantum ground state. *Phys. Rev. X*, 2:041014, 2012.

[179] J. D. Thompson, T. G. Tiecke, A. S. Zibrov, V. Vuletić, and M. D. Lukin. Coherence and raman sideband cooling of a single atom in an optical tweezer. *Phys. Rev. Lett.*, 110:133001, 2013.

Appendix A

Additional information for chapter 8

A.1 Detecting entanglement via collective measurements

The quantification of entanglement requires the measurement of non-linear functionals of a quantum state ρ, such as the n-th order Rényi entropy $S_n = \frac{1}{1-n} \ln \mathrm{Tr}(\rho^n)$ [159]. A general scheme to measure $\mathrm{Tr}(\rho^n)$ is to measure the shift operator V_n acting on n copies of the many-body system. The shift operator V_n re-orders the quantum states when acting on a collection of n states,

$$V_n |\Psi_1\rangle |\Psi_2\rangle \ldots |\Psi_n\rangle = |\Psi_n\rangle |\Psi_1\rangle \ldots |\Psi_{n-1}\rangle. \tag{A.1}$$

The experimentally relevant case of $n = 2$, for which the shift operator V_2 is simply the `swap` operator is discussed in detail in chapter 8. The central identity

$$\mathrm{Tr}(\rho_1 \rho_2) = \mathrm{Tr}(V_2(\rho_1 \otimes \rho_2)) \tag{A.2}$$

linking the expectation value of the shift operator to the quantum state overlap can be proven as [30]

$$\mathrm{Tr}\left(V_2(\rho_1 \otimes \rho_2)\right) = \mathrm{Tr}\left(V_2 \sum_{ijkl} \rho_{ij}^{(1)}\rho_{kl}^{(2)} |i\rangle \langle j| \otimes |k\rangle \langle l|\right)$$

$$= \mathrm{Tr}\left(\sum_{ijkl} \rho_{ij}^{(1)}\rho_{kl}^{(2)} |k\rangle \langle j| \otimes |i\rangle \langle l|\right)$$

$$= \sum_{ijkl} \rho_{ij}^{(1)}\rho_{kl}^{(2)} \delta_{kj}\delta_{il} = \sum_{ik} \rho_{ik}^{(1)}\rho_{ki}^{(2)} = \mathrm{Tr}\left(\rho_1\rho_2\right) \qquad (A.3)$$

In the case where the two state are identical ($\rho_1 = \rho_2 = \rho$), the expectation value of V_2 gives the purity $\mathrm{Tr}(\rho^2)$.

A.2 Beamsplitter operation and phase shifts

As detailed in chapter 8, the expectation value of V_2 can be measured using the discrete Fourier transform

$$(a_1^\dagger + a_2^\dagger)/\sqrt{2} \to a_1^\dagger$$

$$(a_1^\dagger - a_2^\dagger)/\sqrt{2} \to a_2^\dagger \qquad (A.4)$$

Using controlled tunneling in a double-well potential, we can implement the beamsplitter transformation for bosonic atoms:

$$a_1^\dagger \to (a_1^\dagger + ia_2^\dagger)/\sqrt{2}$$

$$a_2^\dagger \to (ia_1^\dagger + a_2^\dagger)/\sqrt{2} \qquad (A.5)$$

where a $\pi/2$-phase (i) is associated with each tunneling event across the double-well. Note that this transformation is *not* equivalent to the Fourier transform in equation (A.4). It is easy to verify that the Fourier transform is realized with the following protocol sequence of the beamsplitter operation and relative phase shift operations:

1. A $-\pi/2$ phase shift $(-i)$ on copy 2

2. The beamsplitter operation in equation (A.5)

3. Another $-\pi/2$ phase shift on copy 2

The inclusion of the additional phase shifts are important to correctly map the symmetric (antisymmetric) eigenstates of the `swap` operator onto states with even (odd) atom number parity in output port 2 of the beamsplitter. The resulting protocol is valid for measuring purity of any general many-body state. In the classical limit where the incident states are two identical coherent states with well-defined identical phases, the inclusion of the proper phase factors in input 2 ensures that the states interfere destructively in output 2. In this port, the total number of bosons is always zero and therefore even, so the measured parity $\langle V \rangle = 1$ correctly gives $\rho_1 = \rho_2$ and $\mathrm{Tr}\rho^2 = 1$. This situation is analogous to the interference of two phase-stabilized laser beams on a 50-50 beamsplitter, which may result in zero intensity in one output for the correct choice of incident phases. Away from the classical limit, for example as the input states become number squeezed states with decreasing uncertainty in atom number but increasing fluctuation in phase, atoms start to appear in output port 2 after the protocol in pairs only (even parity) as long as the input states remain pure and identical.

The protocol also works when there is no global phase relationship between the interfering many-body states, such as in our current experiments. The two copies are prepared each as an independent quantum state with a fixed number of atoms, so there is no well-defined phase. There are also no defined phases when the incident states to the beamsplitter are subsystems partitioned out of bigger systems that are themselves in Fock states. In either case, step 1 of the above protocol has no physical meaning in the absence of a defined

phase and might be omitted from the experiment without changing the resulting state after the transformation. The in situ fluorescence imaging of our microscope detects parity of the atom number on each lattice site which is phase insensitive, so step 3 is also redundant. The beamsplitter operation in the double-well alone is thus sufficient to implement the mapping of `swap` operator eigenstates onto states with even or odd atom number parity. The two output ports are then equivalent and the purity measurements may be obtained from the atom numbers on either side of the double-well after the many-body interference sequence.

A.3 Experimental sequence

Our experiments start with a single-layered two-dimensional $n = 1$ Mott insulator in a deep lattice ($V_x = V_y = 45E_r$). The full experimental sequence is illustrated in Fig.A.1.

State preparation We deterministically prepare a plaquette of 2×2 or 2×4 atoms from a Mott insulator by two subsequent cutting operations described in chapter 4. At the end of the state preparation sequence, the fidelity of unit occupancy is $94.6(2)\%$ per site, limited primarily by the fidelity of the initial Mott insulator and losses during the state preparation. We verify independently that defects are predominantly empty, not doubly occupied sites, most likely due to particle loss during state preparation.

Evolution in independent copies For studying the ground state entanglement using the 2×4 block, we turn on an optical potential with two narrow Gaussian peaks separated by four lattice sites along the x direction and flat-top along y. This confines the atoms inside
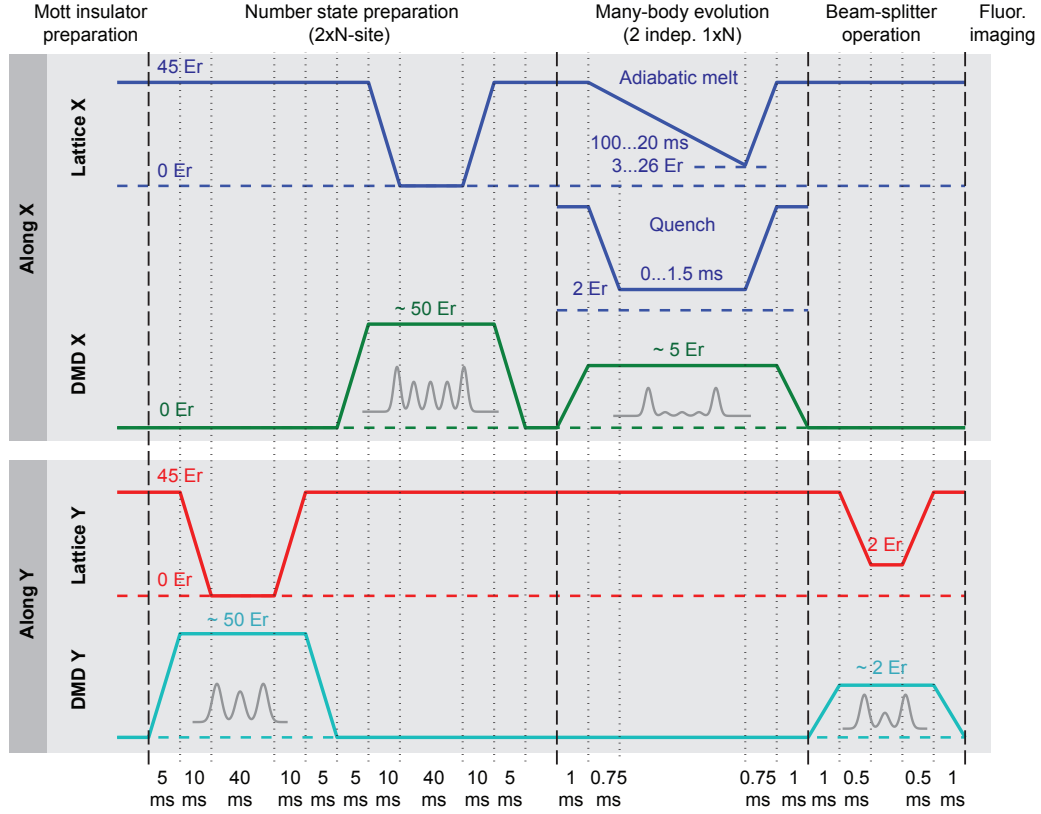
Figure A.1: Experimental sequence. Schematic showing the ramps of the x- and y- lattices and the projected potential from the DMD. The profiles of the DMD potentials are sketched in the direction of interest, while the other direction always has a smooth flattop profile aross the region of interest. Ramps are exponential in depth as a function of time.

the 4-site "box potential". The x lattice is then ramped down adiabatically to various final depths from 26 to $3E_r$. The ramp in depth is exponential in time with a duration of $100\,\text{ms}$ from 45 to $3E_r$. The y-lattice is kept at $45E_r$ so that tunneling along y is negligible and the two copies evolve independently.

For quench dynamics using the 2×2 block, we use a double-well potential along x with $V_{\text{dw}} = 2E_r$ to prevent atoms from leaving the 2-site system. The x lattice is ramped from $45E_r$ to $2E_r$ in $0.75\,\text{ms}$ and held for a variable time. The presence of the double-well
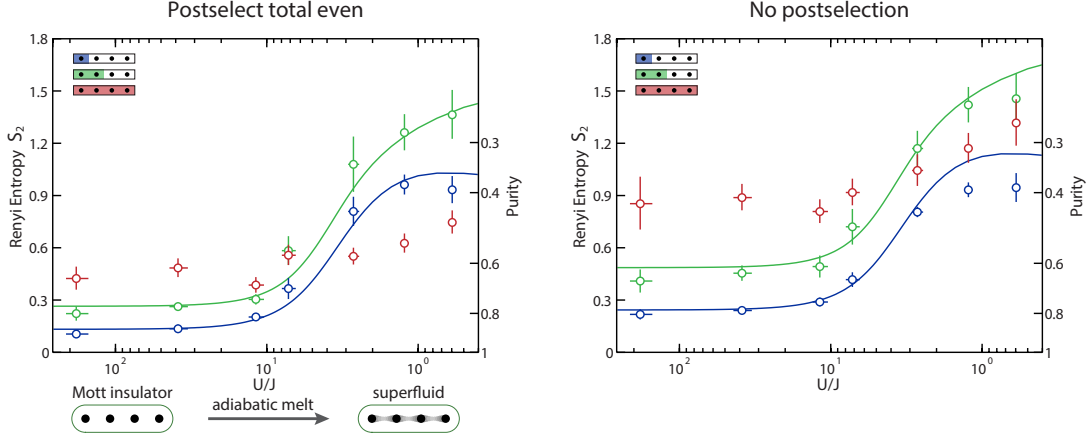
Figure A.2: Rényi entropy of the 4-site system and its subsystems with and without post-selection. The post-selection removes classical entropy and reduces the entropy of the full system (red) from ~ 0.9 to ~ 0.5. Note that even without postselection the entropy of the half-chain (green) rises above the full system entropy, indicating bipartite entanglement. Theory curves are exact diagonalizations shifted vertically by the mean classical entropy per site calculated from the full system entropy.

slightly modifies the values of U and J from values in a lattice only, yielding $U/J = 0.3$ during the hold time.

Many-body coherence In order to measure the correct state overlap $\mathrm{Tr}(\rho_1 \rho_2)$ after the interference step, it is crucial to maintain many-body coherence between the state preparation along x and the beamsplitter operation along y. During this time, the state is pinned in a deep $V_x = V_y = 45 E_r$ lattice, where tunneling is suppressed, but phase evolution occurs due to residual gradients and on-site interactions. Suppose that the prepared state in each copy is ρ_i, and that in the deep lattice each copy evolves under unitary u_i to a new state $\tilde{\rho}_i$.

Then

$$\mathrm{Tr}(\tilde{\rho}_1 \tilde{\rho}_2) = \mathrm{Tr}(u_1^\dagger \rho_1 u_1 u_2^\dagger \rho_2 u_2)$$

$$\neq \mathrm{Tr}(\rho_1 \rho_2) \tag{A.6}$$

i.e. the measured quantity is not the desired state overlap $\mathrm{Tr}(\rho_1 \rho_2)$. If, however, $u_1 = u_2 = u$, then

$$\mathrm{Tr}(\tilde{\rho}_1 \tilde{\rho}_2) = \mathrm{Tr}(u^\dagger \rho_1 u u^\dagger \rho_2 u)$$

$$= \mathrm{Tr}(u^\dagger \rho_1 \rho_2 u)$$

$$= \mathrm{Tr}(\rho_1 \rho_2) \tag{A.7}$$

since unitary evolution is trace-preserving. Phase dynamics in the deep lattice, for example "collapse and revival" evolution, does not affect the measurement, and the global state overlap $\mathrm{Tr}(\rho_1 \rho_2)$ is preserved *if the evolution is the same in both copies*. For the overlap of subsystem matrices $\mathrm{Tr}(\rho_{1A} \rho_{2A})$ to be preserved, we additionally require the evolution in subsystems A and B to be independent in each copy, i.e $u_i = u_{iA} \otimes u_{iB}$. This condition is fulfilled to a very high degree in the deep lattice, where tunneling is suppressed.

The experimentally most relevant source of error are differential gradients between the two copies in the deep lattice. Their impact can be suppressed by keeping the hold time in the deep lattice as short as possible.

A.4   Data analysis

Post-selection   Before data analysis we post-select outcomes of the experiment for which the total number of atoms detected within the plaquette (2×2 or 2×4 sites) is even. Outcomes outside this subset of data indicate either state preparation errors, atom loss during

the sequence, or detection errors. We furthermore reject all realizations for which we detect atoms in the 20×20 block surrounding the region of interest, most likely corresponding to atoms being lost from the plaquette during the sequence. Note that a combination of multiple errors (e.g. failure to load atoms on two sites) may lead to an unsuccessful run of the experiment being included in the post-selected data.

For experiments on the 2×2 plaquette we typically retain 80% of the data, and 60% for the 2×4 plaquette.

Calculating Purity and Entropy For the full many-body state and each subsystem of interest we calculate p_{odd}, the probability of measuring a total odd number of atoms after the beamsplitter operation within the post-selected data. The quantum mechanical purity and second-order Rényi entropy are then given by

$$\mathrm{Tr}(\rho^2) = 1 - 2p_{\mathrm{odd}}, \tag{A.8}$$

$$S_2(\rho) = -\ln(\mathrm{Tr}(\rho^2)). \tag{A.9}$$

We average the calculated purity $\mathrm{Tr}(\rho^2)$ over both copies and over equivalent partitions. For instance, the single-site entropy reported in Figure 8.5 is the mean over the first and last site of each copy of the 4-site system. From the variance of the parity in each subsystem and the covariance between subsystems we obtain the statistical standard error of the mean parity, taking into account possible correlations between regions. The reported error bars are the quadrature sum of the statistical error and the standard deviation of mean parities over the averaged regions. This procedure accounts for residual inhomogeneities between

the copies and along the chains.

Errorbars in U/J correspond to a typical uncertainty in the optical lattice depth of $\pm 2\%$.

Full system purity For the 2×4 plaquette, the initial state purity is reduced from 1 due to the presence of thermal holes in the initial Mott insulating state. Assuming all even sites are holes, the loading statistics for the 2×4 plaquette are:

N atoms	loading probability $p(N)$
8	0.66(1)
7	0.27(1)
6	0.052(4)

i.e. the postselected subset of total even data contains $\frac{0.052}{0.052+0.66} = 7\%$ of events with 6 atoms total. The inclusion of outcomes with 6 atoms reduces the purity of the initial state to 0.94, corresponding to a Rényi entropy of 0.06. This effect is small compared to the extensive entropy induced by beamsplitter imperfections.